Nanoscale

REVIEW

View Article Online
View Journal | View Issue

Cite this: *Nanoscale*, 2026, **18**, 1250

MXene quantum lands: emerging trends and breakthroughs

Mahdi Hasanzadeh Azar, *[a,b] Fatemeh Etehadi,[c,m] Nima Mohamadbeigi,[d] Hessam Shahbazi, [e,f] Sara Salehi Siouki,[g] Ali Mirsepah,[h] Mohammad Reza Rahmani Taji Boyuk,[i] Ahmad Alem,[g] Amir Hatamie,[j] Abdolreza Simchi*[k] and Shayan Angizi*[l]

Chemically stable two-dimensional MXene quantum dots (MQDs) have gained significant attention owing to their exceptional optical properties, tunable surface chemistry, and promising biocompatibility. Leveraging these properties, MQDs have found broad applicability across diverse domains, including optoelectronics (LEDs, lasers, detectors, and solar cells), energy storage (batteries and supercapacitors) and energy conversion (CO_2 reduction and hydrogen evolution), sensing, and biomedicine. This review provides a comprehensive overview of recent advancements in eco-friendly synthesis and surface modification strategies aimed at enhancing the radiative recombination efficiency of fluorescent MQDs. Furthermore, we critically assess the wide-ranging practical applications of MQDs and evaluate the progress achieved through both experimental and computational approaches. Special emphasis is placed on the most promising avenues for improving their optical performance and integration into high-efficiency devices. Finally, we outline key challenges and offer insights into future research directions. This review bridges fundamental understanding with technological development, reinforcing the transformative potential of MQDs in next-generation applications.

Received 26th August 2025,
Accepted 4th December 2025

DOI: 10.1039/d5nr03616j

rsc.li/nanoscale

1. Introduction

MXenes, a groundbreaking class of two-dimensional transition metal carbides (TMCs) and nitrides, have gained remarkable attention for their chemical stability, tuneable surface functionalities, and exceptional electrical conductivity.[1–3] These materials have been extensively studied and successfully integrated into diverse applications, including energy storage,[4–6] catalysis, optoelectronics,[7–9] and biomedical devices.[8,10] Despite the wealth of research on MXenes, their versatility continues to unveil new opportunities with new areas, such as nanoscale and quantum-sized materials.[1,2,11] Therefore, there is yet untapped potential for scientific exploration and technological advancement.

Among emerging frontiers, MXene Quantum Dots (MQDs) stand out as promising yet underexplored materials. By downsizing MXenes to quantum scales, MQDs retain the advantageous properties of their parent material, such as structural stability and chemical tunability, while gaining unique features like enhanced photoluminescence (PL), superior dispersibility, and improved biocompatibility.[1,8,9,12,13] These characteristics make MQDs well-suited for a wide range of applications, from biosensing and bioimaging to energy and optoelectronic and conversion/storage devices (Fig. 1), with the latter including thousands of studies on MQDs and other

[a]*Department of Mechanical and Mechatronics Engineering, University of Waterloo, Waterloo, Ontario N2L 3G1, Canada. E-mail: mhasanza@uwaterloo.ca*
[b]*Waterloo Institute for Nanotechnology, University of Waterloo, Waterloo, Ontario, Canada*
[c]*Leibniz Institute for Composite Materials GmbH (IVW), Erwin-Schrödinger Str. 58, 67663 Kaiserslautern, Germany*
[d]*Department of Materials Science and Engineering, Imam Khomeini International University (IKIU), Qazvin 3414916818, Iran*
[e]*Department of Mechanical and Industrial Engineering, University of Illinois Chicago, Chicago, IL, 60607, USA*
[f]*Department of Electrical and Computer Engineering, University of Illinois Chicago, Chicago, IL, 60607, USA*
[g]*Department of Polymer Engineering and Science, Technical University of Leoben, Otto-Glöckel-Strasse 2, A-8700 Leoben, Austria*
[h]*Department of Physics, Isfahan University of Technology, Isfahan 84156-83111, Iran*
[i]*School of Metallurgy and Materials Engineering, College of Engineering, University of Tehran, P.O. Box: 11155-4563, Tehran, Iran*
[j]*Department of Chemistry, Institute for Advanced Studies in Basic Science (IASBS), No. 444, Prof. Yousef Sobouti Boulevard, Zanjan 45137-66731, Iran*
[k]*Fraunhofer Institute for Manufacturing Technology and Advanced Materials, 28359 Bremen, Germany. E-mail: abdolreza.simchi@ifam.fraunhofer.de*
[l]*Department of Mechanical and Industrial Engineering, University of Toronto, 5 King's College Road, Toronto, Ontario M5S 3G8, Canada. E-mail: shayan.angizi@utoronto.ca*
[m]*Institute for Automation and Applied Informatics, Karlsruhe Institute of Technology, Hermann-von-Helmholtz-Platz 1, 76344 Eggenstein-Leopoldshafen, Germany*

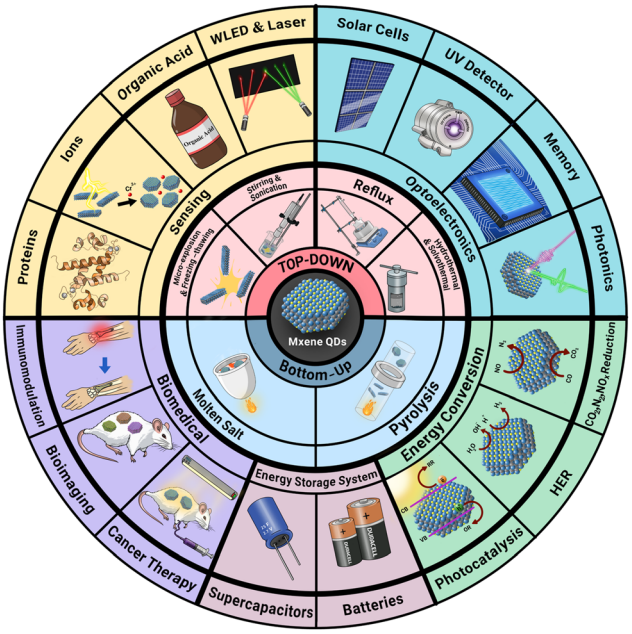

Fig. 1 A schematic diagram illustrating the innovative synthesis methods and applications of MQDs.

nanostructured materials in less than two decades (Fig. S1).[14–17] However, their synthesis, properties, and full application potential remain in the early stages of investigation, leaving ample room for breakthroughs in both fundamental science and practical implementations. Although some review papers have covered specific aspects of MQDs,[3,18–21] there is a noticeable lack of comprehensive review covering the recent advances in the synthesis, properties, and applications of MQDs.

This review presents a comprehensive and conceptually unified framework that systematically integrates the rapidly expanding body of knowledge on MQDs. It aims to elucidate how the electronic structure and surface chemistry of MQDs govern their functional performance across diverse applications, while identifying key challenges and outlining prospective research opportunities. The discussion is organized into three interrelated domains, synthesis methodologies, structure–property relationships, and emerging applications, to provide a coherent connection between fundamental understanding and technological relevance. This article first introduces the structural diversity and compositional tunability of MXene materials, highlighting their vast potential as a versatile family for next-generation technologies. It then explores various synthesis techniques, including both top-down and bottom-up approaches, to emphasize how synthesis parameters critically influence particle size, surface states, and the resulting physicochemical properties.[1] The subsequent sections delve into the optical, electronic, and biocompatible characteristics of MQDs, followed by an in-depth examination of their implementation in key application areas such as sensing,[2,5–7,11] optoelectronics,[8] energy conversion and storage,[22] and biomedicine.[10,13,23,24] Finally, through the introduction of a challenges–solutions–outlook framework, this review integrates the discussed aspects into a single analytical perspective, linking nanoscale design strategies to macroscopic device performance. This structured and comparative approach provides a comprehensive and forward-looking overview of the MQDs landscape, offering valuable insights into future research directions and underscoring the transformative potential of MQDs in advanced technologies.

2. Structural features

MAX phases, consisting of transition metal carbides or nitrides, serve as three-dimensional precursors to two-dimen-

Mahdi Hasanzadeh Azar

Mahdi Hasanzadeh Azar received his M.A.Sc. degree (B.Sc. degree) in Engineering Physics (Materials Science and Engineering) from McMaster University, Canada, with research experience in synthesizing, characterizing, and applying fluorescent quantum dots and wells into various optoelectronic devices. He is currently a Ph.D. student in the Functional Nanomaterials Group (FNG) at the University of Waterloo, holding Ontario Graduate Scholarship in Canada. His research focuses on developing scalable spatial atomic layer deposition method for the large-scale fabrication of perovskite thin film solar cells modified by transition metal dichalcogenides quantum dots.

Fatemeh Etehadi

Fatemeh Etehadi received her M.Sc. in Materials Engineering and Nanotechnology from Politecnico di Milano, Italy. She worked at the Leibniz Institute for Composite Materials on sustainable wood-based composites and is currently pursuing a Ph. D. at the Karlsruhe Institute of Technology, focusing on printed eco-friendly sensors. Her research interest is in developing sustainable and stable solutions by integrating different aspects of sensor technology.

sional MXenes. They are represented by the formula $M_{n+1}AX_n$ (n = 1 to 4), where 'M' refers to an early transition metal (mostly from groups 3–6 (Sc, Y, Ti, Zr, Hf, V, Nb, Ta, Cr, Mo, W)), 'A' denotes an element from groups 13–15 (such as Al, Ga, In, Si, Ge, Sn, P, As, *etc.*), and 'X' is either carbon or nitrogen.[25,26] The distinct bonding structure of MAX phases features relatively weaker and more chemically reactive metallic M–A bonds compared to mixed covalent/ionic M–X bonds. Therefore, the A-layer in the MAX phase is selectively removed by a controlled etching process to form MXenes with the formula of $M_{n+1}X_nT_x$ (n = 1 to 4). Here, T_x denotes the type and number of surface terminations (–F, –OH, –Cl, or –O).[27,28] Typically, n + 1 layers of transition metal enclose n layers of carbon or nitrogen. When n = 1, the resulting structure, M_2X, adopts a hexagonal close-packed structure with the ABABAB stacking sequence. For n = 2 and n = 3, the crystal structures of M_3X_2 and M_4X_3 are face-centered cubic (FCC) with the ABCABC stacking arrangement. It is distinct that the properties of MXene are profoundly influenced by its crystal structure and surface terminations.[27,28]

Over the last decade, computational simulations have been instrumental in understanding the MXenes crystal structures and identifying novel, stable compounds, offering critical insights to experimental advancements. These simulations suggest that MXenes can manifest in five distinct structures (Fig. 2a): (i) mono-transition metal: structures like Ti_2C, which consist of a single type of transition metal uniformly distributed within the M-layers (first row); (ii) solid solutions, like $(Ti, V)_3C_2$, where two different metals are randomly arranged within the M-layers (second row); (iii) ordered double-transition metals, including Mo_2TiC_2, with a well-organized arrangement of two distinct metals within the M-layers (third row); (iv) ordered divacancy, such as $Cr_{4/3}C$, featuring systematically arranged two vacancy sites within the M-layers (fourth row); (v) high-entropy, like $TiVNbMoC_3$, an analogous to the high-entropy oxide of similar chemistry with multiple transition metals randomly distributed within the M-layers (fifth row).[29,30] Density functional theory (DFT) calculations further reveal that certain ordered MXenes are energetically more stable than their solid-solution counterparts. These findings have led to predictions of over 25 different ordered MXenes, highlighting the structural diversity and stability potential within this material class (third row).[21]

Regarding functional groups, the reactive M-element surfaces are rapidly functionalized by terminating species introduced during the etching process. These surface terminations occur at various symmetry sites, including FCC, HCP, atop positions directly above surface M elements, bridging sites between two M elements (Fig. 2b and c). Experimentally, synthesized MXenes predominantly exhibit –O, –OH, and –F terminations due to their greater thermodynamic stability compared to pristine MXenes.[19] However, the hierarchy of functional group stability remains compound-specific and highly dependent on the synthesis method. Theoretical studies suggest that the stability of MXenes increases in the order of –OH < –F < –O for $Ti_4N_3T_x$, $Ti_3C_2T_x$, and $Nb_4C_3T_x$.[30] The lower stability of OH terminations is attributed to hydrogen atom replacement or its conversion to –O at elevated temperatures. In practice, however, the stability order is also influenced by the etching method. For instance, in HF-based methods, the stability follows the order of –F > –O > –OH, whereas thermal treatments or HCl–LiF methods result in the order of –O > –F > –OH.[27,29] However, most simulations overlook the influence of the etching solution, causing significant discrepancies in predictions regarding the functionalization order.[27,29]

When the lateral size of MXenes is reduced below 10 nm, quantum confinement effect may come into play, resulting in the formation of MQDs.[19] While MQDs retain the essential structural attributes of 2D MXenes, they benefit from abun-

Nima Mohamadbeigi

Nima Mohamadbeigi received his Ph.D. degree in Nanotechnology, focusig on design and fabrication of self-powered gas and optical sensors based on triboelectric and thermoelectric nanogenerators for real-time health monitoring. He has substantial experience in developing multifunctional nanomaterials and integrating them into flexible, energy-harvesting sensing architectures. His current research interests include the advancement of self-powered wearable sensor technologies through the coupling of energy conversion and sensing mechanisms, with the overarching goal of realizing next-generation, battery-free health monitoring platforms.

Hessam Shahbazi

Hessam Shahbazi is a researcher at University of Illinois Chicago working at the interface of quantum materials and energy storage, where he investigates how electronic structure and chemical potentials govern material behavior in energy storage and conversion systems. His works expands to in situ and ex situ characterization of solid–solid and solid–liquid interfaces with first-principles calculations to probe reaction energetics and quantum phenomena at atomic scale, strengthened by hands-on R&D experience in lithium battery manufacturing sector at Tesla and early-stage hardtech startups in the field of quantum.

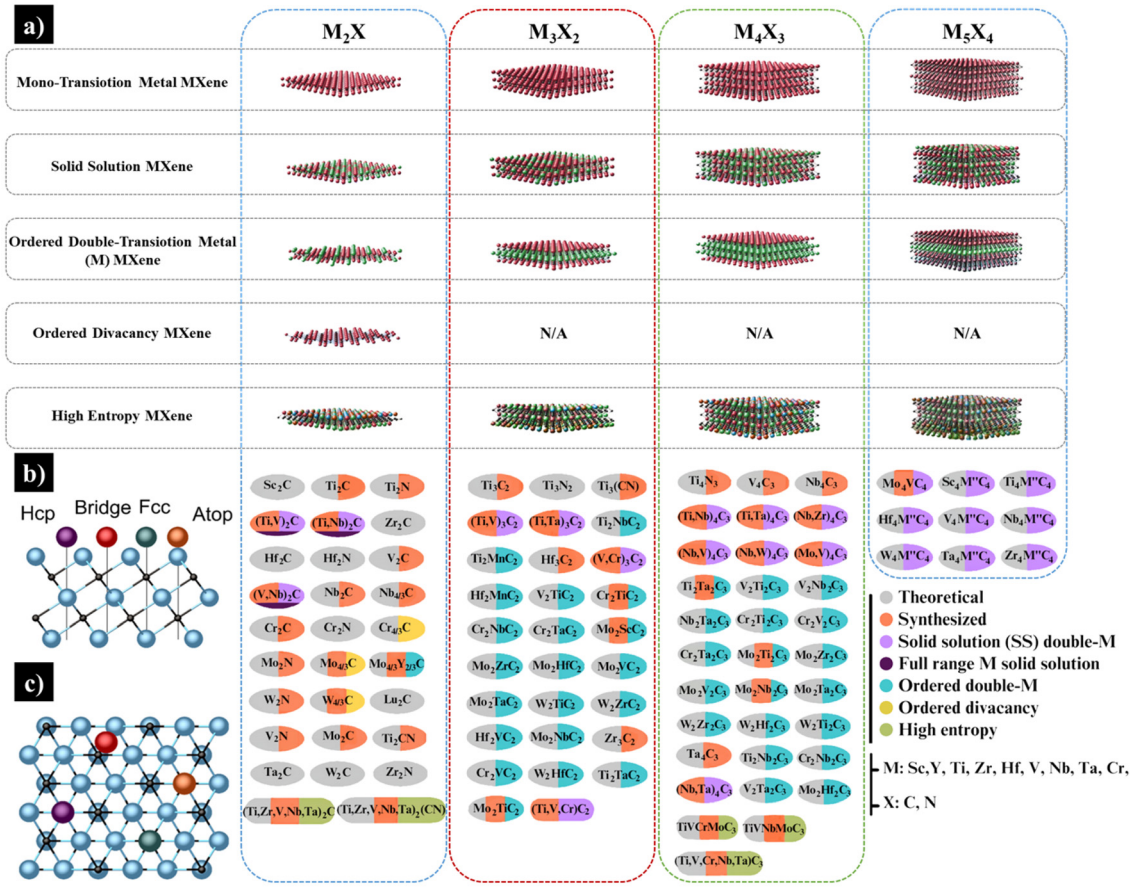

Fig. 2 (a) MXene structures and compositions: experimentally studied compositions are marked in orange and theoretical compositions in gray. Surface terminations are excluded. The schemes also include phases synthesized through bottom-up methods or phase transformations, such as W_2N, V_2N, and Mo_2N.[31,32] (b) Cross-sectional and (c) planar view of the available low-symmetry sites on an M_3X_2-type MXene surface. The four primary sites include HCP (purple), bridge (red), FCC (green), and atop (orange), with the vertical positioning of the terminating species being virtual and variable depending on the species (reprinted with permission from Elsevier, copyright © 2019).[27]

Sara Salehi Siouki

Sara Salehi Siouki received her M.Sc. degree in Materials Engineering and Nanotechnology from the Polytechnic University of Milan, Italy. She is currently pursuing a Ph.D. focused on nucleic acid immobilization strategies on photopolymer surfaces at the Technical University of Leoben, Austria. Her technical experience includes surface analysis and functionalization, antibacterial hydrogels, 3D bioprinting, DNA-based biosensors, and polymer synthesis.

Abdolreza Simchi

Dr Abdolreza (Arash) Simchi is an esteemed Professor of Materials Science and Engineering (MSE) at Fraunhofer Institute IFAM and an elected Fellow of the World Academy of Sciences (TWAS-UNESCO). Prof. Simchi's research focuses on advanced materials, particularly nanomaterials, additive manufacturing, and sustainable materials for biomedical and environmental applications. His contributions have been recognized with several prestigious awards, including the George Foster Research Award from the Alexander von Humboldt Foundation in 2020. He has also been ranked among the top 1% of world scientists based on citations by the ISI Web of Science since 2012.

dant, tunable functional groups, enhanced optical properties, and greater dispersibility. As a result, MQDs are exceptionally well-suited for sensing, energy storage, optoelectronics, and biomedical applications. The superior properties of MQDs provide a significant edge over their 2D counterparts, making them a versatile platform for cutting-edge research and technological advancements.[20]

3. Synthesis of MQDs

The synthesis of MQDs can be broadly categorized into two main strategies: top-down and bottom-up approaches. This section provides a general discussion of these methods. Table 1 presents details on the methods used for synthesizing various types of MQDs.

3.1. Top-down approaches

The top-down procedure is generally comprised of three main steps, including (i) preparation of MXene by etching layer "A" from the MAX phase, (ii) intercalation and exfoliation of layers to produce MXene nanosheets, and (iii) treatment to convert the nanosheets to QDs.

In the first step, the layer "A" is removed with either a chemical etching or electrochemical etching. Etchants like HF are commonly used to target MAX powders, for example, Nb_2AlC and Ti_3AlC_2, to produce MXene phases.[39,50,82] However, HF is a hazardous material, and even time-consuming multiple centrifugation processes have failed to remove HF completely.[24] Numerous attempts have been performed to use alternative chemical etchants. For instance, mixtures of HCl/KF, HCl/sodium fluoride (NaF), and LiF/HCl have proven effective for removing Al from Ti_2AlN,[23] Ta_4AlC_3 or Ti_3AlC_2,[35,38,41,43,60,64,71] and Ti_3AlC_2.[87] The acid (HCl) and fluorine components react with the MAX phases to remove Al by the formation of $AlCl_3$ and other products, such as metal hexafluoroaluminate, resulting in the formation of multilayered MXene. Alternatively, electrochemical etching can be conducted in a 3-electrode cell (Fig. 3a), consisting of a working electrode (*e.g.*, Ti_3AlC_2), an Ag quasi-reference electrode, and a Pt counter-electrode. An electrolyte (*e.g.*, [EMIM][PF_6]/MeCN) is used to remove the A-layer (Al) to prepare the MXene phase ($Ti_3C_2T_x$).[77]

For the preparation of MXene nanosheets, studies have determined that stirring multilayer MXenes in certain solvents like tetramethylammonium hydroxide (TMAOH) and sonication in tetrapropylammonium hydroxide (TPAOH),[50] dimethyl sulfoxide (DMSO),[33] and potassium hydroxide (KOH)[2] enable synthesizing MXene nanosheets.[34] While converting MXene multilayers to MXene nanosheets can be accompanied by various methods, a following procedure is required to synthesis MQDs.[88] A broad spectrum of approaches to synthesize MQDs are briefly presented below.

3.1.1. Stirring in intercalating solutions and sonication. Several studies have reported that facile procedures of stirring of a mixture of water and MXene nanosheets, followed by centrifugation, can effectively produce MQDs.[89] However, the sonication of MXene in certain solutions, such as *N*-methylpyrrolidone (NMP),[23,82] TPAOH,[45] TMAOH,[82] NaOH,[69] and ethanol,[46] has been the most widely adopted methods to convert MXene to MQDs. For example, Ti_2N QDs with lateral sizes of 2–6 nm and an average thickness of 1.8 nm have been prepared by sonicating the solution of Ti_2N nanosheets/NMP in an ice bath, followed by centrifugation.[69,89] Physical shearing forces caused by ultrasound as well as chemical reactions between MXene and NMP are outstanding driving forces inducing cleavage and fragmentation.[45]

3.1.2. Hydrothermal methods. Hydrothermal processing of MQDs is one of the most effective methods to process various types of QDs from nanosheets. This technique utilizes high pressure and temperature in a heated sealed autoclave containing an aqueous solution of MXene nanosheets to synthesize QDs in a reactive environment.[57,66] For instance, hydrothermal treatment of $Ta_4C_3T_x$ nanosheets, prepared through HCl/NaF etching and sonication processes, at 180 °C for 12 h in an ammonia solution results $Ta_4C_3T_x$ QDs.[66] A combination of hydrothermal and sonication methods can also be utilized to enhance the product yield of Ti_3C_2 QDs.[1]

Although various parameters influence the hydrothermal processing of MQDs, temperature manifests the most determining effect on their properties. For instance, Xu *et al.* synthesized MQDs with different sizes by varying the hydrothermal temperature of MXene nanosheets from 120 to 200 °C. After heating the solution of Ti_3C_2 nanosheets in nitric acid at 100 °C for 24 h and adjusting the pH to 7, 2 mL ethanediamine was added to 20 mL Ti_3C_2 nanosheets in a stainless-steel autoclave, followed by heating at 120, 160, and 200 °C for 12 h to synthesize nitrogen-doped Ti_3C_2 QDs. Taking the atomic force microscopy (AFM) and transmission electron microscopy (TEM) results into account, the lateral size/thickness of the N-Ti_3C_2 QDs changed from 3.93/0.7 nm at 120 °C to 3.7/1.4 nm at 160 °C and 5.76/3.8 nm at 200 °C, respectively (Fig. 3b–j). These results showed that the QDs treated at 120 °C, 160 °C, and 200 °C correspond to monolayer, bilayer, and multilayer structures, respectively, revealing the effect of temperature on the number of layers. Despite revealing the effect, no mechanism was proposed to explain this trend, which should be addressed in future investigations. The XPS characterization of N-MQDs shows that C=N bonds was dominant at 200 °C stating that overcoming the energy barrier requires higher temperature. The life-time investigation demonstrates that temperature increment up to 160 °C increases life-time to a maximum, however, at higher temperature life-time decreases possibly owing to chemical state change.[36]

Both doping and surface functionalization of MQDs can be performed during hydrothermal synthesis. In the former case, studies have shown that adding HNO_3, H_2SO_4, and ethylenediamine results in nitrogen (N)-doping of Ti_3C_2 QDs.[81] As a result of doping, the size of MQDs can be altered. For example, during N-doping of Nb_2C, the thickness decreased from 5.0 to 2.8 nm with a marginal effect on the lateral size.[90] Regarding

Table 1 Synthesis of MQDs by various methods

			Morphology		Size			
MQD	Method	Chemicals	NS	QD	l (nm)	t (nm)	Mechanism	Ref.
Ti_2N	Sonication	NSs: Ti_2AlN, HCl, KF QDs: NMP, ice bath, PBS, Ti_2N, ethanol, soybean phospholipid, chloroform	(1) 12 h etching of Ti_2AlN (2) 2 h sonication at 45 °C (3) Centrifugations at 3500 rpm (4) Decantation	(1) 24 h ice bath sonication (2) 20 h tip sonication (3) Centrifugation at 9000 rpm (4) Centrifugation at 12 000 rpm (5) Rinse by PBS or DI water (6) 10 min sonication (7) Rotary evaporator at 60 °C	4.83	1.81	—	19
Nb_2C	Sonication	NSs: Nb_2AlC, HF, ethanol QDs: TPAOH	(1) 2 days etching of Nb_2AlC (2) 15 min centrifugation (3) Wash with ethanol	(1) Stirring in TPAOH (2) 10 h pulsed ultrasonication in ice bath (3) Filtration (4) Freeze-drying	1–5	1.2	—	33
Ti_3C_2	Sonication	NSs: Ti_3AlC_2, HF QDs: $Ti_3C_2T_x$, TMAOH	(1) 20 h etching of Ti_3AlC_2 (2) Centrifugation (3) Wash (pH = 5–6)	(1) 24 h stirring (2) Centrifugation (3) 20 h sonication (4) 10 min centrifugation	3.4	1.65	—	31
Ti_3C_2OH	Sonication	NSs: Ti_3AlC_2, HF QDs: $Ti_3C_2T_x$, NaOH	(1) Ti_3AlC_2 + HF (2) Washing (3) Freeze-drying	(1) Sonication (2) Agitation (3) Centrifugation (4) Dialysis (5) Freeze-drying	2.4–3.2	1.48–1.99	—	34
$Ti_3C_2T_x$	Sonication	NSs: Ti_3AlC_2, LiF QDs:	(1) 48 h at 40 °C in oil bath (2) Washing	(1) Ultrasonication (2) Centrifugation (3) Vacuum freeze-drying	10	—	—	35
$Ti_3C_2T_x$	Centrifugation + stirring	NSs: Ti_3AlC_2, LiF, HCl, $Ti_3C_2(OH)_2$, $Ti_3C_2F_2$ QDs: —	(1) 24 h mixing (2) Washing (3) Filter membrane (4) Drying	(1) 1 h stirring (2) 1 h centrifugation	2–6	5	—	36
N-doped Ti_3C_2	Solvothermal + sonication	NSs: — QDs: Ti_3C_2, DMF, ammonium hydroxide	—	(1) 1 h sonication (2) Ammonium hydroxide → pH ~ 9	3.09	—	—	37

Table 1 *(Contd.)*

MQD	Method	Chemicals	Morphology		Size		Mechanism	Ref.
			NS	QD	l (nm)	t (nm)		
				(3) 6 h heating (4) Centrifugation				
$Ti_3C_2T_x$	Sonication	NSs: Ti_3AlC_2, Ag wire, Pt wire, [EMIM][PF_6], MeCN QDs: MeCN	(1) Electrochemical cell, V = 3–7 V, 5 h (2) Centrifugation	(1) 10 h ultrasonication (2) Centrifugation	5.34	4	Strong binding capability of F^- with Al → etching	38
Ti_3C_2 QDs-AuNPs	Sonication	NSs: Ti_3AlC_2, LiF QDs: —	(1) 24 h stirring (2) 3 times centrifugation	(1) 10 h sonication (2) Centrifugation (3) Filtration	6.5	—	—	39
Ti_3C_2	Sonication	NSs: Ti_3AlC_2, HF QDs: Ti_3C_2	(1) 24 h stirring at 45 °C (2) Centrifugation (3) Washing (pH = 6) (4) Drying	(1) 24 h stirring (2) Centrifugation (3) Washing (4) 10 h sonication (5) Centrifugation (6) Filtration	~1.75	1.2	—	40
Ti_3C_2/watermelon peel aerogels	Sonication	NSs: Ti_3AlC_2, LiF, HCl, H_2SO_4 QDs: —	(1) 48 h stirring at 30 °C (2) Washing by H_2SO_4 (3) 5–10 min stirring (4) Centrifugation (5) Washing (6) Stirring (7) Centrifugation	(1) 10 min purging by N_2 (2) 5 h ultrasonic (3) Centrifugation (4) Filtration	<10	—	Immersing freeze-drying-dried fresh watermelon peel into QD dispersion	41
Mo_2C@NG	Sonication	NSs: — QDs: $(NH_4)_6Mo_7O_{24}{\cdot}4H_2O$ (AHM), graphene oxide, poly (oxypropylene) Diamines	—	(1) 5 min stirring (2) 1 min heating at 90 °C (3) Freeze-drying (4) 1 h heating at 500 °C in quartz tube (5) 4 h heating at 700 °C under Ar.	1.8 (MQD)	11.5 μm (MQD@NG)	—	42
Ti_3C_2	Sonication + hydrothermal	NSs: Ti_3AlC_2, NaF, HCl, DMSO QDs:	(1) 12 h etching of 1 g Ti_3AlC_2 (2) Centrifugation in HCl (3) Washing (4) Drying (5) 24 h stirring of Ti_3C_2 (6) Centrifugation (7) Sonication	(1) 10 h sonication (2) 12 h heating (3) Filtration (4) Dialysis	Diameter: 3.96	—	—	32
Ti_3C_2	Hydrothermal	NSs: Ti_3AlC_2, HF, DMSO	(1) 64 h etching of 2 g Ti_3AlC_2	(1) 12 h heating	—	—	—	43

Table 1 *(Contd.)*

MQD	Method	Chemicals	Morphology		Size		Mechanism	Ref.
			NS	QD	*l* (nm)	*t* (nm)		
		QDs: PEI	(2) Washing (3) Under vacuum (4) 24 h stirring (5) Centrifugation (6) Sonication	(2) Filtration (3) Dialysis				
V_2C	Hydrothermal	NSs: V_2AlC, HF QDs: ammonium hydroxide	(1) V_2AlC 24 h stirring (2) 48 h stirring (3) Freeze-drying (4) Sonication	(1) 6 h at 120 °C (2) Filtration (3) Dialysis	4.13	2–3	—	44
Ti_3C_2	Hydrothermal	NSs: HF, Ti_3AlC_2, TMAOH QDs: Ti_3C_2, ammonia	(1) HF etching of Ti_3AlC_2 (2) TMAOH intercalating	(1) 6 h heating at 100 °C at autoclave (2) Cooling (3) Filtration (4) Freeze-drying	4.2	1.2–2.0	—	45
Ti_3C_2	Hydrothermal	NSs: — QDs: Ti_3C_2 NSs, ethylenediamine	Chemical exfoliation	(1) 5 h sonication (2) 12 h heating at 160 °C (3) 220 nm mesh filter (4) 12 h dialysis	4	—	—	1
BSA@Ti_3C_2	Hydrothermal	NSs: Ti_3AlC_2, HF QDs: Ti_3C_2, BSA	(1) 20 h etching of 0.5 g Ti_3AlC_2 (2) 15 min centrifugation (3) Drying under vacuum	(1) 50 mg Ti_3C_2 NS 6 h heating at 120 °C (2) 15 min sonication (3) pH = 9 by ammonia (4) Centrifugation (5) Filter	2	—	—	30
$Ta_4C_3T_x$	Hydrothermal	NSs: Ta_4AlC_3, HCl, NaF QDs: $Ta_4C_3T_x$	(1) 48 h etching (2) Centrifugation (3) Washing (4) Freeze-drying (5) Drying at 60 °C (6) Sonication (7) Homogenizer	(1) 12 h heating of $Ta_4C_3T_x$ NSs	Diameter: 3.5	—	(1) HCl/NaF etchant: fewer surface defects compared to HF (2) $Toxicity_{NaF} < toxicity_{LiF}$ (3) Mechanical vibration and/or sonication: intercalation and interlayer spacing increment	20
Nitrogen-doped-Ti_3C_2	Hydrothermal	NSs: Ti_3AlC_2, HF QDs: Ti_3C_2, HNO_3, H_2SO_4, NaOH, ethylenediamine	(1) 48 h etching of 1.5 g Ti_3AlC_2 (2) Centrifugation (3) pH tuning (~7)	(1) 36 h mixing (2) Cooling to 25 °C (3) pH tuning (~7)	3.8	1.24	—	46

Table 1 *(Contd.)*

MQD	Method	Chemicals	Morphology		Size		Mechanism	Ref.
			NS	QD	l (nm)	t (nm)		
			(4) Vacuum-drying	(4) 25 min ultrasonication (5) 12 h heating at 180 °C (6) Filtration (7) Dialysis				
S and N doped-$Ti_3C_2T_x$	Hydrothermal	NSs: Ti_2AlC, TiC, HF QDs: HNO_3, H_2SO_4, Ti_3C_2, NaOH, $Na_2S_2O_3$, $NH_3{\cdot}H_2O$	(1) 16 h ball milling (2) 2 h at 1350 °C (3) Crushing (4) Washing (5) Centrifugation (6) Drying	(1) 2 h heating at 100 °C (2) NaOH → pH = 7 (3) 12 h heating (4) Dialysis	N-MQDs: 50 S-MQDs: 15–35	14.15 20.41	—	9
$Ti_3C_2T_x$	Hydrothermal	NSs: Ti_3AlC_2, HF QDs: ammonia	(1) 72 h stirring (2) Washing (3) Drying (4) Sonication	(1) 6 h heating (2) Centrifugation	<10 nm	1.98	—	47
Ti_3C_2 QDs decorated TiO_2/Nb_2O_5 composite	Hydrothermal	NSs: Ti_3AlC_2, HF QDs: ammonia	(1) 18 h etch (2) Rinsing (3) Centrifugation (4) Drying (5) Ultrasonication	(1) Ammonia → pH = 9 (2) 6 h heating (3) Filtration (4) Drying	3.8	—	—	48
$Na_2Ti_3O_7/Ti_3C_2T_x$ QDs	Hydrothermal	NSs: Ti_3AlC_2, HF QDs: $Ti_3C_2T_x$, dimethyl sulfoxide, $NH_3{\cdot}H_2O$	(1) 24 h stirring (2) Washing (3) Drying	(1) 4 h vibration (2) Washing (3) 6 h heating	—	—	—	49
Ni–Co LDH@Ti_3C_2 QDs	Hydrothermal	NSs: Ti_3AlC_2, LiF, HCl QDs: —	(1) 5 min stirring (2) 24 h stirring (3) Washing (4) 1 h sonication	(1) +Ammonia → pH = 9 (2) 6 h heating at 100 °C (3) Centrifugation	3.06 ± 0.78	—	—	50
N-doped Ti_3C_2	Hydrothermal	NSs: Ti_3AlC_2, HF QDs: Ti_3C_2, H_2SO_4, HNO_3, NaOH, methanol	(1) 24 h stirring (2) Centrifugation (3) Washing (4) Drying	(1) 6 h heating at 100 °C (2) Decant to ice water (3) +NaOH (pH = 7) (4) Centrifugation (5) 6 h drying (6) 5 h heating at 160 °C (7) Centrifugation (8) Evaporating	7.5	—	—	51
AgPt@N-Ti_3C_2 QDs	Hydrothermal	NSs: Ti_3C_2, nitric acid QDs: ethanediamine	(1) 24 h in oil bath at 100 °C (2) +Ice water + NaOH → pH = 7	(1) 12 h heating at 160 °C (2) Filtration	2–5	—	—	52

Table 1 *(Contd.)*

MQD	Method	Chemicals	Morphology		Size		Mechanism	Ref.
			NS	QD	l (nm)	t (nm)		
			(3) Centrifugation					
N-Ta_4C_3	Hydrothermal	—	(1) Etch	(2) Hydrothermal	1.9–3.3 (avg: 2.6)	0.8–3.2 (avg: 1.9)	—	53
Eu doped-Ti_3C_2	Hydrothermal	NSs: Ti_3AlC_2, HF, $NH_3{\cdot}H_2O$	(1) 20 h stirring	(1) 6 h heating at 120 °C	2.81	4.83	—	54
		QDs: —	(2) Washing	(2) 2 h heating at 90 °C				
			(3) Centrifugation (4) 48 h drying (5) 30 min sonication	(3) Centrifugation				
TiCN (titanium carbonitride, MXene-like)	Hydrothermal	NSs: —	—	(1) 5 min stirring	2.7 ± 0.2	2.7–4 (avg: 3.2 ± 0.3)	—	55
		QDs: TiCN		(2) 10 h heating at 120 °C (3) Centrifugation				
N, P-Ti_3C_2	Hydrothermal	NSs: Ti_3C_2, HCl, nitric acid	(1) 12 h at 100 °C	(1) 12 h at 120 °C	N,P-MQDs: 1–8 (2.73 ± 0.50)	0.85 ± 0.02	—	56
		QDs: diammonium phosphate (DAP)	(2) 100 mL ice + NaOH → pH = 7	(2) Filtration	N-MQDs: 3.14	0.93		
				(3) 2 days dialysis (4) Freeze-drying	P-MQDs: 2.97	0.71		
S, N-Nb_2C	Hydrothermal	NSs: Nb_2C, sulphuric acid, nitric acid	(1) 12 h at 100 °C	(1) 12 h heating at 160 °C	S, N-Nb_2C: 2.6–4.7 (avg: 3.56)	S, N-Nb_2C: 1.74	—	57
		QDs: L-cysteine	(2) +NaOH → pH = 7	(2) Filtration (3) 2 days dialysis	Nb_2C: 2.4 N-Nb_2C: 2.66	Nb_2C: 5.01 N-Nb_2C: 2.80		
N-doped Ti_3C_2 QDs@DAP	Hydrothermal	NSs: Ti_3C_2, $NH_3{\cdot}H_2O$	(1) 30 min ultrasonic	(1) 6 h heating at 120 °C	3.4	0.5–1.3	—	58
		QDs: —	(2) +$NH_3{\cdot}H_2O$ (under N_2) → pH = 9	(2) Centrifugation (3) Filtration				
Amino-functionalized Ti_3C_2	Hydrothermal	NSs: Ti_3AlC_2, HF, $NH_3{\cdot}H_2O$	(1) 24 h stirring at 60 °C	(1) 6 h heating at 120 °C	2.73	2.76	—	59
		QDs: —	(2) Rinse by DI (3) Centrifugation (4) 20 h drying (5) 30 min sonication	(2) 1 h dialysis (3) Centrifugation (4) Filtration (5) Freeze-drying				
N-doped Ti_3C_2	Hydrothermal	NSs: Ti_3AlC_2, LiF, HCl, APTES, ethanol	(1) 10 min stirring	(1) 12 h heating at 120 °C	7–10 (avg: 8.63)	—	—	60
		QDs: —	(2) 24 h stirring at 35 °C	(2) Filter				
			(3) Centrifugal washing	(3) Dialysis				
			(4) Vacuum-drying (5) 1 h ultrasonication (6) Centrifugation	(4) Freeze-drying				

Table 1 *(Contd.)*

MQD	Method	Chemicals	Morphology		Size		Mechanism	Ref.
			NS	QD	l (nm)	t (nm)		
			(7) Ultrasonication (8) 24 h stirring (9) Centrifugation					
TiO_2/Ti_3C_2	Hydrothermal	NSs: Ti_3AlC_2, LiF, HCl QDs: —	(1) Etch (2) Sonication	(1) Heating	Diameter: ~8.2	1.02	—	61
GSH-Ti_3C_2 QDs	Hydrothermal	NSs: Ti_3AlC_2, HF QDs: Ti_3C_2 NP, GSH, NaOH	(1) 24 h stirring at 40 °C (2) Washing (3) Centrifugation (4) 12 h drying (5) 5 h sonication	(1) 12 h heating at 120 °C (2) Filtration (3) 12 h vacuum drying	2.5	—	Sonication: Ti_3C_2 film cutting + hydrothermal	62
N, B-Ti_3C_2	Hydrothermal	NSs: — QDs: Ti_3C_2, boric acid, ammonia hydroxide	—	(1) 12 h heating at 100 °C (2) Filtration (3) Freeze-drying	2.25	—	—	63
N-Ti_3C_2	Hydrothermal	NSs: — QDs: Ti_3C_2, nitric acid, ethanediamine	—	(1) 24 h at 100 °C in oil bath (2) In beaker containing 100 mL ice, +NaOH → pH = 7. (3) 12 h heating at 160 °C (4) Filtration (5) 2 days dialysis	Hydrothermal: 120 °C: 3.93 160 °C: 3.7 200 °C: 5.76	Hydrothermal: 120 °C: 0.7 160 °C: 1.4 200 °C: 3.8	—	64
Nb_2C	Solvothermal	NSs: — QDs: Nb_2C, ammonia	—	(1) 0.5 h stirring of 15 mg Nb_2C (2) pH = 6 by ammonia (3) 6 h heating (4) Filtration (5) Drying	—	—	—	65
Nb_2C-SH[a]	Sonication	NSs: — QDs: Nb_2C, *n*-octadecyl mercaptan	—	(1) 30 min sonication (2) Stirring overnight (3) Filtration	2.3–5.4	—	—	
Carbide-derived graphene QDs	Solvothermal	NSs: $Ti_3C_2T_x$, HF QDs: DMF	(1) 5 h etching (2) Wash (3) Centrifugation (4) 3 h sonication	(1) Centrifugation (2) 20 h heating (3) Centrifugation (4) Dialysis	4–10	1.36	(1) Solvothermal → C–Ti bonds break (2) C atoms self-assemble into GQDs	66
Nb_2C	Solvothermal	NSs: HF, Nb_2AlC, TPAOH	(1) HF etching of Nb_2AlC for 5 days	(1) 30 min sonication	5 nm	—	—	29

Table 1 *(Contd.)*

MQD	Method	Chemicals	Morphology		Size		Mechanism	Ref.
			NS	QD	l (nm)	t (nm)		
		QDs: 20 mg Nb_2C NS, 20 mL TPAOH	(2) Stirring TPAOH + Nb_2AlC for 5 days (3) Sonication	(2) 24 h solvothermal at 110 °C (3) 120 h dialysis in water (4) Freeze-drying				
Ti_3C_2	Solvothermal	NSs: Ti_3AlC_2, HF QDs: DMSO, ammonia	(1) 24 h etching of Ti_3AlC_2 (2) Drying (3) Sonication	(1) Centrifuging (2) Washing (3) pH tuning (~9) by ammonia (4) Sonication (5) 6 h heating (6) Filtration	3	—	—	67
$Ti_3C_2T_x$	Solvothermal	NSs: Ti_3AlC_2, HF QDs: $Ti_3C_2T_x$, TMAOH	(1) 12 h etching of Ti_3AlC_2 (2) Thermal annealing	(1) 24 h shaking of as-prepared $Ti_3C_2T_x$ (2) Centrifugation (3) Sonication (4) Centrifugation (5) Filtration (6) Dialysis	4.99	—	—	68
$Ti_3C_2T_x$	Solvothermal	NSs: HF QDs: DMF, ethanol, DMSO	(1) Etch	(1) Disperse (2) 6 h heating (3) Centrifugation	s-MQDs: 1.8 e-MQDs: 2.5 f-MQDs: 3.3	1–2.5	(1) Higher polarity solvent → stronger interaction → easier exfoliation of NSs to QDs (2) Lower boiling point solvent → higher pressure → stronger exfoliation efficiency	69
N-doped Ti_3C_2	Solvothermal	NSs: Ti_3C_2, KOH QDs: Ti_3C_2, DMF	(1) 3 h sonication (2) Centrifugation	(1) 12 h heating at 140 °C (2) Centrifugation	2.3	—	—	2
N-Ti_3C_2	Solvothermal	NSs: DMF QDs: DETA, DMF	(1) Sonication (12 h at 750 W) (2) Centrifugation (3) Drying	(1) 8 h heating at 150 °C (2) 5 centrifugation re-suspension cycles (3) Drying	6.2	1	—	70
Ti_3C_2	Solvothermal	NSs: Ti_3AlC_2, HCl, LiF QDs: PEI	(1) 5 min stirring (2) 24 h stirring at 40 °C (3) Wash by DI (4) Centrifugation (5) Decanting → pH = 6 (6) 10 min purging with N_2	(1) 24 h heating at 120 °C under N_2 (2) Filtration (3) Dialysis	10.2	~1.0		71

Table 1 *(Contd.)*

MQD	Method	Chemicals	Morphology		Size		Mechanism	Ref.
			NS	QD	l (nm)	t (nm)		
			(7) 5 h ultrasonication (8) Centrifugation					
PLL-protected Ti_3C_2	Solvothermal	NSs: Ti_3AlC_2, HF QDs: Ti_3C_2 NP, ε-poly-L-lysine (PLL), NaOH	(1) 24 h stirring at 40 °C (2) Wash (3) Centrifugation (4) Purging with N_2 → film (5) 5 h sonication (6) Centrifugation	(1) 24 h heating at 100 °C under N_2 (2) Filtration (3) Dialysis (4) Drying (5) 12 h vacuum drying at 60 °C	3	—	—	72
Ti_3C_2	Reflux	NSs: Ti_3AlC_2, HF, TMAOH QDs: TMAOH	(1) 5 h etching Ti_3AlC_2 (2) Wash (3) Centrifugation (4) Vacuum-dry (5) Intercalation by TMAOH (6) Centrifugation (7) Vacuum filtration (8) Vacuum drying	(1) 1 day reflux (2) Centrifugation (3) Vacuum drying.	8	—	—	73
N-$Ti_3C_2T_x$	Reflux	NSs: Ti_3AlC_2 QDs: $Ti_3C_2T_x$, TMAOH	(1) 24 h stirring at 60 °C (2) Centrifugation (3) Wash → pH = 7 (4) Overnight desiccation under vacuum at 80 °C	(1) 3 days oil bath refluxing at 120 °C (2) Centrifugation (3) Overnight vacuum drying at 200 °C	2.7	—	—	74
$Ti_3C_2T_x$ QDs/TiO_2/FTO	Reflux	NSs: Ti_3AlC_2, HF, TMAOH QDs: TMAOH	(1) 12 h stirring (2) Centrifugation (3) Drying at 200 °C under vacuum (4) 12 h stirring (5) Centrifugation (6) Vacuum drying	(1) 1 day reflux at 110 °C (2) Centrifugation (3) Vacuum drying at 200 °C.	—	Avg: ~1.0	—	75
$Ti_3C_2T_x$	Microwave + reflux	NSs: Ti_3AlC_2, HF QDs: $Ti_3C_2T_x$	(1) 24 h stirring (2) Washing (3) 12 h drying	(1) 30 min microwave irradiation (2) Filtration (3) Reflux	3.3	2.5	—	76
UA@Ti_3C_2 QDs	Microwave	NSs: Ti_3C_2, HNO_3, NaOH, HCl QDs: UA	(1) 24 h heating at 100 °C (2) In beaker → pH = 7	(1) Microwave irradiation (2) Centrifugation	6.4 ± 0.5	—	—	77

Table 1 *(Contd.)*

MQD	Method	Chemicals	Morphology		Size		Mechanism	Ref.
			NS	QD	l (nm)	t (nm)		
			(3) Centrifugation					
N, P-Ti_3C_2 QDs	Microwave	NSs: HF QDs: Ti_3C_2, formamide, ammonia	(1) Etch	(1) Microwave (2) Centrifugation (3) Filtration (4) Vacuum drying	3.11 ± 0.86	—	—	78
Ti_3C_2	Microwave	NSs: Ti_3AlC_2, ammonia QDs: —	(1) 24 h stirring at 40 °C (2) Washing (3) Centrifugation (4) Drying at 60 °C under vacuum (5) 3 min ultrasonication	(1) Microwave (800 W, 5 min, 90 °C) (2) Filtration (3) 12 h vacuum drying at 60 °C	Diameter: 2 ± 0.33	—	—	63
Cl, N doped-Ti_3C_2	Potential static	NSs: — QDs: Ti_3AlC_2, Pt wire, TMAOH, NH_4Cl	—	(1) V = 0.1 V, 1 h (2) Centrifugation (3) Filtration (4) Dialysis	3.45	—	(1) Cl^- promotes N doping in graphene (2) Cl^- breaks Ti–Al bonds (3) NH_4OH is intercalated	79
$Ti_3C_2T_z$	Acoustomicrofluidic	NSs: Ti_3AlC_2, HF QDs: —	(1) 24 h stirring (2) Washing	(1) Cycles of centrifugation (2) Membrane vacuum-filtering (3) 24 h drying	7.8 ± 5.2	1.1 ± 0.2	Nebulization of sample driven by high frequency acoustic waves	80
$Ti_3C_2T_x$	Micro-explosion	NSs: Ti_3AlC_2, HF QDs: $Ti_3C_2T_x$	(1) 3days stirring at 40 °C (2) Centrifugation (3) Washing (4) 24 h drying	(1) +L-N_2 → evaporation (2) 24 h stirring (3) Filtration (4) Centrifugation (5) Freeze-drying	7.23	5	Temperature difference of L-N_2 and hot deionized water	81
WO_3/Ti_3C_2 QDs/In_2S_3	Freezing-and-thawing + sonication	NSs: Ti_3AlC_2, LiF QDs: —	(1) 24 h stirring (2) Centrifugation	(1) 5 min centrifugation (2) 3 h at 4 °C (3) 3 h at −38 °C (4) 4 times freezing-and-thawing (5) 2 h sonication (6) Filtration	1.66 ± 0.04	0.5–2	—	82
Mo_2C QDs embedded in carbon NSs	Molten salt	NSs: — QDs: molybdenum acetylacetonate, sucrose, ethanol, NaCl	—	(1) 15 min stirring at 70 °C (2) +NaCl (3) 2 h calcination at 800 °C under Ar	2–3	3.5 (Mo_2C/C NS)	—	83

Table 1 *(Contd.)*

MQD	Method	Chemicals	Morphology		Size		Mechanism	Ref.
			NS	QD	l (nm)	t (nm)		
Mo_2C nanoparticle-decorated carbon polyhedrons	Solvothermal + pyrolysis	NSs: — QDs: $Zn(CH_3COO)_2{\cdot}2H_2O$, MIM, PVP, DMF, Mo/ZIF-8, H_2SO_4	—	(4) 3 times washing (5) Centrifugation (1) 48 h heating at 160 °C (2) Centrifugation (3) Washing (4) Drying at RT (5) 2 h pyrolysis (6) Treating in 0.5 M H_2SO_4 aqueous	<5	—	—	84
Mo_2C QDs-decorated CNT networks	Spray-drying	NSs: — QDs: ammonium molybdate tetrahydrate, CNT	—	(1) 1 h ultrasonication (2) Spray drying (3) 1 h carbonization at 500 °C (4) 4 h at 700 °C under Ar	<3	—	Mo_2C QDs: polar and conductive → provide active sites to absorb + Mo_2C QDs welding spots for CNT	85
Mo_2C/C nanoflowers (ultrathin carbon NSs decorated with Mo_2C QDs)	*In situ* synthesis + calcination	NSs: — QDs: dopamine hydrochloride, ammonium molybdate, PEG, ethanol, $NH_3{\cdot}H_2O$	—	(1) 30 min stirring (2) Injecting of $NH_3{\cdot}H_2O$ (3) 6 h stirring (4) Centrifugation (5) Washing (6) 2 h stabilizing at 450 °C (7) 3 h calcining at 900 °C under Ar	2–4	—	—	86

Average lateral size (l), thickness (t), 2,3-diaminophenazine (DAP), 2-methylimidazole (MIM), 2,2′-diethanolamine (DETA), 3-aminopropyltriethoxysilane (APTES), bovine serum albumin (BSA), carbon nanotube (CNT), dimethyl sulfoxide (DMSO), dimethylformamide (DMF), glutathione (GSH), methanol quantum dots (MQDs), nanosheet (NS), polyethyleneimine (PEI), poly (vinylpyrrolidone) (PVP), quantum dot (QD), tetramethylammonium hydroxide (TMAOH), tetrapropylammonium hydroxide (TPAOH), uric acid (UA), zeolitic imidazolate frameworks (ZIF).
[a] MXene QDs functionalized with the thiol group.

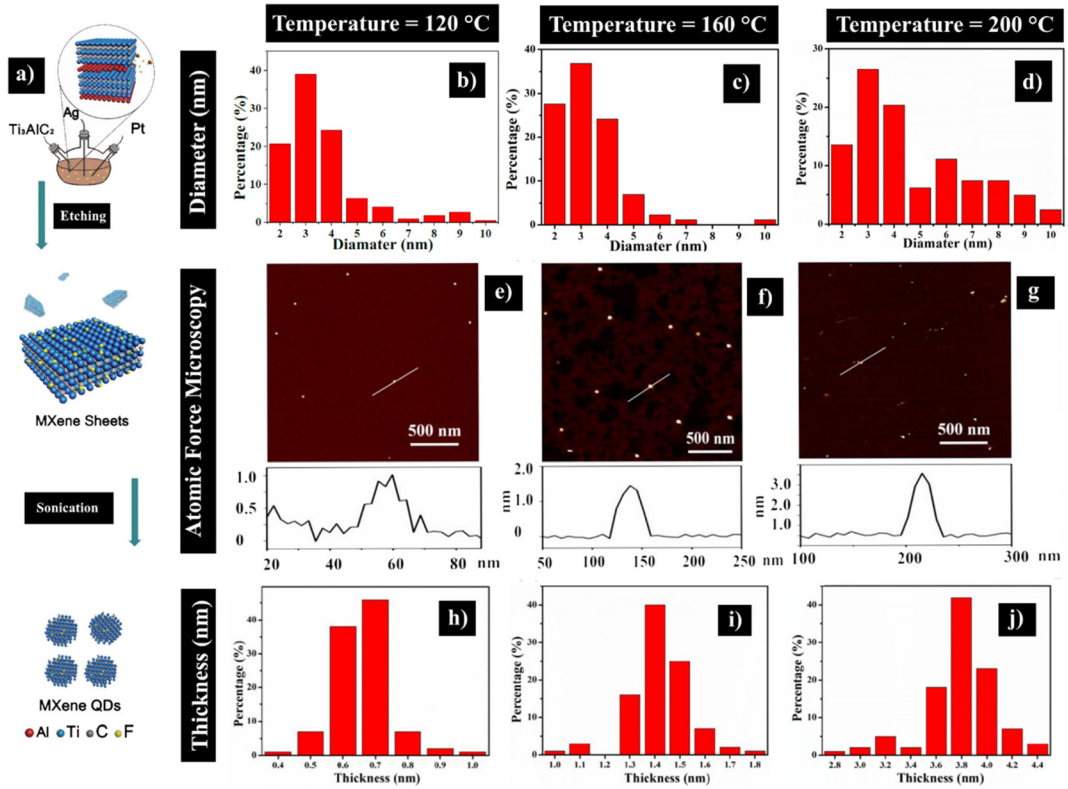

Fig. 3 (a) Electrochemical etching of Ti_3AlC_2 to produce $Ti_3C_2T_x$ MQDs (reprinted with permission from American Chemical Society, copyright © 2020).[77] (b–d) Size distribution, (e–g) AFM images, and (h–j) thickness of QDs depending on the processing temperature: (b, e and h) 120 °C; (c, f and i); 160 °C; (d, g and j) 200 °C (reprinted with permission from Royal Society of Chemistry, copyright © 2022).[36]

the latter case, Al-Duais *et al.*[39] have indicated that sonication-assisted hydrothermal treatment of aqueous solution of Ti_3C_2 and bovine serum albumin (BSA) forms BSA-functionalized Ti_3C_2 QDs (BSA@Ti_3C_2), serving as sensitive fluorescent probes.[39]

An alternative benefit of hydrothermal treatments is the fabrication of MQD/semiconductor heterostructures. Ding *et al.*[81] have prepared N-Ti_3C_2 QDs/CdS nanorods heterostructure through a self-assembly strategy by mixing the CdS nanorods (length = 1–2 μm and D = 30 nm) with N-Ti_3C_2 (D = 3.8 nm and t = 1.24 nm) in DI water for two days. Using a similar strategy, g-C_3N_4@Ti_3C_2 QD composites were prepared by mixing the g-C_3N_4 NSs and Ti_3C_2 QDs for 24 h. Ti_3C_2 QDs assisted g-C_3N_4 in: (i) boosting the density of the active sites, (ii) increasing the specific surface area, and (iii) improving carrier transfer efficiency due to excellent electronic conductivity in view of metallic characteristic.[33]

3.1.3. Solvothermal methods. Solvothermal treatments of MXene nanosheets, similar to the hydrothermal method but differing in the type of solvent used, have garnered considerable attention. In this process, organic solvents, such as TPAOH,[50] DMF,[2,91] DMSO,[79] and ethanol,[67] are used instead of an aqueous solution to synthesize MQDs. For instance, the solvothermal processing of Nb_2C NSs in TPAOH at 110 °C for a day yields spherical Nb_2C QDs with a diameter of 5 nm.[50]

The type of the solvent plays an important role in altering the properties of MQDs. Fig. 4a–f clearly shows that solvothermal treatment of MXene nanosheets in DMF, DMSO, and ethanol provides MQDs with a different lateral size. The higher polarity of the solvent increases the interaction between solvent and nanosheets, leading to exfoliation facilitation and further size reduction. Therefore, DMSO with the highest polarity and strongest oxidation ability formed the smallest particles. In contrast, DMF with higher polarity than ethanol shows larger particles, corresponding to the effect of boiling point. The lower the boiling point, the higher the vessel pressure, paving the way for preparing smaller particles. In this case, the boiling point of ethanol (74.8 °C) is lower than DMF and the solvothermal temperature (120 °C), thereby producing more evaporated gas molecules and higher pressure, enhancing the exfoliation and size reduction.[67]

3.1.4. Micro-explosion and freezing-and-thawing methods. MQDs have also been synthesized using an efficient and innovative method called micro-explosion. In this approach, $Ti_3C_2T_x$ is intercalated by liquid nitrogen (L-N_2) and hot deionized water.[92] Constantly evaporating L-N_2 at room temperature, owing to its low boiling point (−196 °C), intercalates $Ti_3C_2T_x$ layers. By adding deionized water at high temperatures (100 °C), rapid gasification of the interlayer L-N_2 in a confined space occurs, resulting in micro-explosion due to temperature

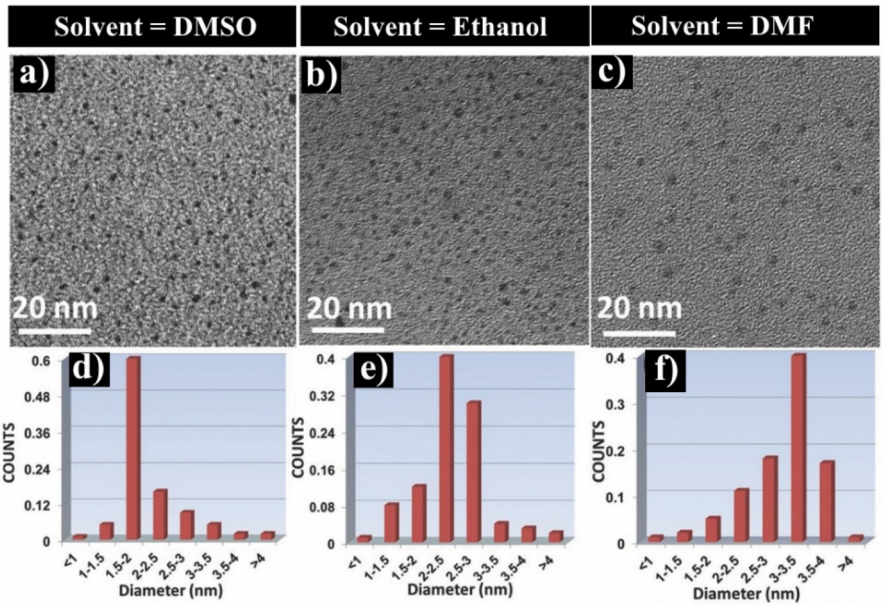

Fig. 4 TEM images and size distribution of (a and d) DMSO-MQDs, (b and e) ethanol-MQDs and (c and f) DMF-MQDs (reprinted with permission from Wiley, copyright © 2022).[67]

difference, forming $Ti_3C_2T_x$ QDs with a lateral size and diameter of 7.23 nm with 5 nm, respectively (Fig. 5a).[92]

The freezing-and-thawing method is one of the newest methods that is commonly applied in the exfoliation of boron nitride nanosheets,[94] metal–organic nanosheets,[94] graphene oxide (GO),[94] and antimony triselenide (Sb_2Se_3).[94] To prepare Ti_3C_2 QDs with 1.7 nm average lateral size, the solution of Ti_3C_2 experiences freezing (at −38 °C for 3 hours) and thawing (at room temperature) cycles, followed by sonication to convert MXene flakes to QDs. By repeating freezing and thawing cycles, water is solidified and expanded multiple times, creating a honeycomb structure. This structure boosts van der Waals breakage by exerting extrusion force, thus promoting nanosheets peeling and QDs formation.[35]

3.1.5. Other methods. Apart from the abovementioned methods, some new approaches have been introduced to prepare MQDs. Potential static is one of the them that enables synthesizing Cl, N doped-Ti_3C_2 QDs with a lateral size of

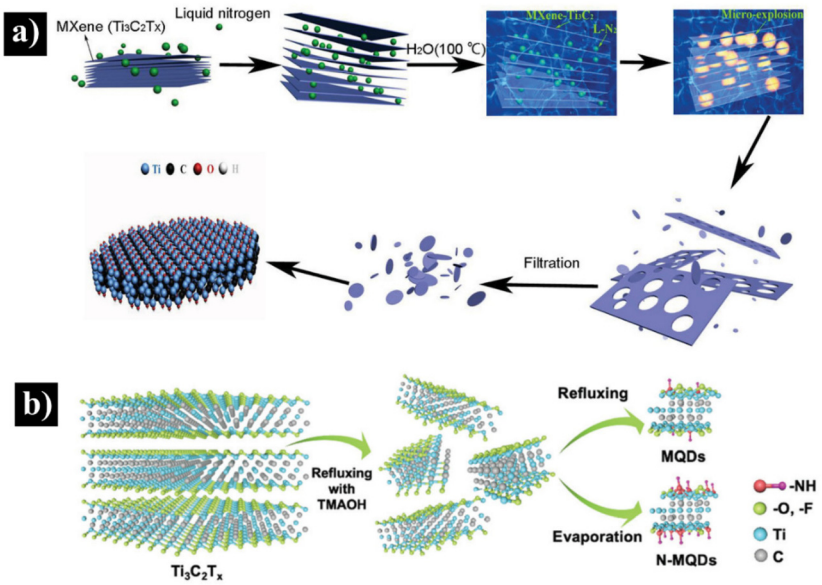

Fig. 5 (a) Synthesis of $Ti_3C_2T_x$ MQDs by the micro-explosion method (reprinted with permission from Wiley, copyright © 2020).[92] (b) Synthesis of $Ti_3C_2T_x$ and N-$Ti_3C_2T_x$ MQDs by reflux methods (reprinted with permission from The Royal Society of Chemistry, copyright © 2022).[93]

3.4 nm. This was done by applying a specific amount of voltage to the electrochemical cell, comprising Ti_3AlC_2 as a working electrode, Pt wire as a counter electrode, and mixture of TMAOH and NH_4Cl as the electrolyte.[75] Reflux is another method that was used to prepare a broad spectrum of QDs, including nitrogen-doped carbon (NDC),[73] CdS,[76] CA-capped CdTe,[76] TiO_2,[78] and Cu_3BiS_3 QDs.[80] The key feature of this method is that the condenser prevents solvent vapors from escaping, while a circulating coolant, such as water, condenses the vapor and returns it into the reaction vessel.[83,95] This method has been employed to synthesize $Ti_3C_2T_x$ QDs by processing of Ti_3C_2 and TMAOH at 110 °C for a day (Fig. 5b).[83] The microwave method, which has been used for the synthesis of a wide range of QDs, has also been found effective in forming bare and doped MQDs. For instance, $Ti_3C_2T_x$ nanosheets turned into QDs by microwave heating at 560 W for 3 min and subsequent refluxing.[84,96] Acoustomicrofluidic is a chemical-free method that can be used to synthesize MQDs with a size of 7.8 nm and thickness of 1.1 nm.[97] This approach utilizes surface-reflected bulk waves to minimize oxidation, causing the material to nebulize and form aerosol droplets, which then condensed within the glass enclosure. The wave has a surface acceleration of 10^8 m s^{-2} and strong evanescent electric field of 10^7 V m^{-1}, facilitating exfoliation through protonation of lithium fluoride into hydrofluoric acid. The influence of nebulization cycles was examined by performing 1, 5, and 10 cycles, which transformed nanosheets to ultrathin QDs by reducing thickness and lateral size. The average thicknesses decreased from 8.5 nm to 4.8 nm and 1.1 nm, while the mean lateral sizes shrank from 68.4 nm to 27.1 nm and 10.7 nm, respectively. Although these results demonstrate that the size and morphology of the material can be precisely tuned by controlling the number of nebulization cycles, no mechanism was proposed to explain these observations.[97]

3.2. Bottom-up approaches

Compared to top-down methods, which offer a wide range of synthesis designs for MQDs preparation, only a few bottom-up processes have been proposed for producing MQDs, primarily Mo_2C QDs. Various studies have demonstrated the great potential of molten salts to synthesis various QDs, such as polymeric carbon nitride,[85] $In_{1-x}Ga_xP$, $In_{1-x}Ga_xAs$, and Mo_2C. In the case of the latter, NaCl is mixed with Mo-containing precursor and sucrose in ethanol/H_2O (4 : 1), followed by continuous NaCl nanocubic crystal precipitation and stacking growth. Subsequently, sucrose and the Mo-containing precursor are confined within the interstices of the NaCl crystals. Finally, heat treatment at 800 °C for 2 hours in argon results in the formation of molybdenum carbide nanodots embedded in ultrathin carbon nanosheets (Mo_2C/C NSs with an average size of 2–3 nm) (Fig. 6a).[37]

Pyrolysis is a temperature-induced method, which creates QDs by chemical decomposition of organic materials in the absence of oxygen.[40] To prepare Mo_2C nanoparticle-decorated carbon polyhedrons, Mo/ZIF-8, formed by the hydrothermal treatment of the mixture of precursors, is heated for 2 hours in an argon-filled tube furnace at 700 °C. As a result of pyrolysis, Mo/ZIF-8 framework is transformed into a carbon matrix, simultaneously forming Mo_2C NPs less than 5 nm (Fig. 6b).[42]

Spray-drying is another process for preparing particles, in which a solution of raw materials is pressurized to form droplets and then dried at high temperatures to form particles.[44] This method was used to prepare Mo_2C QDs-decorated CNT networks.[98] As illustrated in Fig. 6c, an ultrasonication-treated ammonium molybdate tetrahydrate in CNT solution is spray-dried at a flow rate of 1 L h^{-1} at 170 °C, followed by carbonization in the quartz tube to complete the procedure.[98]

4. Properties

MQDs possess key properties, including high colloidal, chemical, and photostability, making them promising candidates for various applications, including biomedicine, sensing, and optoelectronics. We aim to highlight two interesting properties biocompatibility/cytotoxicity and optical behavior which highly influence the performance of biomedical and optoelectronic devices.

4.1. Biocompatibility and cytotoxicity

MQD with excellent *in vitro* and *in vivo* biocompatibility have unlocked new opportunities in biomedical engineering across various fields, including transplantation medicine, cancer photo-thermal therapy, and bio-imaging.[47] This section addresses recent advancements in bioinertness, bioactivity, biodistribution, cytotoxicity, and cellular dysregulation caused by oxidative stress, collectively referred to under the broad term biocompatibility.

4.1.1. *In vitro* assays. A crucial step in evaluating the biomedical potential of MQDs is assessing their compatibility with biological systems. This evaluation involves identifying challenges and advancements in understanding the biocompatibility of MQDs, emphasizing the importance of prioritizing human health and safety. For example, Ti_3C_2 QDs exhibit good biocompatibility with multiple therapeutic cell types, such as Mesenchymal Stem Cells (MSCs), induced Pluripotent Stem Cells (iPSCs)-derived Fibroblasts (iPS-Fibs), and human immune cells.[48,49] Some studies have shown the potential of MQDs to enhance cell survival and function.[51] MSCs and iPS-Fibs are particularly promising due to their inherent capacity to repair and regenerate damaged tissues through paracrine actions and versatile differentiation.[48,49] To investigate the *in vitro* biocompatibility of MQDs, different methods, including calcein AM/EthD-1 cell viability assay, flow cytometry, fluorescence microscopy using calcein AM and 7-AAD, LDH cytotoxicity assay, and cell proliferation assay have been employed. It is also important to evaluate the cytocompatibility of MQDs at different concentrations over both short-term (24 h) and long-term (1 week) periods.[51]

Materials selection is a crucial factor influencing the biocompatibility of MQDs. For instance, $Ti_3C_2T_x$ can elevate intracellular reactive oxygen species (ROS), leading to oxidative

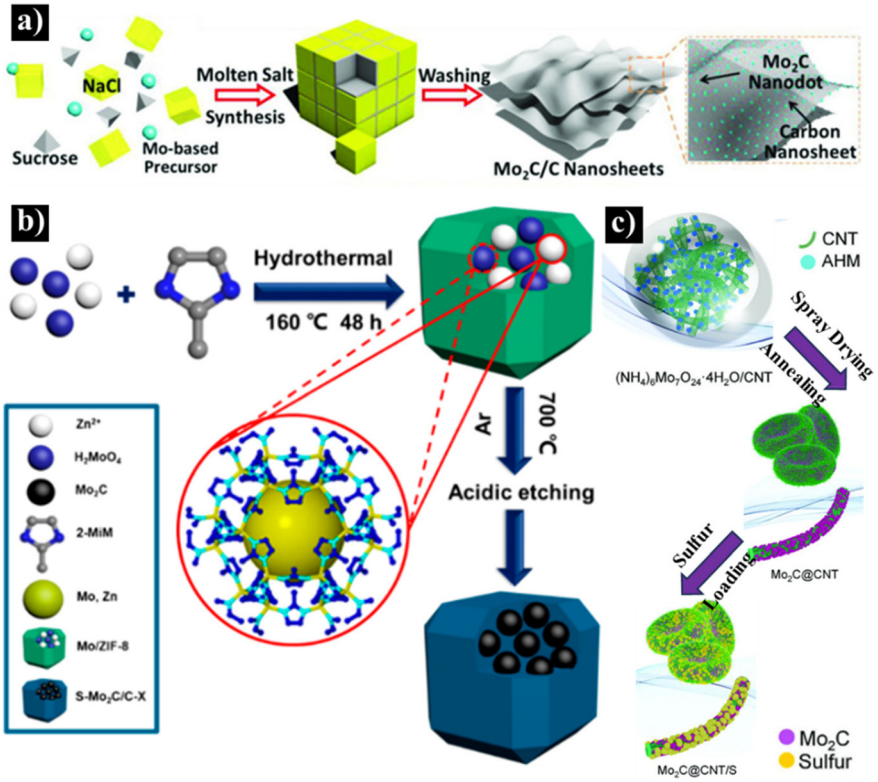

Fig. 6 (a) Molten salt synthesis of Mo_2C/C nanosheets (reprinted with permission from Wiley, copyright © 2018).[37] (b) Pyrolysis synthesis of Mo_2C-decorated carbon polyhedrons (reprinted with permission from American Chemical Society, copyright © 2018).[42] (c) Spray-drying synthesis of Mo_2C QDs-decorated CNT networks (reprinted with permission from Wiley, copyright © 2021).[98]

stress with both beneficial and detrimental effects. While it can be used to treat tumors and bacterial infections,[52] it also has the potential to cause cellular damage.[53] In contrast, Ti_2N QDs demonstrate no cytotoxic effects on human embryonic kidney cells, U87 human malignant glioma cells, or 4T1 murine mammary carcinoma cells (*in vitro*) in a standard 3-(4,5-dimethyl-2-thiazolyl)-2,5-diphenyl-2*H*-tetrazolium bromide (MTT) cytotoxicity assay.[23] The destruction of cancer cells using Ti_2N QDs only occurs when they are exposed to near-infrared (NIR) laser irradiation for a short duration, a result that could not be achieved with either MQDs or NIR irradiation alone. This phenomenon positions Ti_2N as a promising candidate for photothermal cancer therapy. Fig. 7a shows the confocal fluorescence images after the treatment with calcein AM (green) and PI (red) for live and dead cells, respectively.[23]

In addition to materials selection, surface functional groups significantly influence the biocompatibility and bioactivity of MQDs. For instance, the surface of $Ta_4C_3T_x$ MQDs, enriched with negatively charged functional groups, enhanced bioactivity by facilitating interactions between the QDs and cells.[24,54] In another study, it has been demonstrated that the surface charge of $Ta_4C_3T_x$ MQDs varies with pH, enabling these QDs to escape endosomes shortly after cellular uptake, and localize near the nucleus.[24,55]

The concentration of MQD colloidal solution is another important factor that greatly influences its biocompatibility. In one study, various concentrations of $Ta_4C_3T_x$ MQDs, ranging from 2 μg mL^{-1} to 100 μg mL^{-1} in PBS, were applied in cultures of human umbilical vein endothelial cells (HUVECs). Using CellROX green fluorescent dye and the CellEvent fluorescence-based apoptosis detection kit, the researchers found that these concentrations neither induced intracellular oxidative stress nor activated caspase-3 and caspase-7, which are key mediators of the cell death.[24] No significant changes in cellular cytotoxicity or cell growth were observed over a seven-day period.[24] It is noteworthy that most of the aforementioned findings are predominantly based on laboratory *in vitro* experiments; hence, *in vivo* investigations using diverse disease models and real clinical conditions are needed to fully understand the performance of MQDs in living organisms.

4.1.2. *In vivo* assays. Researchers actively explore the *in vivo* performance of MQDs to address concerns about their potential toxicological effects. For instance, the long-term toxicity of Ti_2N QDs used as nanoagents in photothermal therapy (PTT), was systematically evaluated by monitoring mice at a dose of 20 mg kg^{-1} over 20 days. Detailed blood biochemistry assays and histological examinations revealed no signs of organ damage in the treated group compared to the control group (Fig. 7b). Therefore, within the observed timeframe, the inves-

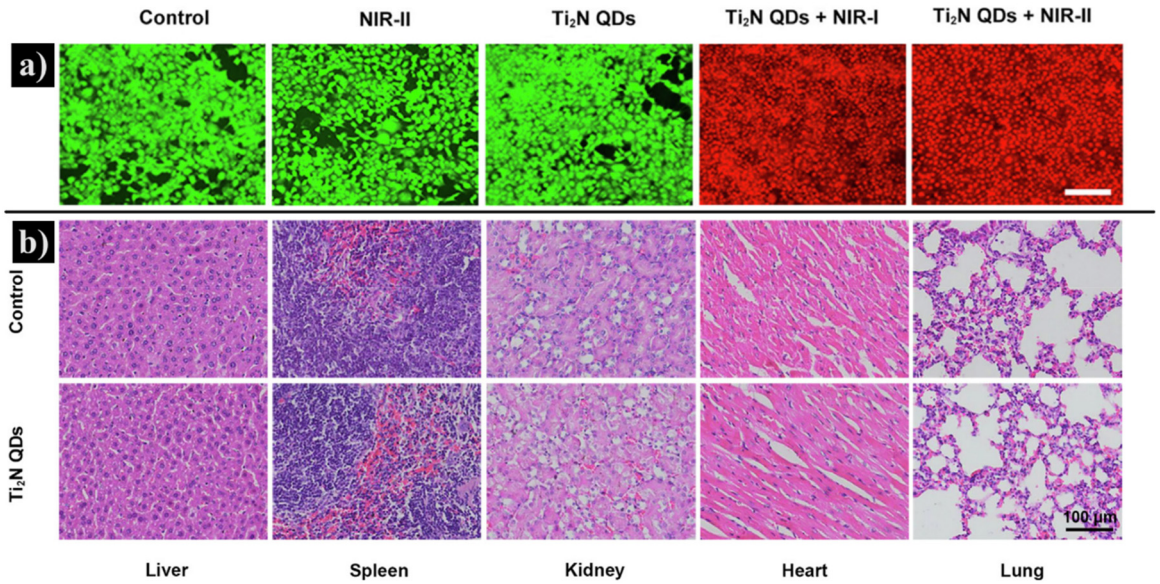

Fig. 7 (a) Confocal images showing calcein-AM staining for live cells (green) and PI staining for dead cells (red). The scale bar is 100 μm. Injection (reprinted with permission from Elsevier, copyright © 2020).[23] (b) H&E-stained images of major organs of the Ti_2N QDs treated mice at 20 days post-injection (reprinted with permission from Elsevier, copyright © 2020).[23]

tigated concentrations of Ti_2N QDs did not elicit a significant toxic response.[23]

Biodistribution is also crucial for MQD applications in living organisms. Encapsulation of MQDs within stable substances like albumin has been explored,[56] along with other techniques; for example, Ti_3C_2 MQDs, used as photothermal agents for cancer treatment, gain improved dispersion and biocompatibility by ultrasonic oxidation, introducing hydrophilic groups without surface modification.[58] Biodistribution studies on Ti_2N QDs for photothermal cancer therapy determined accumulation of the MQDs in tumors, the liver, and kidneys. The enhanced permeability and retention effect considerably promoted the uptake of MQDs in cancerous areas, improving the PTT efficacy. The high content of Ti_2N within the liver primarily resulted from the clearance activity of the reticuloendothelial system, whereas the kidney absorption might be associated with potential renal elimination. The amounts of Ti_2N QDs detected in the feces and urine of mice were similar to those accumulated in the kidney that were metabolized, showing a high clearance efficiency. Therefore, it was concluded that the long-term toxicity concerns for Ti_2N QDs, as inorganic PTT nanoagents, are less significant.[23]

4.2. Optical properties

MXenes have garnered significant attention for their exceptional electrical conductivity (up to 20 000–24 000 S cm^{-1} (ref. 59)). However, their PL quantum yield remains extremely low.[61] This raises the question: Can the transition from a 2D structure to a QD morphology enhance the optical properties of MXenes? Through what mechanisms?

The answer is yes. The 2D to QD transformation induces various fascinating optical characteristics. First, QDs exhibit a strong quantum confinement effect, especially when their size falls below the Bohr radius.[62] In this case, the photogenerated excitons, *i.e.*, a pair of electron and hole, are tightly confined within the QD, increasing the probability of radiative recombination and enhancing photoluminescence quantum yield (PLQY). Second, QDs feature tunable bandgap energy.[62] As the lateral size of QDs decreases, the highest occupied molecular orbital (HOMO)–the lowest unoccupied molecular orbital (HOMO–LUMO) gap gradually widens, the absorption edge is blue-shifted, and the continuous spectral bands change to sharp spectral peaks, resulting in a stronger quantum confinement effect.[62] Beyond the quantum confinement effect, surface states and edge effects with various F–, OH–, and O– functional groups play an important role in tuning the optical properties of QDs.[63]

To quantitatively assess the optical properties of MQDs, ultraviolet-visible spectroscopy (UV-Vis) and PL spectrometry have widely been employed, providing valuable insights into the absorption edge, emission peak, and bandgap energy (E_g). Regarding absorbance, Ti_3C_2 MQDs have an absorption band between 245–275 nm related to π–π* electronic transitions.[65] In some cases, an absorption peak between 300–320 nm was also observed, corresponded to the n–π* transition.[65] In terms of PL, the strongest emission peak typically appears at ~460 nm when QDs are optically excited at 365 nm (Fig. 8a).[65] This emission may be controlled by the quantum confinement effect or edge defects,[65] leading to excitation-dependent or excitation-independent PL, respectively. While increasing the excitation wavelength shifts the emission peak to longer wavelengths in the former case, there is no shift in the emission peak in the latter case. Although the underlying mechanisms of this phenomenon have thoroughly been explored in other

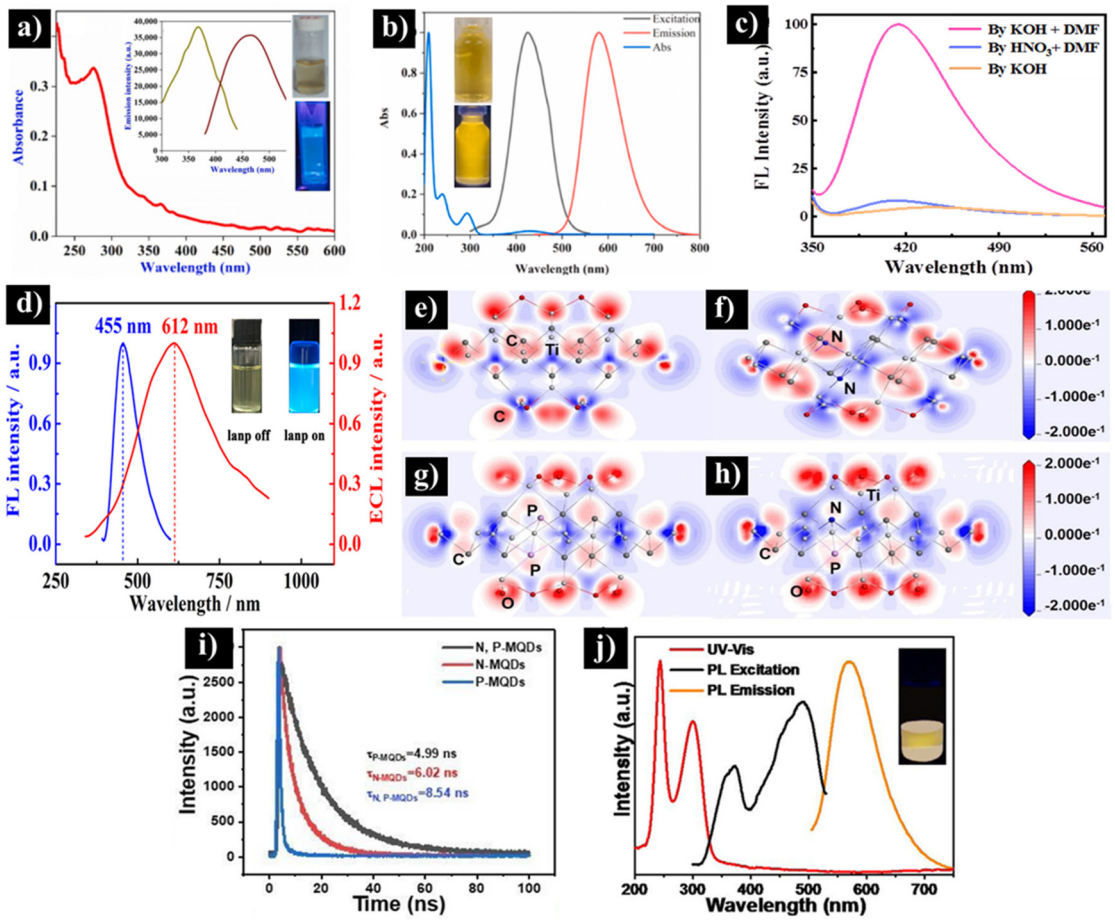

Fig. 8 (a) UV–vis absorption spectrum of Ti_3C_2 MQDs. The inset shows the emission and photographs of fluorescence spectra (reprinted with permission from Elsevier, copyright © 2022).[99] (b) UV-Vis absorption spectrum and PL spectrum of N-doped MQDs (reprinted with permission from Elsevier, copyright © 2021).[100] (c) The emission spectra of Ti_3C_2 MQDs prepared in different solvents (reprinted with permission from Elsevier, copyright © 2022).[2] (d) Normalized ECL emission spectrum (red curve) of N-Ti_3C_2 QDs in 10 mM $S_2O_8^{2-}$ solution (reprinted with permission from Elsevier, copyright © 2022).[101] The charge density difference of (e) Ti_3C_2 MQDs, (f) N-functionalized Ti_3C_2 MQDs, (g) P-functionalized Ti_3C_2 MQDs, and (h) N, P functionalized MQDs. (i) PL decay spectra of doped MQDs (reprinted with permission from Royal Society of Chemistry, copyright © 2019).[102] (j) UV-vis and PL spectra of SN-MQDs (reprinted with permission from Elsevier, copyright © 2019).[9]

QDs like SiC, there is a lack of in-depth investigation into this behavior for MQDs. In terms of bandgap energy, studies have revealed that by changing the lateral size of MQD, their bandgap energy can be tuned between 0.1–3.52 eV (Table 2).[46]

There are several factors that play a crucial role in optoelectronic properties of MQDs, with the synthesis method being one of the most important. For example, the ultrasonication-assisted HF process in various organic solvents was among the earliest approaches used for synthesizing fluorescent MQDs. While MQDs synthesized in dimethylformamide (DMF) had an average size of 2.75 nm with a PLQY of 4.5%,[68] using DMSO reduced the MQD size to less than 2 nm and enhanced the PLQY to 7.7%.[70,72] Compared with the ultrasonication method, the solvothermal process in organic solvents exhibited different results: a brownish solution of $Ti_3C_2T_x$ QDs in DMSO (D = 1.8 nm) exhibited an emission wavelength and PLQY of 570 nm and 4.1%, respectively; a yellowish QDs in DMF (D = 3.3 nm) and colorless QDs in ethanol (D = 2.5 nm) indicated lower emission wavelengths at 436 and 370 nm but higher PLQYs at 10.7% and 6.9%, respectively.[67] These size and optical property differences were attributed to the polarity, boiling temperature, and oxidation capability of the solvents. Solvents with higher polarity and lower boiling temperature normally paves the way for 2D to QD transformation, due to the strong 2D/solvent interaction and higher gas pressure, leading to smaller QDs with higher PLQY. However, $Ti_3C_2T_x$ QDs showed a reverse trend in terms of PLQY since DMSO formed the smallest QDs with the lowest PLQY because the solvent had the highest intensity of oxygen-containing functional groups (*e.g.*, C–O–C, C═O, and Ti–O). This oxidation degraded $Ti_3C_2T_x$ into anatase or rutile TiO_2 NCs, leading to a decrease in PLQY.[67]

Beyond the type of solvents, the processing time and temperature significantly influence the optical properties of MQDs. Studies have shown that extending the solvothermal duration from 1 hour to 8 hours results in a blue shift of the emission

Table 2 Effects of functionalization on the optical properties of MQDs

MXene QDs	Size* l (nm) and t (nm)	λ_{abs} (nm)	λ_{exc} (nm)	λ_{em} (nm)	PLQY (%)	τ (ns)	Ref.
TiCN	l = 2.7 t = 3.2	232	310	400	—	—	103
Ti_3C_2	l = 2.75	—	365	445	4.5	—	68
Ti_3C_2	l = 1.75	—	320	410	7.7	—	70
N-Ti_3C_2	l = 1.75	239, 293, 427	420	580	5.42	—	100
(1) N-Ti_3C_2	(1) l = 3.14, t = 0.93	234, 295	—	—	(1) 10.3	(1) 6.02	102
(2) P-Ti_3C_2	(2) l = 2.97, t = 0.85		—	—	(2) 2.4	(2) 4.99	
(3) N, P-Ti_3C_2	(3) l = 2.73, t = 0.71		480	560	(3) 20.1	(3) 8.54	
N-Ti_3C_2 QDs	l = 3.4 t = 0.5–1.3	229, 290	369	448	DMF = 11.3, ethanol = 1.09, H_2O = 0.34	—	104
N-Ti_3C_2	l = 2.3	—	335	420	14.46	5.24	61
N-Ti_3C_2	l = 8.63	—	330	427	N-Ti_3C_2 (APTES) = 15.4 Ti_3C_2 = 6.7	6.86	64
S, N co-doped Nb_2C	l = 3.8 t = 1.2	—	390	520	17.25	7.12	2
N-doped Ti_3C_2	l = 3.4	—	360	470	18.7	7.06	36
N, B-Ti_3C_2	l = 2.25	220, 280	335	448	18.9	4.39	101
GSH-Ti_3C_2	l = 2.5	300	337	430	21	—	105
PLL-protected Ti_3C_2	l = 3	—	330	415	22	—	64
N-doped Ta_4C_3	l = 2.6	234, 293	380	450	23.4	7.92	106

* Average lateral size (l), thickness (t), quantum dot (QD), absorption wavelength (λ_{abs}), excitation wavelength (λ_{exc}), emission wavelength (λ_{em}), excitation wavelength (λ_{exc}), carrier lifetime (τ), photoluminescence quantum yield (PLQY), glutathione (GSH), ε-poly-L-lysine (PLL).

peak and an increase in emission intensity of nitrogen-doped Ti_3C_2, attributed to the quantum size effect.[74] Another study indicated that decreasing the hydrothermal temperature from 150 °C to 100 could increase the PLQY of the Ti_3C_2 MQDs from 7.9% to 9.9%, showing the optimized temperature value is dependent on type of MQDs.[86] However, no mechanism was provided for this trend. Anyway, despite the capability of synthesis methods in preparing fluorescent MQDs, the PLQY yet remained quite low.

Doping has been introduced as an efficient way to modify the electronic structure and properties of MQDs. Here, nitrogen is the commonly used dopant, found remarkably effective in improving various properties.[100] It has revealed that N-doping of Ti_3C_2 QDs changes the absorption spectrum by adding a new absorption peak at 427 nm which corresponds to the n–π* transition of C=N (Fig. 8b). Consequently, a new yellow fluorescence peak at 580 nm appears. Besides, the fluorescence intensity of N-Ti_3C_2 QDs is highly stable in the presence of various compounds (*e.g.*, 1.0 M NaCl)[107] due to the abundant hydrophilic groups, providing excellent water solubility.[107]

More importantly, nitrogen doping can remarkably boost the PLQY which is dependent on many factors. First of all, not all dopants are capable of improving the PLQY. For instance, by N-doping of MQDs, the PLQY and carrier lifetime could reach 10.3% and 6.02 ns, respectively, significantly higher than the phosphorous (P)-doped MQDs (2.40% and 4.99 ns).[2,90,102,108] Regarding N-doping, the selected solvent plays an important role. Using DMF as both a nitrogen doping source and a medium for the solvothermal process, the PLQY of N-Ti_3C_2 QDs reached 11.13%.[104] This improvement was related to the reaction of dimethylamine, derived from DMF decomposition, and carboxylic groups of QDs. In another study, a combination of DMF and KOH was used to synthesize N-Ti_3C_2 QDs with a PLQY of 14.46%.[2] This value is significantly higher than that of QDs prepared by HNO_3 and KOH (less than ~2% for both) (Fig. 8c), owing to the nitrogen doping confirmed by the detection of C–N–C and N–H bonds in X-ray photoelectron spectroscopy (XPS). 3-Aminopropyltriethoxysilane (APTES) was another N-containing source that succeeded in enhancing the PLQY to 15.4%, attributed to the surface-passivating amino groups, which exert a strong electron-donating effect at the edges of the MQDs.[64] To further enhance the PLQY of nitrogen-doped Ti_3C_2 QDs to 16.9%, MQDs were solvothermally synthesized by adding diethylenetriamine to DMF.[74] Compared to diethylenetriamine, ethylenediamine was more effective in enhancing PLQY to 18.7% by prolonging the carrier lifetime to 7.06 ns due to the gap states formed close to LUMO.[36] High-resolution N 1s XPS spectrum determined four new peaks at 397.9, 399.5, 400.2, and 401.2 eV, corresponding to the Ti–N band, pyrrole-like nitrogen (C=N), N–H, and graphitic nitrogen C–N, respectively. Ethylenediamine also demonstrated electro-chemiluminescent (ECL) properties, exhibiting a ECL emission peak at 612 nm with a quantum yield of 1.58%. This emission was attributed to electronic injection into surface traps within the QDs' band gap (Fig. 8d).[101] Similar to Ti_3C_2, ethylenediamine enhanced the optical properties of Ta_4C_3 by forming –NH_2 and C–N bands, resulting in a PLQY of 23.4%.[106] Additionally, the formation of –NH groups on the surface of N-MQDs improved pH resistance.[106]

Co-doping offers a greater potential for enhancing the optical properties of Ti_3C_2 QDs. For instance, Q. Guan *et al.*[102] have shown that simultaneous doping of monolayer Ti_3C_2 QDs

by nitrogen and phosphorus enhance PLQY to 20.1%. High-resolution N 1s and P 2p XPS spectra have indicated the characteristic peaks of NO_3^- (407.2 eV), N–Ti (396.1 eV), C–N (398.2 eV), N–H (400.7 eV), P–O (133.9 eV), and PO-C (134.8 eV). The electron density difference (EDD) distribution underscores the electron transfer between bonding atoms (Fig. 8e–h). In this image, the blue and red isosurfaces represent electron-depleted and electron-accumulated regions, respectively. Oxygen sites, with high electronegativity, appear red, while phosphorus atoms show blue electron-depleted regions. The enhanced blue intensity at P atoms in P, N-doped Ti_3C_2 QDs indicates electron transfer from P to N, leading to improved radiative recombination and optical performance.[102] The trend of carrier lifetime in N, P-Ti_3C_2 QDs, N-Ti_3C_2 QDs, and P-Ti_3C_2 QDs (8.54 ns, 6.02 ns, and 4.99 ns, respectively) also confirm the photoluminescent enhancement (Fig. 8i).

Besides the P and N dopant pair, other dopants have also been explored to improve the optical properties of Ti_3C_2 QDs. For instance, nitrogen and boron co-doped Ti_3C_2 MQDs (N, B-Ti_3C_2 MQDs) were hydrothermally prepared from ammonia and boric acid, exhibiting good water solubility, strong stability, and high optical characteristics.[109] Co-doped S, N Ti_3C_2 MQDs showed the most redshifted PL emission of 580 nm as well as the highest PLQY of 28.12%.[9] Notably, the PLQY value was higher than that of N-Ti_3C_2 MQDs (8.33%) and S-Ti_3C_2 MQDs (7.78%), which correlated with the carrier lifetime enhancement from 4.67 ns for S-doped MQDs and 5.81 ns for N-doped MQDs to 7.74 ns for S, N-doped MQDs (Fig. 8j). Co-doping was also found effective in tuning the optical properties of other MQDs. For instance, co-doped Nb_2C QDs (S, N-doped Nb_2C MQDs) with green excitation-dependent emission at 520 nm indicated a high PLQY of 17.25%.[2] Based on the S 2p XPS spectra, the peaks located at 168.2 eV and 169.3 eV, correspond to different oxidized sulfur forms of SO_x (x = 2–4) bond, typically associated with the surface of the Nb_2C layers.

Co-doped MQDs also offer higher PLQY combined with improved pH resistivity. Studies indicated that the fluorescence intensity of N, B-Ti_3C_2 QDs remained constant when pH was in the range of 3–13, showing high pH-resistive behavior of co-doped QDs.[109] In contrast, the N-doped MQDs exhibited emission stability only within the pH range of 4–9, attributed to the presence of both amino and hydroxyl groups on the surface of QDs.[108] Beyond this range, the intensity quenched out in both acidic and basic solutions. In alkaline solutions, deprotonation of hydroxyl groups forms O^- groups on the MQDs surface. Consequently, oxidation of MQDs is accelerated and the PL intensity is reduced.[109]

Surface functionalization of MQDs with various molecules was also found effective in enhancing the PLQY of MQDs. This improvement is highly dependent on the synthesis procedure and type of molecules. In terms of synthesis methods, the hydrothermal reaction plays a critical role in the synthesis of fluorescent MQDs, as simple stirring of a mixture of molecules with Ti_3C_2 has been shown to be ineffective.[39] Regarding the type of molecules, while the PLQY of BSA@MQDs and polyethyleneimine (PEI)-MQDs were 8% and 7.13%, respectively, an aqueous solution of GSH-Ti_3C_2 MQDs demonstrated a much higher PLQY of 21%. Although PEI successfully functionalized the surface of QDs by forming amide and N–H bonds,[43] GSH increased the surface defect sites and enhanced the PLQY more effectively.[105]

It is noteworthy that molecule-passivated MQDs exhibit intriguing differences in their optical responses to pH tuning. Studies have revealed that the optical properties of BSA@MQDs and PEI@MQDs are highly sensitive to pH changes.[39] The highest emission of BSA@MQDs is attained at pH = 2, and increasing the pH drastically reduces the PL intensity. At the low pH value, the full protonation of BSA amine groups enhances vibrational coupling with hydroxyl functional groups, while deprotonation at higher pH levels leads to the formation of nonradiative recombination centers associated with increased surface defects.[39] A similar trend has been observed in PEI-functionalized QDs, as confirmed by time-resolved photoluminescence (TRPL) analysis.[43] While the slow decay time constant (τ_1), associated with intrinsic transitions of Ti_3C_2 MQDs, remains unchanged across different pH levels, the fast decay time constant (τ_2), related to emissions from surface defect sites, decreases with increasing pH. This reduction is explained by the deprotonation of surface defects, which transforms luminescent surface defects into non-luminescent ones, thereby diminishing the emission intensity of Ti_3C_2 MQDs. In contrast, GSH-Ti_3C_2 MQDs,[105] UA@Ti_3C_2 MQDs,[88] and PLL-protected Ti_3C_2 MQDs exhibit stable PL intensity across a wide pH range of 1–13. This stability is attributed to the superior surface passivation provided by the functional molecules, effectively shielding the QDs from pH-induced surface changes.[105,110]

5. Applications

Leveraging the exceptional optical properties and inherent biocompatibility of MQDs, their utility has been demonstrated across a diverse range of applications. In this section, we will cover a wide range of applications, commencing with sensing technologies and highlighting the effective detection of various analytes. Subsequently, we will evaluate the significant impact of MQDs on the performance enhancement of optoelectronic devices, energy conversion systems, and biomedical applications.

5.1. Sensing

- **Mechanisms**

QDs have revolutionized nanotechnology, offering tunable optical and electronic properties, including broad excitation spectra, adjustable emission properties, and intense fluorescence with long-term photostability driven by quantum confinement effects. This versatility has propelled advancements in various fields, such as optoelectronics, bioimaging, and sensing.[6,107,111] Despite these merits, QDs face several limitations, particularly in sensing applications. First, their applica-

bility in fluorescence detection is hindered by inherent biological toxicity, particularly in Pb- and Cd-based QDs.[2,5,6,11] Second, many QDs are soluble only in toxic, nonpolar organic solvents, restricting their direct use in aqueous systems. Additionally, certain QDs, such as CdS, degrade under acidic conditions (pH < 7.0), resulting in the loss of their fluorescence properties over time.[5] Therefore, MQDs with strong pH resistance in certain wavelengths and stable optical properties in aqueous solutions have gained remarkable attention in recent years.[35] By taking advantage of various optical, electrochemical, and electrochemiluminescence (ECL) sensing techniques, MQDs have manifested great potential for use in sensors.[88]

So far, optical sensing by fluorescence quenching has been the one of the most used and efficient techniques.[7] Fluorescence quenching refers to the fluorescence intensity reduction of a fluorophore due to different intermolecular interactions, such as excited state reactions, molecular rearrangements, Förster resonance energy transfer (FRET), photoinduced electron transfer (PET), inner filter effect (IFE), ground state complex formation, and collisional quenching.[7] IFE, FRET, and PET are the mechanisms that have been widely utilized for sensing. The IFE is a non-specific mechanism (no probe-analyte interactions) that occurs when there is an overlap between the absorption spectrum of the quencher (analyte) and the excitation or emission spectra of the luminescent probe. This phenomenon reduces the amount of light available to excite the probe or diminishes the intensity of the emitted light, resulting in decreased luminescence.[7] FRET is a non-radiative energy transfer process that occurs when a donor molecule (the luminescent probe) in an excited state transfers energy to an acceptor molecule. This phenomenon occurs when there is an overlap between the emission spectrum of the donor and the absorption spectrum of the acceptor. Therefore, the efficiency of FRET highly depends on the donor–acceptor distance.[7] PET, which occurs over relatively longer distances than FRET, involves the transfer of an electron from the donor to the acceptor, forming a non-emissive complex and effectively quenching the probe's luminescence.[7] Therefore, the PET efficiency is influenced by the redox properties as well as the HOMO and LUMO of the donor and acceptor.[7]

Compared to single-emission, dual-emission reverse change ratio PL offers higher sensitivity and accuracy due to intrinsic signal amplification.[88] In dual-emission, the fluorescence of one component decreases while another's fluorescence significantly increases in the presence of the analyte. The ratio of the fluorescence intensities of the two components is then determined for quantitative analysis. For instance, curcumin (CUR) caused the fluorescence emission of Ti_3C_2 MQDs at 430 nm to be suppressed by the FRET, whereas CUR's fluorescence emission at 540 nm increased.[88]

Colorimetric sensors are another group of optical sensors that exhibit a distinct color shift in response to the analyte's reaction.[112] This color transition is detected by the naked eye or specific instrumentation to determine the change in intensity at a certain wavelength within the visible (400–800 mm) range.[112] For example, N, P-Ti_3C_2 MQDs showed a transparent-to-orange color change upon Fe^{2+} detection, demonstrating potential for portable sensors.[84] ECL has been widely used in analytical chemistry and bioassays due to its high sensitivity, low background noise, and compatibility with miniaturized devices.[72] In ECL, a voltage is applied to an electrode, which causes a redox reaction to occur and generates excited-state species. Then, these species emit light after returning to their ground state.[101] To assess the redox activity, cyclic voltammetry (CV) is used by sweeping the potential of the working electrode linearly with time and measuring the resulting current, providing information about redox potentials, electron transfer kinetics, and surface area.[113] By leveraging advanced sensing techniques and MQDs, researchers have successfully detected various types of targets. Table 3 provides a summary of the most recent advances in this field. The following sections offer a critical review on the application of MQDs in sensing.

5.1.1. Ion detection. MQDs have frequently been used to detect a broad spectrum of ions, particularly transition metals. For instance, Cu^{2+} is an essential element that serves as a catalytic co-factor for numerous enzymes, participating in redox reactions.[152] However, excessive intake causes severe liver and kidney damage, and it is associated with diseases like Wilson's and Alzheimer's.[152] Fluorescence quenching of MQDs has widely been utilized to detect copper. Feng *et al.*[74] used N-Ti_3C_2 MQDs to detect Cu^{2+}, observing a gradual decrease in emission intensity as the copper concentration increased up to 2000 μM. This fluorescence quenching was highly selective for Cu^{2+}, showing a significant response (~56%) compared to negligible interference from other metal cations. This selectivity was attributed to the strong interaction between Cu^{2+} and N-Ti_3C_2, which altered the energy states of the MQDs.[74] Feng *et al.*[74] demonstrated that the fluorescence quenching mechanism of N-MQDs was primarily static, by which the quencher forms a stable complex with the fluorophore. Other investigations underscored the role of surface passivating amino groups on S, N-Nb_2C MQDs and N, P-Ti_3C_2 MQDs in capturing Cu^{2+}.[102] These groups formed absorbent complexes on the surface of the MQDs, inducing electron–hole recombination annihilation and aggregation of the MQDs into larger complexes. These complexes resulted in strong fluorescence quenching with a robust linear relationship across different concentrations (Fig. 9a). The reported LOD for both S, N-Nb_2C MQDs and N, P-Ti_3C_2 QDs were at as low as 2 μM, revealing superior sensitivity relative to previous studies on Cu^{2+}.[102]

Fe^{3+} is another critical element that has widely been detected by MQDs *via* fluorescence technique because iron deficiency can lead to anemia, while excessive iron levels are associated with conditions such as hyperferremia and cancer.[121] Gao *et al.*[68] used fluorescence quenching of Ti_3C_2 MQDs to detect Fe^{3+} with a high sensitivity (0.6377 mM^{-1}) and low LOD (1.4 μM) through the electrostatic-induced aggregation mechanism.[68] Amino-rich Ti_3C_2 MQDs demonstrated even greater sensitivity, achieving a LOD of 0.17 μM with excellent linearity for Fe^{3+} detection, through binding of the metal

Table 3 Categorized applications for various MQD platforms and their features

Application	Platform	Features	Mechanisms	Ref.
miRNA sensing	Ti_3C_2 MQDs@Au nanobones heterostructure	• **Target**: miRNA-26a • **LOD**: 1.7 fM • **Linear range**: 5 fM–10 nM • **Selectivity**: miRNA-126, miRNA-155, miRNA-221 • **Sensitivity in real conditions**: human serum samples	ECL (short-distance electron transfer)	72
Proteins sensing	Amino-functionalized Ti_3C_2 MQDs	• **Target**: histidine • **LOD**: 2.1 nM • **Linear range**: 100–1000 nM • **Selectivity (Ni^+)**: Li^+, K^+, Ag^+, Na^+, Mn^{2+}, Zn^{2+}, Mg^{2+}, Ca^{2+}, and Al^{3+} • **Sensitivity in real conditions**: human serum samples	FL (IFE)	114
Organic acid sensing	Ti_3C_2 MQDs/TiO_2 inverse opal heterojunction	• **Target**: glutathione • **LOD**: 9.0 nM • **Linear range**: 0.1–1000 μM and 1 μM to 200 μM • **Selectivity**: AA, GLU, UA, Fe^{3+}	PEC	115
Other targets sensing	N-doped Ti_3C_2 MQDs@DAP	• **Target**: H_2O_2 • **LOD**: 0.57 μM • **Linear range**: 2–50 μM • **Selectivity**: DA, AA, Phe, Glu, Lys, L-Cys, Tyr, GSH, GSSG, K^+, Mg^{2+}, Ca^{2+}, Na^+, Zn^{2+}, Cd^{2+}, Fe^{2+}, Fe^{3+}, Ag^+, I^-, and Br^- • **Target**: xanthine • **LOD**: 0.24 μM • **Linear range**: 1–50 μM • **Selectivity**: adenosine, BSA, DA, AA, UA, cytidine, urea, Glu, K^+, and Ca^{2+} • **Sensitivity in real conditions**: human serum	Sensing: ratiometric fluorescence Quenching: PET	92
Proteins sensing	Ti_3C_2 MQDs-AuNPs	• **Target**: polynucleotide kinase • **LOD**: 2.7×10^{-5} U mL^{-1} • **Linear range**: 0.0001 to 10 U mL^{-1} • **Selectivity**: glucose oxidase (GOD), alkaline phosphatase (ALP), thrombin and lysozyme • **Sensitivity in real conditions**: HeLa cell lysate	ECL	71
miRNA sensing sensing	TiO_2 nanosheet arrays/Ti_3C_2 MQDs	• **Target**: MicroRNA-155 • **LOD**: 0.025 pM • **Linear range**: 0.1 pM–10 nM • **Selectivity**: miRNA-122, miRNA-141, miRNA-21	PEC	71
Proteins and amino acids sensing	ε-Poly-L-lysine-protected Ti_3C_2 MQDs	• **Target**: cytochrome c • **LOD**: 20.5 nM • **Linear range**: 0.2 to 40 μM • **Selectivity**: Trf, Lyz, Ova, Chy and BSA • **Target**: trypsin • **LOD**: 0.1 μg mL^{-1} • **Linear range**: 0.5 to 80 μg mL^{-1} • **Selectivity**: ALP, lysozyme, BSA, pepsin, thrombin and IgG • **Sensitivity in real conditions**: 50-fold diluted serum samples	Sensing: FL Quenching: IFE	110
Environmental pollutants sensing	Aptamer modified polyhedral oligomeric silsesquioxane-perovskite quantum dots (POSS-PQDs-Apt)/Ti_3C_2	• **Target**: *Vibrio parahaemolyticus* (VP) • **LOD**: 30 cfu mL^{-1}	Sensing: FL Quenching: FRET	116

Table 3 *(Contd.)*

Application	Platform	Features	Mechanisms	Ref.
		• **Linear range**: 10^2 to 10^6 cfu mL^{-1} • **Selectivity**: common bacteria, including *Listeria monocytogenes*, *Salmonella typhimurium*, *Escherichia coli*, and *Staphylococcus aureus* (all concentrations were at 10^5 cfu mL^{-1}) common ions and pesticide residues in water on the test results, including Na^+, K^+, Mg^{2+}, Ca^{2+}, and dimethoate. • **Sensitivity in real conditions**: real seawater samples		
Environmental pollutants sensing	N, B-doped Ti_3C_2 MQDs	• **Target**: tetracycline • **LOD**: 20 nM (using the smartphone: 45 nM) • **Linear range**: 0.2–20 μM (using the smartphone: 0.4–20 μM) • **Selectivity**: other antibiotics (KAN, CFX, CHL, NOR, OTC, and DOX) and some potentially coexisting substances (Na^+, Ba^{2+}, Ca^{2+}, Zn^{2+}, Fe^{3+}, BSA, Asp, Ser, Lys, Gys, His, GSH, GLU) • **Sensitivity in real conditions**: milk	Sensing: ratiometric fluorescence Quenching: IFE	109
Environmental pollutants sensing	Eu-doped Ti_3C_2 MQDs	• **Target**: tetracycline • **LOD**: 48.79 nM (using colorimetric method: 11.36 nM) • **Linear range**: 0–1000 μM • **Selectivity**: K^+, Ag^+, Li^+, Na^+, Mn^{2+}, Zn^{2+}, Ba^{2+}, Mg^{2+}, Ca^{2+}, Al^{3+} and antibiotics (Kana, Azi, Chl) • **Sensitivity in real conditions**: milk, and soil • **Target**: oxytetracycline (OTc) • **LOD**: 3.86 nM • **Linear range**: 100–1000 μM • **Target**: chlortetracycline (CTc) • **LOD**: 64.73 nM • **Linear range**: 100–1000 μM	Sensing: ratiometric fluorescence Quenching: FRET	65
Environmental pollutants sensing	N-doped Ti_3C_2 MQDs	• **Target**: Alizarin red • **LOD**: 1.21 μM • **Linear range**: 0–80 μM • **Sensitivity in real conditions**: actual water samples	Sensing: FL Quenching: IFE	100
Environmental pollutants sensing	Uric acid-capped Ti_3C_2 MQDs	• **Target**: 2,4,6-trinitrophenol • **LOD**: 9.58 nM • **Linear range**: 0.01–40 μM • **Selectivity**: NBA, BA, BD, NB, DNPH; PNPP, K^+, Cl^-, Ca^{2+}, Ba^{2+}, Cr^{3+}, Al^{3+}, NH^{4+}, S^{2-}, SO_3^{2-}, PO_4^{3-}, Mg^{2+}, Zn^{2+}, Mn^{2+}, Fe^{2+}, and NO^{3-}, Cu^{2+}, Pb^{2+}, and Fe^{3+}, Co^{2+} and Cd^{2+} • **Sensitivity in real conditions**: in lake and tap water	Sensing: FL Quenching: IFE	88
Other targets sensing	Ti_3C_2 MQDs	• **Target**: dopamine • **LOD**: 3 nM • **Linear range**: 0.01–20 μM • **Selectivity**: ascorbic acid, uric acid, glucose, NaCl, KCl and urea • **Sensitivity in real conditions**: DA hydrochloride injection purchased from a drugstore	—	113
Proteins and amino acids sensing	N-doped Ti_3C_2 MQDs	• **Target**: mucin 1 • **LOD**: 0.31 fg mL^{-1}	Sensing: ECL	101

Table 3 *(Contd.)*

Application	Platform	Features	Mechanisms	Ref.
		• **Selectivity**: carcinoem-bryonic (CEA), α-1-fetoprotein (AFP), human serum albumin (HSA) and hemoglobin (Hb) • **Sensitivity in real conditions**: serum samples		
Ions/organic acids sensing	N-doped Ti_3C_2 MQDs	• **Target**: chromium(VI) • **LOD**: 0.012 μM • **Linear range**: 0.1–500.0 μM • **Selectivity**: NH^{4+}, K^+, Na^+, Ag^+, Mg^{2+}, Ca^{2+}, Mn^{2+}, Zn^{2+}, Cu^{2+}, Cd^{2+}, Co^{2+}, Hg^{2+}, Fe^{2+}, Fe^{3+}, MnO_4 • **Sensitivity in real conditions**: in tap and Yudai Lake water • **Target**: ascorbic acid • **LOD**: 0.02 μM • **Linear range**: 0.1–500.0 μM • **Selectivity**: common amino acids (L-phenylalanine; L-tyrosine; L-/D-tryptophan; L-arginine; L-glutamate) and other potentially biomolecules (glutathione; glucose; uric acid; urea) • **Sensitivity in real conditions**: vitamin C tablets and lemon juice samples	Sensing: FL Quenching: IFE	107
Organic acids sensing	GSH-Ti_3C_2 MQDs	• **Target**: uric acid • **LOD**: 125 nM (ratiometric fluorescence), 200 nM (absorption) • **Linear range**: 1.2–75 μM (ratiometric fluorescence), 1.2–100 μM (absorption) • **Selectivity**: Try, Cys, urea, Nap, Kp, GSH, DA, GLU, NO^{3-}, SO^{4-}, Cl^-, UA • **Sensitivity in real conditions**: serum and saliva	Sensing: ratiometric fluorescence colorimetric (absorption) Quenching: FRET	105
Other targets/ions sensing	Ti_3C_2 MQDs	• **Target**: curcumin • **LOD**: 20 nM • **Linear range**: 0.05–10 μM • **Selectivity**: interfering ions (K^+, Na^+, Fe^{3+}, Al^{3+}, Ca^{2+}, Mg^{2+}, SO_4^-, Fe^{2+}, Zn^{2+}, Cl^-, and HPO_4^-), various amino acids, GSH, folic acid, and L-ascorbic acid, two carbohydrates (fructose and glucose). • **Target**: hypochlorite • **LOD**: 5 μM • **Linear range**: 25 to 150 μM and 150 to 275 μM • **Selectivity**: ClO^-: various oxidized anions and free radicals	Sensing: ratiometric fluorescence Quenching: FRET	117
Other targets sensing	N-doped Ti_3C_2 MQDs	• **Target**: H_2O_2 • **LOD**: 1.2 nM • **Linear range**: 5 to 100 nM • **Selectivity**: Na^+, K^+, Mg^{2+}, Ca^{2+}, Fe^{2+}, Zn^{2+}, and Al^{3+} ions	Sensing: FL	118
Other targets sensing	Ti_3C_2 MQDs	• **Target**: H_2O_2 • **LOD**: 5 nM	—	97
Ions sensing	N-doped Ti_3C_2 MQDs	• **Target**: Fe^{3+} • **LOD**: 2 μM • **Linear range**: 2 to 5000 μM • **Selectivity**: Na^+, Mg^{2+}, Cu^{2+}, K^+, Fe^{3+}, Mn^{2+}, Zn^{2+}, Ca^{2+}, Al^{3+}, Ce^{3+}, Cu^+ and Ni^{2+}	Sensing: FL	119
Ions sensing	N-doped Ti_3C_2 MQDs	• **Target**: Cu^{2+}	Sensing: FL	74

Table 3 *(Contd.)*

Application	Platform	Features	Mechanisms	Ref.
		• **Selectivity**: Na^+, K^+, Mg^{2+}, Ca^{2+}, Fe^{2+}, Fe^{3+}, Co^{2+}, Ni^{2+}, Zn^{2+}, Cd^{2+}, Pb^{2+}, Hg^{2+}, and Ag^+		
Ions sensing	Ti_3C_2 N, P-MQDs	• **Target**: Cu^{2+} • **LOD**: 2 μM • **Linear range**: 2–100 μM and 250–5000 μM • **Selectivity**: Zn^{2+}, Pb^{2+}, Na^+, La^{3+}, Mn^{2+}, Ni^{2+}, Ce^{3+}, Fe^{3+}, Ca^{2+}, K^+, Ag^+	Sensing: FL Quenching: IFE	102
Ions sensing	N-doped Ti_3C_2 MQDs	• **Target**: Cu^{2+} • **LOD**: 0.15 μM • **Linear range**: 0.5–100 μM • **Selectivity**: Hg^{2+}, Mn^{2+}, Ag^+, Cd^{2+}, Al^{3+}, Zn^{2+}, Mg^{2+}, Ca^{2+}, K^+, and Na^+ • **Sensitivity in real conditions**: water sample • **Target**: Fe^{3+} • **LOD**: 0.17 μM • **Linear range**: 0.5–100 μM • **Selectivity**: Hg^{2+}, Mn^{2+}, Ag^+, Cd^{2+}, Al^{3+}, Zn^{2+}, Mg^{2+}, Ca^{2+}, K^+, Na^+ • **Sensitivity in real conditions**: water sample	Sensing: FL Quenching: IFE	120
Ions sensing	TiCN MQDs	• **Target**: Fe^{3+} • **LOD**: 1.0 μM, 2.4 ± 0.1 μM (tap water) • **Linear range**: 2–400 μM and 500–800 μM • **Selectivity**: K^+, Cd^{2+}, Cu^{2+}, Fe^{2+}, Hg^{2+}, Mg^{2+}, Ni^{2+}, Pb^{2+}, Ce^{3+}, Mn^{2+}, Co^{2+}, Al^{3+}, and Zn^{2+} • **Sensitivity in real conditions**: tap water	Sensing: FL Quenching: IFE	103
Ions sensing	Ti_3C_2 MQDs	• **Target**: Fe^{3+} • **LOD**: 310 nM • **Selectivity**: cysteine, serine, arginine, ascorbic acid, dopamine, H_2O_2, Mn^{2+}, Fe^{2+}, Cu^{2+}, Ca^{2+}, Al^{3+}, Cd^{2+}, Co^{2+}, Cr^{3+}, Mg^{2+}, Na^+, Ni^{2+}, Pb^{2+}, Sn^{2+}, and Zn^{2+} • **Sensitivity in real conditions**: serum and seawater samples	Sensing: FL Quenching: IFE	70
Ions/physical parameters sensing	N-doped Ta_4C_3 MQDs	• **Target**: Fe^{3+} • **LOD**: 2 μM • **Selectivity**: NO_3^-, SO_4^-, Cl^-, Hg^+, Mg^+, Ce^+, Na^+, Ca^+, K^+, Fe^+, Cu^+, Ni^+, Ba^{2+}	Sensing: FL	106
Ions sensing	BSA@Ti_3C_2 MQDs	• **Target**: Fe^{3+} • **LOD**: 1.25 nM • **Linear range**: 0–150 μM • **Selectivity**: ascorbic acid, Sn^{2+}, Ca^{2+}, Ni^{2+}, Cd^{2+}, Pb^{2+}, Al^{3+}, Zn^{2+}, Ag^+, Cr^{3+}, Cr^{6+}, Cu^{2+}, Na^+, and K^+ • **Sensitivity in real conditions**: tap water samples	Sensing: FL Quenching: IFE	121
Ions/pH sensing	Amino-functionalized $Ti_3C_2T_x$ MQDs	• **Target**: Fe^{3+}/pH • **LOD**: 2 nM • **Selectivity**: K^+, Ca^{2+}, Na^+, Al^{3+}, Zn^{2+}, La^{3+}, Co^{2+}, Ni^{2+}, Cu^{2+}, Cd^{2+}, Ce^{4+}, Fe^{2+} • **Sensitivity in real conditions**: tap water samples	Sensing: ratiometric Fluorescence	108
Ions sensing	N-doped Ti_3C_2 MQDs	• **Target**: Co^{2+} • **LOD**: 0.21 μM • **Linear range**: 0.5–100 μM	Sensing: FL Quenching: IFE	2

Table 3 *(Contd.)*

Application	Platform	Features	Mechanisms	Ref.
		• **Selectivity**: K^+, Ca^{2+}, Mg^{2+}, Al^{3+}, Zn^{2+}, Fe^{3+}, Cr^{3+}, CO_3^{2-}, SO_4^{2-}, SO_3^{2-}, PO_4^{3-}, NH^{4+}, Fe^{2+}, Pb^{2+} and Cu^{2+} • **Sensitivity in real conditions**: tap water, river water		
		• **Target**: Ag^+ • **LOD**: 0.10 μM • **Linear range**: 0.5–150 μM • **Selectivity**: K^+, Ca^{2+}, Mg^{2+}, Al^{3+}, Zn^{2+}, Fe^{3+}, Cr^{3+}, CO_3^{2-}, SO_4^{2-}, SO_3^{2-}, PO_4^{3-}, $S_2O_3^{2-}$, NH^{4+}, Pb^{2+}, and Cu^{2+} • **Sensitivity in real conditions**: tap water, river water		
Ions sensing	Ti_3C_2 MQDs	• **Target**: Cr^{3+} • **LOD**: 30 mM • **Selectivity**: Cu^{2+}, Na^+, Ca^{2+}, Fe^{3+}	Sensing: FL	5
Ions sensing	N, P-doped Ti_3C_2 MQDs	• **Target**: NO_2^- • **LOD**: FL intensity ratio: 0.25 μM absorbance ratio: 0.71 μM • **Linear range**: FL intensity ratio: 1.5–80 μM, absorbance ratio: 4–85 μM • **Selectivity**: anions (F^-, Cl^-, Br^-, I^-, NO_3^-, CO_3^{2-}, SO_3^{2-}, SO_4^{2-}, PO_4^{3-}, HPO_4^{2-}), cations (Ca^{2+}, Mg^{2+}, Fe^{3+}, K^+, Zn^{2+}, Ba^{2+}) and coexisting substances (Arg, Try, Gly, Lys, Asp, Ser, His, Cys, Ala) • **Sensitivity in real conditions**: six types of sausage samples	Sensing: colorimetry (absorption) fluorometric dual-modal Quenching: IFE	84
Ions sensing	Fe_3O_4/Ti_3C_2 MQDs	• **Target**: Cr(VI) • **LOD**: 0.26 μM • **Linear range**: 0–60 μM • **Selectivity**: Na^+, Ni^{2+}, K^+, Ca^{2+}, Mg^{2+}, Co^{2+}, Cu^{2+}, Mn^{2+}, Al^{3+}, Fe^{3+}, Pb^{2+} and Cr^{3+} • **Sensitivity in real conditions**: tap water samples	Sensing: colorimetry	122
pH sensing	Ti_3C_2 MQDs	• **Target**: intracellular pH • **Linear range**: 6–8/5–9	Sensing: ratiometric fluorescence	43
Physical parameters sensing	MQD within natural 3D watermelon peel matrix	• **Target**: pressure sensor • **Sensitivity**: 323 kPa^{-1} for 0–0.4 kPa and 51.38 kPa^{-1} for 0.4–20 kPa	—	38
Others sensing	$Ti_3C_2T_x$ MQD thin film on quartz bulk acoustic wave	• **Target**: infrared radiation	Sensing: electromechanical (admittance and frequency shift of the sensor throughout infrared radiation absorption)	106
Ions sensing	Ti_3C_2 MQDs	• **Target**: Ag^+ • **LOD**: 0.45 μM • **Linear range**: 0.5–40 μM • **Selectivity**: Na^+, Au^{3+}, Mg^{2+}, Ca^{2+}, Zn^{2+}, Cu^{2+}, Ce^{3+}, Mn^{2+}, Cd^{2+}, Ni^{2+}, Al^{3+}, Fe^{3+}, Cr^{3+}, and Hg^{2+} • **Sensitivity in real conditions**: tap and river water samples	Sensing: FL	123
Others sensing	Ti_3C_2 MQDs–EDTA–Eu^{3+}	• **Target**: 2,6-dipicolinic acid (DPA) • **LOD**: 0.26 nM • **Linear range**: 0–11 μM • **Selectivity**: BA, PH, PA, NA, ISA, Cys, Leu, Arg, UA, Phe • **Sensitivity in real conditions**: river water samples	Sensing: colorimetry (absorption) fluorometric dual-modal Quenching: absorbance energy-transfer effect	124
Environmental pollutants sensing	Cu@Ti_3C_2 MQDs-aerogel	• **Target**: pirimiphos-methyl • **LOD**: 0.65 nM	Sensing: colorimetry (absorption)	125

Table 3 *(Contd.)*

Application	Platform	Features	Mechanisms	Ref.
		• **Linear range**: 100–3200 nM • **Sensitivity in real conditions**: seawater, tap water, pear juice, orange juice, milk, tomato juice and corn juice		
Others sensing	N-doped Ti_3C_2 MQDs	• **Target**: quercetin (QC) • **LOD**: 1.35 nM • **Linear range**: 25–600 nM • **Selectivity**: rutin, gallic acid, chrysin, morin, kaempferol, phloroglucinol, myricetin, galangin, dopamine, uric acid, serotonin, cysteine, methionine, glutathione, resorcinol, catechol, hydroquinone, lysine, Na^+, Cu^{2+}, Mg^{2+}, K^+ • **Sensitivity in real conditions**: onions, oranges, and red wine	Sensing: FL Quenching: static quenching/ radiation-free complex formation and IFE	126
WLED	S-doped, N-doped, and S–N-doped Ti_3C_2 MQDs	• CIE coordinates of (0.31, 0.35) • High stability under UV irradiation for a month	Yellow, blue, and orange emissions to make white LED	9
Single-component WLED	PDMS + Ti_3C_2 MQDs nanocomposite	• Tuning the white emission temperature from cool to warm • Piezochromic effect	Strong two-photon white fluorescence, originating from both carbon core and OLA-passivated surface states.	127
White laser	V_2C MQDs	• Enhancement in the PL intensity, covering the entire visible range	—	128
Solar cell	$Ti_3C_2Cl_x$ MQDs modified-perovskite	• PCE: 21.31% • Increase in J_{sc} and V_{oc} • Decrease in normal hysteresis • Maintaining over 84% of PCE after 1000 h	(1) Interaction between the Cl^- and Pb^{2+} ions induce the preferred grain orientation with smaller residual tensile strain. (2) $Ti_3C_2Cl_x$ QDs near the bottom substrate improve the perovskite film crystallinity.	129
Solar cell	Modified perovskite and TiO_2 with Ti_3C_2 MQDs and nanosheets.	• PCE improvement from 12.0% to 17.1% • Reduced hysteresis effect	(1) Positive effect of nanosheets on electron mobility improvement of TiO_2 (2) Reduced defects concentration *via* perovskite film passivation and increased perovskite crystallinity	34
Solar cell	Introduction of Nb_2C MQDs into SnO_2	• PCE improvement by 3%, reaching high value of 22.86% • Maintaining 98% of PCE after 40 days	(1) Grains enlargement (2) Modifying the roughness and surface energy (3) Lowering defects content (4) Enhanced perovskite crystallinity and effective carrier transport	130
Solar cell	$Ti_3C_2T_x$ MQDs-modified SnO_2	• Enhanced absorption in visible range • PCE: 23.3% • Outstanding stability against humidity and light soaking	Improving the crystal quality and phase stability of the perovskite	131
Solar cell	Nb_2O_5 and Ti_3C_2 MQDs into the TiO_2	• Increase in both photocurrent and efficiency (7.24%) • Higher and wider absorption range for photoanodes in the visible region and better charge transfer	(1) Tuning the energy level alignment of the photoanode through the introduction of Nb_2O_5 and Ti_3C_2 QDs into the TiO_2 photoanode (2) Suppressing electron–hole recombination at the photoanode interface	132

Table 3 *(Contd.)*

Application	Platform	Features	Mechanisms	Ref.
UV detector	$Ti_3C_2T_x$ MQDs into perovskite	• UV detector −1100% increase in spectral responsivity (264 A W^{-1} at 310 nm)	Enhancement of charge carriers and light absorption	8
Ultrafast photonics	Ytterbium-doped fiber laser/ $Ti_3C_2T_x$ MQDs	• Broadband saturable absorption from 540 to 1550 nm • Stable 357 ps mode • Locked pulses centered at 1069.17 nm under a low threshold power of 54 mW	Switching the polarization state in the cavity resulted in tunable mode-locked optical spectra	77
Ultrafast photonics	The photodeposition method to transfer $Ti_3C_2T_x$ MQDs to the tapered area to fabricate the SA	• Ultrafast photonics – tapered fiber saturable absorber (SA) device for an Er^{3+}-doped fiber laser (EDFL) • Low saturation intensity (1.983 GW cm^{-2}) and high modulation depth (11.6%) • Ultrashort pulses of 466 fs at a wavelength of 1566.57 nm with a fundamental frequency of 22.78 MHz	—	46
Nonvolatile memory device	PVP + MQDs nanocomposite	• Stable operation during a retention test (1.2×10^4 s), with an on/off current ratio of up to 100	(1) MQD charge trapping, originated from quantum confinement and the dissolvability of memristive components (2) Tuning the electrical conductance of an ITO/MQD-PVP/Au structure from insulator behavior to irreversible resistive switching, reversible resistive switching, and conductor behavior	133
Li–O_2 battery	Ti_3C_2 MQDs/N-doped carbon nanosheets (E'lyte: 1 M LiTFSI/TEGDME)	• Discharge capacity: 16 000 mAh g^{-1} • Cycling stability: 240 cycles at 200 mA g^{-1} • Voltage gap: 0.62 V (O_2 consumption/evolution overpotential) • Coulombic efficiency: 93.8%	Enhanced electrocatalytic activity, through adsorption of Li^+ to C side of the edge-rich of MQDs, and charge accumulation for Li_2O_2 production on cathode	134
Zn–air battery	Ti_3C_2 MQDs/Ni, Fe-layered dihydrate (Ni, Fe-LDH)/NG (E'lyte: 0.1 M KOH)	• Higher OER activity than pristine LDH/NG • Faster OER kinetics with smaller Tafel slope of 57 mV dec^{-1} compared to 120 mV dec^{-1} for Pt/C • 98.8% current retention after 10 h of operation, exceeding 84.3% for the commercial Pt/C	Improved electrical conductivity associated with MQDs (metallic behavior), and provided a higher carrier density compared to LDH sample	135
Li–S battery	g-C_3N_4@MQDs (E'lyte: 1 M LiTFSI@DME : DOL v/v 1 : 1 + 2 wt% $LiNO_3$)	• Confinement of polysulfide shuttle • Capacity = 1433 mA h g^{-1} at 0.1C • Capacity decay of 0.024% per cycle after 1000 cycles at 2C • Retention rate of nearly 70%, higher than Li–S batteries with GC separator (58%)	Improved capture–confinement–conversion through electrostatic adsorption of protonated g-C_3N_4 and MQDs to improve capturability of polysulfides	136
Supercapacitor	Integrated $Ti_3C_2T_x$ MQDs onto MXene nanosheets (PVA/H_2SO_4 gel electrolyte)	• Areal capacitance: 2202 mF cm^{-2} at 3 mA cm^{-2} • Areal energy density: 90.33 μWh cm^{-2} at 450 mW cm^{-2}	(1) Heterodimensional structure: 0D TCQDs + 2D TCNs → improved electron transport & ion accessibility (2) Strong interface interactions: polar functional groups enhance structural integrity & stability	137

Table 3 *(Contd.)*

Application	Platform	Features	Mechanisms	Ref.
Supercapacitor	MQD-$Ni(OH)_2$ composite (1 M KOH)	• Capacitance retention: 84% after 10 000 charge–discharge cycles • Specific capacitance: 1660 F g^{-1} at 1 A g^{-1} • 98 F g^{-1} for asymmetric supercapacitor • Energy density: 30.6 Wh kg^{-1} (at 750 W kg^{-1} power density) • Capacitance retention: 84% after 10 000 cycles • R_{ct}: 6.7 Ω (lower than $Ni(OH)_2$-only)	(1) Quantum confinement of QDs → enhanced conductivity → faster electron transport, and boosted electrochemical reactivity (2) Thin $Ni(OH)_2$ nanosheets → increased active sites	138
Supercapacitor	MQDs/Laser Reduced Graphene Oxide (LRGO) (PVA/H_2SO_4 gel electrolyte)	• Areal capacitance: 10.42 mF cm^{-2} (91% transmittance) • 64.6 mF cm^{-2} (53% transmittance) • Energy density: 2.04 × 10^{-3} mWh cm^{-2} • Power density: 129.4 μWh cm^{-2} • Cycle life: 97.6% retention after 12 000 cycles • Transparency: over 90% • Conductivity: 760.4 S m^{-1}	Enhanced surface area & edge states → improved charge storage synergistic MQD/LRGO interface → higher electron/ion transport	12
Supercapacitor	Ti_3C_2 MQDs/large $Ti_3C_2T_x$ (L-$Ti_3C_2T_x$) fiber (PVA/H_2SO_4 gel electrolyte)	• Electrode capacitance: 1560 F cm^{-3} at 1 A cm^{-3} • Capacity retention: 79% at 20 A cm^{-3} • Mechanical strength: 130 MPa • Supercapacitor capacitance: 413 F cm^{-3} at 0.5 A cm^{-3} • Cycle stability: 97% retention after 10 000 cycles • Energy density: 36.7 mWh cm^{-3} at 311 mW cm^{-3} • Temperature range: −40 to 60 °C	(1) Large L-$Ti_3C_2T_x$ NSs → improved mechanical strength (2) Synergistic interaction of $Ti_3C_2T_x$ QDs & L-$Ti_3C_2T_x$ → higher efficiency	139
Photocatalytic HER	Ti_3C_2 MQDs/g-C_3N_4 (0.5 M Na_2SO_4)	• Co-catalysts for photocatalytic H_2 evolution	Increased H_2 reduction rate due to high aqueous solubility of MQDs and more abundant active edge sites	140
Photocatalytic HER	N-doped Ti_3C_2/1D-CdS (0.1 M Na_2SO_4)	• HER rate: 17 094 μmol g^{-1} h^{-1} (14.79× higher than pure CdS) • R_{ct}: 3.57 Ω (significantly reduced) • Electron lifetime: 6.65× longer than pure CdS • Photostability: no significant loss after 4 cycles	Facilitated separation and charge carriers transfer from photoexcitation of CdS QDs, and supply Lewis acid sites for adsorption of 1,2-BM to accelerate H_2 evolution	138
Photocatalytic HER	MQDs/$Co_2(OH)_3Cl$/CF (0.1 M KOH)	• Overpotential: 91 mV@10 mA cm^{-2} • Tafel slope: 67 mV dec^{-1} • Low charge transfer resistance (R_{ct}): 4.514 Ω • Electrochemical Surface Area (ECSA): 240 cm^{-2} • Stability: 82.6% retention after 30 h	(1) Interface charge transfer: induces $Co^{2+\delta}$ high-valence sites for better H_2O activation (2) Lattice strain effect: improves structural integrity (3) Lowering the kinetic barrier for H_2O dissociation (Volmer step): tuning the H* adsorption Gibbs free energy toward the thermoneutral ideal.	141

Table 3 *(Contd.)*

Application	Platform	Features	Mechanisms	Ref.
Photocatalytic HER	Ti_3C_2 MQDs modified 3D/2D TiO_2/g-C_3N_4 (0.1 M Na_2SO_4)	• Hydrogen production rate of 5540.2 μmol g^{-1} h^{-1}, 1.6 times higher than that of TiO_2/g-C_3N_4 and 33 times higher than that of pure g-C_3N_4	(1) Promoting strong interaction between cocatalysts due to MQDs' functional groups (2) Stronger performance due to reducing electron–hole recombination (3) Accelerating electron migration from the conduction band of g-C_3N_4	142
Nitrogen Reduction Reaction (NRR)	Ti_3C_2 MQDs/2D Ni-MOF (0.5 M Na_2SO_4)	• Ammonia yield: 88.79 μmol g^{-1} h^{-1} (4× higher than pristine Ni-MOF) • Band gap: 3.6 eV (Ni-MOF), 4.92 eV (Ti_3C_2-QD)	(1) MQD excitation → electrons transfer to Ni-MOF (2) Ni sites act as active centers → adsorption & activation of N_2 MQDs with abundant active sites enable efficient NRR	138
NRR	Ti_3C_2 MQDs decorated on the 2D Ni-MOF (3 M KOH)	• Photo-reduction N_2 activity of 88.79 μmol g^{-1} h^{-1}, which was 4 times higher than that of the pristine 2D Ni-MOF	(1) Interfacial area of the Ti_3C_2 MQD/Ni-MOF composite to facilitate the photocarrier's direction migration (2) Reducing the free-energy corresponding N–N bond and length of the N_2 fixation pathways	4
NORR	Ti_3C_2 MQDs/Cu NWs (0.1 M K_2SO_4)	• Electrochemical reduction of NO into NH_3 high NH_3 yield of 5346.3 μg h^{-1} mg^{-1} • Faradaic efficiency of 95.5% in 0.1 M K_2SO_4 solution at a much lower potential of −0.4 V *vs.* RHE • Zn–NO battery with Ti_3C_2 QDs/Cu NWs as the cathode showed power density of 3.03 mW cm^{-2} and an NH_3 yield of 925.2 μg h^{-1} mg^{-1}	NO into NH_3 reaction pathway (*NO → *HNO → *N → *NH → *NH_2 → *NH_3) and potential determination step (*N → *NH) for the NORR on Ti_3C_2 QDs/Cu NWs	143
NO_x oxidation	$Ti_3C_2T_x$ MQDs/g-C_3N_4/bismuth oxyiodide (BiOI) (0.2 M Na_2SO_4)	• NO removal rate: 42.23% (highest among tested catalysts) • NO_2 production: 31.52 ppb (lowest among tested catalysts) • NO_2 selectivity: 0.17 (indicates efficient NO oxidation) • Stability: 5-cycle test shows minimal degradation	p–n heterojunction led to enhanced charge separation and transfer, as well as promoting gas absorption and activization, further achieving an excellent photocatalytic performance.	138
CO_2 photoreduction	$Ti_3C_2T_x$ MQDs/g-C_3N_4/BiOI 0.5 M Na_2SO_4	• CO production rate: 57.8 μmol g^{-1} h^{-1} (highest among tested catalysts) • CH_4 production rate: 3.6 μmol g^{-1} h^{-1} • Adsorption capacity: 4.53 cm^3 g^{-1} for CO_2 • CN/MQDs/BOI showed CO production rate of 57.8 μmol g^{-1} h^{-1} and CH_4 production rate of 3.6 μmol g^{-1} h^{-1}	Electron-withdrawing ability of MQDs, further promotes the generation of more active species involved in reactions	144
CO_2RR	Ti_3C_2 MQDs decorated Cu_2O NWs on Cu mesh (0.5 M Na_2SO_4)	• Methanol production	(1) Improved the stability of Cu_2O NWs, enhanced charge transfer, carrier density, light adsorption, and decreasing band bending edge and charge recombination	145

Table 3 *(Contd.)*

Application	Platform	Features	Mechanisms	Ref.
		• Photocatalytic reduction of CO_2 by Ti_3C_2 QDs/Cu_2O NWs/Cu is 8.25 times and 2.15 times of that from Cu_2O NWs/Cu and Ti_3C_2 sheets/Cu_2O NWs/Cu	(2) Ti_3C_2 QDs favorably chemisorbed CO_2 instead of H_2O and further facilitated CO_2 reduction by promoting H^+ attachment and donating electrons	
Photocatalysis	Ti_3C_2 MQDs/Cu_2O NWs/Cu (0.5 M Na_2SO_4)	• Photoelectrochemical CO_2 reduction	Light absorption improvement, facilitated charge separation, and transport	146
H_2O_2 production	Nb_2C MQDs@PY-DHBD-COF (pyrene-based)	• Achieved a H_2O_2 yield record of 3560 μmol g^{-1} h^{-1}, and AQY of 12.8% at 400 nm together with SCC efficiency of 0.27%	• Adsorption of O_2 on the MQDs to form $*O_2$ • Transfer of e^- to the $*O_2$ to be reduced to *OOH • Combination of H^+ with *OOH to form *HOOH • Hydrogenation of *HOOH to form H_2O_2	147
Nucleus-target low-temperature photothermal therapy	V_2C MQDs modified with the cell nucleus-target TAT peptides and cell target Arg-Gly-Asp	• Tumor clearance at low temperature • Without side effects non-toxic	Processed proteins facilitated drug nuclear-targeting of cancer cells. Under NIR-II laser irradiation, V_2C-PEG-TAT's temperature raised, leading to genetic material damage.	148
Antitumor activity *in vivo*	Non-oxidizing N-MQDs-$Ti_3C_2T_x$	• Tumor inhibition rate of 91.9% • No significant toxicity during the therapeutic treatment • Excreted by the kidneys of animals 48 h after administration	(1) By intratumorally MQDs administering in HeLa tumor xenografts, the Ti^{3+} bonded to cancer cells in H_2O_2, catalyzing its production of highly toxic species led to cancer cell death. (2) Tumor microvascular permeability caused hemorrhage.	92
Photothermal cancer therapy	Fluorine-free Ti_3C_2 MQDs	• Photothermal conversion efficiency of 52.2% • Extinction coefficient of 52.8 L g^{-1} cm^{-1} • High photostability • No biotoxicity at a concentration of 100 PTT (*in vitro*) on HeLa, MCF-7, U251, and HEK 293 cells. • No toxic effects and side effects of the QDs on mouse cells	$Al(OH)_4$ on the surface of MQDs caused strong absorption in the NIR region. Irradiation of 808 nm with a power of 0.5 W cm^{-2} led to a tumor destruction rate of 100% with no significant change in the bodyweight of mice.	149
PA imaging guided photothermal therapy	Ti_2N MQDs	• Applicable in NIR-I and NIR-II region • High absorption • High photothermal conversion efficiency • Photothermal stability	Mice injected with Ti_2N QDs. After, 10 min laser irradiation at 1.0 W cm^{-2} power density in NIR-I and NIR-II, the temperature increased from 37 °C to more than 60 °C and 69 °C.	148
PA/photothermal imaging-guided PTT/ intracellular microRNA imaging	Mo_2C MQDs	• Photothermal conversion efficiency of 42.9% at low concentration (100 μg mL^{-1}) • Biocompatibility • Photothermal stability • Efficient tumor accumulation through EPR	After intravenous administration of Mo_2C QDs in mouse bearing B16-10F tumor, an 808 nm laser (0.64 W cm^{-2}, 10 min) irradiated. This increased the tumor temperatures from 27.9 °C to 63 °C.	92

Table 3 *(Contd.)*

Application	Platform	Features	Mechanisms	Ref.
		• Providing photoacoustic imaging signal		
Photothermal immunoassay/protein point-of-care (POC) testing and diagnostics	Ti_3C_2 MQDs-encapsulated liposomes	• High photothermal efficiency • Ability to detect infinitesimal concentrations of prostate-specific antigen	PSA detected at 808 nm with 1.5 W cm^{-2}. NIR laser energy was converted into heat using Ti_3C_2 QDs and the temperature shift was assessed.	149
Multicolor cellular imaging	Different morphologies of Ti_3C_2 MQDs with RAW264.7 cells	• Strong photoluminescence • High biocompatibility • Multicolor excitations at 405, 488, and 543 nm • Penetrate easily into the cell without damaging the nucleus	Within 4 h incubation, the MQDs were incorporated into the cells by endocytosis. Then the images were taken with confocal fluorescence microscopy.	82
Imaging and biolabeling abilities	Ratiometric fluorescent pH sensors based on Ti_3C_2 MQDs	• Excellent performance for living cells	Images taken with confocal fluorescence microscopy of MCF-7 cells after endocytosis of Ti_3C_2 QDs. As pH decreases from 8 to 6, fluorescence from the Ti_3C_2 QDs increases.	150
Fluorescence probes applicable for the cellular study	Nb_2C MQDs	• Highly chemically stable • Biocompatible • Photobleach resistant • Selectively stained the cytoplasm of the cells	MQDs were cocultured with cells for 4 h. The cytoplasm of the cells was selectively stained.	82
Cell imaging/detecting Cu^{2+} ions/diagnosis of cytophagy-related diseases	N, P-MQDs	• The tests are performed at nontoxic concentrations • Photoluminescence quantum yield (PLQY) of 20.01% (by doping) • Constant fluorescence intensity in a wide pH and temperature range • Good stability and stable expression in complex organisms	The N, P-MQDs were taken up by the THP-1 macrophages in 24 h and emitted green colors when exposed to 488 nm light source.	151

MXene quantum dots (MQDs), electrochemiluminescence (ECL), fluorescence (IFE), photoelectrochemical (PEC), ascorbic acid (AA), glucose (GLU), uric acid (UA), diaminopyridine (DAP), photoinduced electron transfer (PET), limit of detection (LOD), dopamine (DA), glucose oxidase (GOD), alkaline phosphatase (ALP), transferrin (Trf), lysozyme (Lyz), ovalbumin (Ova), chymotrypsin (Chy), immunoglobulin G (IgG), colony-forming unit (Cfu), kanamycin (KAN), cefixime (CFX), chloramphenicol (CHL), norfloxacin (NOR), oxytetracycline (OTC), doxorubicin (DOX), aspartic acid (Asp), serine (Ser), lysine (Lys), glycine (Gly), glutathione (GSH), nitrobenzoic acid (NBA), benzoic acid (BA), benzidine (BD), nitrobenzene (NB), 2,4-dinitrophenylhydrazine (DNPH), *p*-nitrophenyl phosphate (PNPP), tryptophan (Try), cysteine (Cys), Förster resonance energy transfer (FRET), electron spin resonance (ESR), hydrogen evolution reaction (HER), nitrate oxidation reduction reaction (NORR), nitrogen reduction reaction (NRR), covalent organic framework based on pyridine and dihydroxybenzidine (PY-DHBD-COF).

ions with the amino groups.[64] The lowest reported LOD for Fe^{3+} detection (1.25 nM) was attained when BSA@Ti_3C_2 MQDs were used.[70,121] The detection mechanism involved electron and energy transfer processes where the metal ions facilitated electron–hole recombination annihilation and altered the electronic state of the MQDs (Fig. 9b).

Cobalt and silver ions are of particular concern due to their environmental risks[153] and potential to cause cellular diseases,[2] making their sensitive and simultaneous detection highly significant. Cr^{3+} plays an essential role in biological processes and metabolism; however, elevated concentrations of Cr^{3+} can adversely affect cellular structure scan.[2] N-Ti_3C_2 MQDs enabled real-time and simultaneous detection of Co^{2+} and Ag^{+} with a LOD of 0.21 μM and 0.10 μM, respectively.[2] The primary detection mechanism was attributed to a combination of the IFE and the static quenching effect, resulting from the overlap between the absorption spectra of Co^{2+}/Ag^{+} ions and the emission and excitation spectra of the N-Ti_3C_2 QDs.[2] In another study, by taking advantage of Ti_3C_2 MQDs, Cr^{3+} was detected with a low limit of detection of 30 mM with high selectivity in the presence of interfering ions.[5] Although all Cr^{3+}, Fe^{2+}, Co^{3+}, and Cu^{2+} quenched the emission of QDs, the

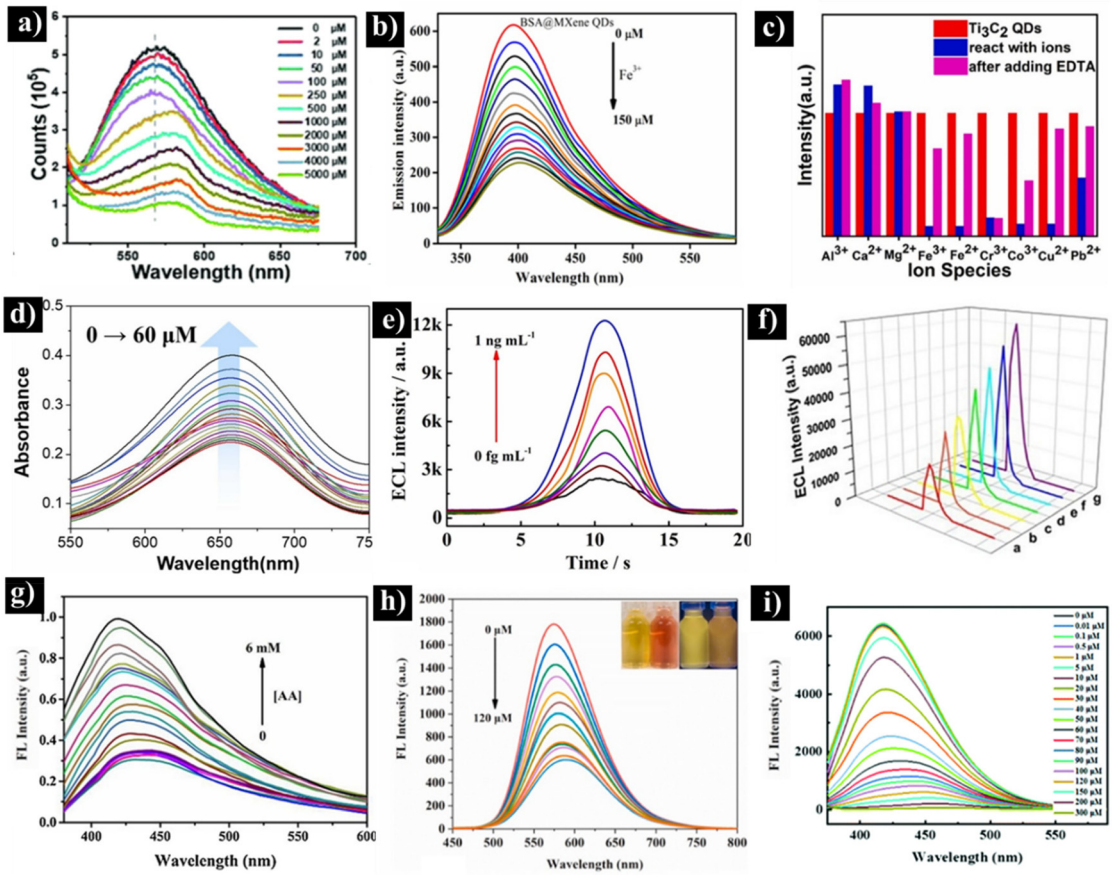

Fig. 9 (a) PL emission spectra of Cu^{2+}-(N, P-MQD) depending on the Cu^{2+} concentration (reprinted with permission from The Royal Society of Chemistry, copyright © 2019).[102] (b) Fluorescence-based detection of Fe^{3+} ions by BSA@MQDs (reprinted with permission from Wiley, copyright © 2022).[39] (c) Fluorescence quenching and recovery of Ti_3C_2 MQDs by metal ions and EDTA addition, respectively (reprinted with permission from Elsevier, copyright © 2022).[5] (d) UV-Vis spectra of Fe_3O_4@Ti_3C_2 MQDs depending on the Cr(VI) concentration (reprinted with permission from Elsevier, copyright © 2023).[122] (e) ECL curves of MUC1 immunosensor (reprinted with permission from Elsevier, copyright © 2022).[101] (f) ECL detection of miRNA-26a with various concentrations by Ti_3C_2 MQD@Au nanobones (reprinted with permission from the American Chemical Society, copyright © 2021).[72] (g) Changes in the fluorescence spectra of N-Ti_3C_2 MQDs with increasing AA concentrations (reprinted with permission from Elsevier, copyright © 2021).[107] (h) Variations in the fluorescence spectra of N-MQDs with ARS concentrations. The inset shows the colloidal samples under daylight (left) and 365 nm UV (right) (reprinted with permission from Elsevier, copyright © 2021) images.[100] (i) The florescence spectra of UA@Ti_3C_2 MQDs fluorescence depending on the TNP concentrations (reprinted with permission from The Royal Society of Chemistry, copyright © 2020).[88]

addition of ethylenediaminetetraacetic acid recovered the PL response for all interfering elements except Cr^{3+}, indicating selective detection of the target ion (Fig. 9c).[5] Another recent progress is colorimetric detection of Cr(VI) ions by Fe_3O_4@Ti_3C_2 MQDs since an exceeding concentration of Cr(VI) in drinking water causes various diseases.[122] This colorimetric method includes a catalytic oxidation of 3,3′,5,5′-tetramethylbenzidine (TMB) by Fe_3O_4@Ti_3C_2 MQDs in the presence of H_2O_2, resulting in the formation of a blue-colored product. Then, introducing 8-Hydroxyquinoline (8-HQ) reduces the blue color intensity of oxidized TMB. Introducing Cr(VI) with various concentrations up to 60 μM leads to a linear increase in the absorbance and recovery of the blue color (Fig. 9d), allowing sensitive and selective detection of Cr(VI) with a LOD of 0.26 μM.[122] Ti_3C_2 MQDs have also been utilized for the detection of manganese (Mn(VII)) with a low LOD of 5.2 nM, which is superior to carbon dots with a LOD of 230 nM. This exceptional sensitivity was associated to the inherent reducibility of the MQDs, which facilitated a redox reaction with Mn(VII), resulting in pronounced fluorescence quenching. In contrast, the fluorescence quenching mechanism in carbon dots involved a synergistic IFE and static quenching due to the overlap between the absorption peaks of Mn(VII) and the excitation/emission spectra of the CDs. Further studies underscored the potential of these MQDs to serve as a dual-functional platform for simultaneous detection and scavenging of Mn(VII) in plant leaves, showcasing their impeding application in environmental safety and biological monitoring.[154]

5.1.2. Detection of amino acids and proteins. MQDs have been utilized to detect various amino acids and proteins.[114]

Histidine, a fundamental amino acid for human tissue growth and repair, was detected with the LOD of 2.1 nM using the nonfluorescent complex of Ni^{2+}-Ti_3C_2 MQDs *via* the IFE mechanism. Due to its strong affinity for Ni^{2+} ions, histidine competes with Ti_3C_2 MQDs for binding, thereby reversing fluorescence quenching. The sensor demonstrated high accuracy in detecting histidine in human samples, with a recovery rate ranging from 6.75% to 103.24%.[114] Another example is the application of Ti_3C_2 MQDs for the detection of cytochrome (cyt-c) and trypsin.[110] Introducing cyt-c to fluorescent Ti_3C_2 MQDs quenches the emission due to electron transfer from the QDs to the analyte. The degree of fluorescence quenching provides a quantitative measure of cyt-c concentration. Upon adding trypsin, the fluorescence is restored as trypsin hydrolyzes cyt-c into smaller peptides and removes them from the Ti_3C_2 QDs solution.[110]

Researchers have developed a novel MXene-based biosensor for detecting polynucleotide kinase (PNK).[71] This enzyme plays a crucial role in phosphorylation-related DNA repair and nucleic acid metabolism. This biosensor, which operates *via* an ECL mechanism (eqn (1)–(5)) utilizes a hybrid Ti_3C_2 MQD/Au NPs in the presence of a co-reactant ($K_2S_2O_8$). The hybrid NPs offer significant advantages over Ti_3C_2 MQDs, including a threefold enhancement in the ECL signal due to surface plasmon resonance (SPR), superior electrocatalytic performance, and charge transfer capabilities. PNK interacts with the DNA probe immobilized on the modified electrode surface, triggering a series of reactions that amplify the ECL signal. Under optimal conditions, a linear relationship between ECL intensity and PNK concentration is attained, making this biosensor a powerful tool for PNK analysis in comparison to other sensors.[71]

$$S_2O_8^{2-} + e^- \rightarrow SO_4^{2-} + SO_4^{\bullet -} \quad (1)$$

$$Ti_3C_2\ QDs\text{-}AuNPs + SO_4^{\bullet -} \rightarrow Ti_3C_2\ QDs^{\bullet +}\text{-}AuNPs + SO_4^{2-} \quad (2)$$

$$Ti_3C_2\ QDs\text{–}AuNPs + e^- \rightarrow Ti_3C_2\ QDs^{\bullet -}\text{–}AuNPs \quad (3)$$

$$Ti_3C_2\ QDs^{\bullet +}\text{–}AuNPs + Ti_3C_2\ QDs^{\bullet -}\text{–}AuNPs \rightarrow Ti_3C_2\ QDs^{*}\text{–}AuNPs \quad (4)$$

$$Ti_3C_2\ QDs^{*}\text{–}AuNPs \rightarrow Ti_3C_2\ QDs\text{–}AuNPs + h\nu \quad (5)$$

Jiang *et al.*[101] detected Mucin 1 (MUC1), a key molecule involved in cell signal transduction,[155] by an ECL biosensor based on N-Ti_3C_2 MQDs.[101] The MQDs exhibited fluorescence and ECL emissions at 455 nm and 612 nm, respectively. To fabricate the biosensor, Au NPs were electrodeposited onto a glassy carbon electrode (GCE) and functionalized with anti-MUC1 antibodies, followed by BSA treatment to prevent nonspecific binding. Next, the MUC1 antigen was introduced to this surface. The biosensor platform was then promoted with adding an AgPt@N-Ti_3C_2 QDs-anti-MUC1-BSA bioconjugate to enhance ECL sensitivity. The AgPt@N-Ti_3C_2 QDs nanocomposites played a crucial role in developing the ECL immunosensor for MUC1 detection through interacting with the co-reactant $S_2O_8^{2-}$ in phosphate-buffered saline (PBS). As the concentration of MUC1 increased from 1 fg mL^{-1} to 1 ng mL^{-1}, the ECL signal was linearly enhanced, providing a low LOD of 0.31 fg mL^{-1} (Fig. 9e).[101]

5.1.3. miRNAs detection. Identifying specific organic molecules as biological indicators is crucial for diagnosing health problems in the early stages. For instance, triple-negative breast cancers are diagnosed by miRNA-26a identification, which plays a critical role in preventing cell proliferation, invasion, and migration in breast cancer cells.[72] Recently, MQDs have engaged considerable attention to be used for miRNAs detection. By taking advantage of Ti_3C_2 MQD@Au nanobones (NBs), miRNA-26a was detected up to a concentration of 10 nM with the a LOD of 1.7 fM (Fig. 9f).[72] The biosensor was also applied to detect clinical patient serum samples. The sensing mechanism involved a series of interactions that led to measurable changes in ECL. The heterostructure was modified with capture DNA that bound to miRNA-26a. Upon hybridization, T7 exonuclease cleaved the DNA-miRNA complex and released miRNA-26a, which served as an RNA walker, interacting with more capture DNA. Simultaneously, amino-functionalized MnO_2 nanosheets (MnO_2 NSs@probe DNA) were introduced to quench the ECL signal of MQD@Au NBs. As the miRNA-26a concentration increased, more capture DNA was cleaved, thereby reducing the interaction between the capture DNA and the probe DNA on the MnO_2 nanosheets that ultimately increased the ECL signal.[72] In another study, Ti_3C_2T MQDs were used to enable sensitive detection of microRNA-155, an important indicator of B-cell lymphoma and breast cancer diseases.[71] To this end, a photoelectrochemical (PEC) platform, comprising TiO_2 nanosheets with exposed (001) facets, antibody, RNA–DNA, $Ti_3C_2T_x$ QDs, and (001) TiO_2/FTO, was fabricated. To achieve this, AuNPs were deposited on the electrode to immobilize thiol-modified DNA, which bound to microRNA-155 selectively. The electrode was then treated with 6-mercapto-1-hexanol (MCH) to block nonspecific sites and to enhance specificity. Afterwards, the hybridized microRNA–DNA structure was recognized by an antibody (S9.6 antibody), followed by the introduction of IgG-ALP, which generated an electron donor, increasing the photocurrent for quantitative analysis. The PEC platform demonstrated high sensitivity with a detection limit of 0.025 pM for microRNA-155.[71] The high surface energy of nanosheets as well as the $Ti_3C_2T_x$ QDs/TiO_2 type II heterostructure minimized electron transfer loss.

5.1.4. Sensing of organic acids. MQD-based sensors have frequently been utilized for detecting organic acids, such as ascorbic acid (AA), which is an essential antioxidant regulating internal redox homeostasis during various life processes.[107] The fluorescent N-Ti_3C_2 MQD nanoprobe has been effective in the determination of Cr(VI) and AA with a LOD of 0.02 μM and 0.012 μM, respectively.[107] In the absence of AA, the fluorescence of N-Ti_3C_2 MQDs is significantly impeded by Cr(VI) due to the IFE and static quenching. However, upon the addition of AA, the redox reaction between Cr(VI) and AA weakens the impact of the IFE, resulting in the restoration of the fluorescence signal of N-Ti_3C_2 MQDs (Fig. 9g). The nanoprobe demonstrates high sensitivity, selectivity, and reproduci-

bility for the detection of Cr(VI) and AA in real samples.[107] Ti_3C_2 MQDs also allow monitoring of uric acid (UA) with the a LOD of 125 nM.[105] UA is a key biomarker for various medical conditions, such as obesity, fatty liver, kidney stones, and diabetes.[105] To achieve this, *o*-phenylenediamine (OPD) is oxidized to produce yellow-colored 2,3-diaminophenazine (oxOPD) in the presence of horseradish peroxidase (HRP) and hydrogen peroxide. Using an overlap between fluorescence emission of glutathione (GSH)-functionalized Ti_3C_2 MQDs at 430 nm and the absorption of oxOPD at 425 nm, FRET is facilitated. As the concentration of UA increases, the GSH-Ti_3C_2 MQDs emission is gradually diminished, while the 568 nm emission from oxOPD increases progressively, enabling precise detection of UA.[105]

5.1.5. Environmental pollutants. Environmental pollutants pose serious risks to human and public health, thus requiring advanced detection methods.[111,156] MQDs-based platforms have manifested great potential for sensitive and efficient detection of different contaminants, including *Vibrio parahaemolyticus* (VP),[116] Alizarin Red (ARS),[100] 2,4,6-trinitrophenol (TNP),[88] pirimiphos-methyl,[125] and tetracycline (TC).[109]

To detect VP with a LOD of 30 cfu mL^{-1}, a composite probe comprised of modified polyhedral oligomeric silsesquioxane-perovskite quantum dots (POSS-PQDs) with aptamers (as the signal probe) and Ti_3C_2 MQDs (as the quencher) was used. The fluorescence emission of the probe was quenched through FRET in the absence of the VP. Introducing VP recovered the PL signal and amplified it in a concentration-dependent manner.[116]

ARS is a commonly used dyeing agent for textiles; however, its toxicity poses a significant risk to human health and ecological stability.[100] Recently, N-Ti_3C_2 MQDs were found effective in the successful detection of ARS, achieving a LOD of 1.21 μM in the linear range of <80 (Fig. 9h).[100] The quenching mechanism was identified as IFE due to three key observations. First, the absorption spectra of ARS overlapped with the excited emission spectra of N-Ti_3C_2 MQDs, thereby reducing the emission of N-Ti_3C_2 QDs. Second, the fluorescence lifetimes of N-Ti_3C_2 MQDs remained nearly unchanged before and after the addition of ARS, suggesting that the quenching is not due to static quenching but rather to IFE. Third, no new absorption peaks were observed in the absorption curves after adding ARS, indicating that there are no chemical interactions.[100]

TNP is a versatile chemical compound widely used in various industrial applications, including explosives, matches, dyes, and leather products.[88] TNP is highly toxic, and prolonged exposure can cause adverse symptoms such as headaches, dizziness, and nausea. Wang *et al.*[88] successfully detected TNP by UA-modified Ti_3C_2 (UA@Ti_3C_2 MQDs). A significant overlap was observed between the absorption spectrum of TNP and the emission spectrum of UA@Ti_3C_2 MQDs, suggesting the potential involvement of FRET or IFE. Further analysis using UV absorption and the average fluorescence lifetime of UA@Ti_3C_2 MQDs revealed that the quenching occurred *via* the IFE mechanism. The fluorescence intensity decreased with increasing TNP concentration, enabling the detection of TNP within a range of 0.01 to 300 μM, with a LOD of 9.58 nM (Fig. 9i). The detection limit was lower than the maximum residue limit of TNP in drinking water, as set by the US Environmental Protection Agency.[88] In another study, Ding *et al.*[125] used Cu@Ti_3C_2 MQDs-aerogel to detect pirimiphos-methyl, a kind of organophosphorus pesticides. The detection mechanism was based on the peroxidase-like activity of Cu@Ti_3C_2 MQDs-aerogel, which catalyzed the decomposition of hydrogen peroxide (H_2O_2) into reactive hydroxyl radicals ($^{\bullet}OH$). This process enabled an effective colorimetric assay by measuring the peak intensity at 652 nm, corresponding to the oxidation of TMB. As the concentration of pirimiphos-methyl increased, the catalytic activity decreased, allowing for its precise detection with a LOD of 0.65 nM.[125]

Tc is a versatile antibiotic in animal care, but its misuse poses health risks, including allergic reactions and ecological accumulation.[109] Therefore, there is an urgent need for efficient detection of Tc residues in food and water.[109] A ratiometric fluorescent sensor based on N, B co-doped Ti_3C_2 MQDs and Eu^{3+} was found effective in Tc detection with a LOD of 20 nM. When Tc was added to a N, B co-doped Ti_3C_2 MQDs solution, the emission intensity at 448 nm was slightly reduced due to the IFE mechanism. As the Tc concentration increased, the 448 nm emission peak was gradually weakened, while another peak that appeared at 616 nm appeared, underscoring the prominent effect of Eu^{3+} in Tc detection. The successful performance of Eu^{3+}/N, B-Ti_3C_2 MQDs in the detection of Tc in the milk samples demonstrated their strong potential for practical use.[109]

5.1.6. Other biological targets. GSH is a strong antioxidant that plays a crucial role in the detoxification, the metabolism of chemotherapeutic drugs, and the support of cellular functions.[115] It is well known that deviations in GSH levels cause severe cell apoptosis and cancer. Chen *et al.*[115] employed the PEC technique and a Ti_3C_2 MQD/TiO_2 heterojunction electrode to detect GSH with a LOD of 9 nM. The electrode was simultaneously biased at 0.1 V and excited by 150 W xenon light. The results revealed that the photocurrent of TiO_2/Ti_3C_2/Nafion electrode gradually increased with the addition GSH, enabling its detection at a low applied bias with strong surface adsorption.[115]

There is also an urgent need to advance sensitive and non-toxic detection methods for H_2O_2.[118] As an example of potential application, the tumor microenvironment in cancer cells often exhibits an overproduction of H_2O_2, leading to the formation of highly reactive and toxic hydroxyl radicals ($^{\bullet}OH$). These hydroxyl radicals, in turn, induce oxidative stress and damage to cancer cells, prompting processes such as apoptosis (programmed cell death) and inhibition of tumor growth.[92] Hence, detecting H_2O_2 levels accurately is critical for understanding its role in diseases and for the development of sensitive, non-toxic detection methods.[118] Recently, N-Ti_3C_2 MQDs were utilized for H_2O_2 sensing with a LOD of 1.2 nM which is the lowest reported value to date.[118] In another study, it was shown that Ti_3C_2 MQDs synthesized *via* the acoustic method exhibit more H_2O_2 sensing capability compared to those pre-

pared by the hydrothermal method.[97] The sensor platform was based on Ti_3C_2 MQDs/glassy carbon (Naf/MQD/GCE).[97] The square wave voltammetry revealed a LOD of 5 nM (Fig. 10a and b), with a higher linear regression slope of the current response plots.[97] H_2O_2 was also detected by N-$Ti_3C_2T_x$ MQDs *via* a colorimetric approach using TMB.[92] Here, the breakdown of the O–O bond in H_2O_2 into $^{\bullet}OH$, which oxidized TMB, resulting in two distinctive absorbances at 370 and 652 nm. This enabled the detection and quantification of hydroxyl radicals and H_2O_2.[92]

N-Ti_3C_2 MQDs functionalized with oxOPD (N-Ti_3C_2 QDs@DAP) have proven highly effective for detecting substances like xanthine, which generates H_2O_2 through specific enzymatic reactions.[92] The operation of this nanoprobe involves a multi-step enzymatic process. Xanthine is oxidized by xanthine oxidase (XOD) to produce H_2O_2, which subsequently reacts with OPD in the presence of HRP. This reaction results in the formation of DAP. The presence of DAP not only quenches the fluorescence of N-Ti_3C_2 MQDs but also provides a new emission peak at 560 nm, establishing a dual-emission sensor. Here, N-Ti_3C_2 MQDs serve as electron donors, while DAP acts as an electron acceptor. Consequently, a complex is formed on the functionalized surface of the QDs, quenching the fluorescence intensity. This dual-emission system provides a sensitive and reliable method for detecting xanthine and H_2O_2, showcasing the versatility and efficacy of N-MQDs@DAP in diagnostic applications.[92]

Ti_3C_2 MQDs have also been utilized for the ratiometric fluorescence detection of a *Bacillus anthracis* biomarker, 2,6-dipicolinic acid (DPA).[124] Ti_3C_2 MQDs are endowed with abundant hydroxyl and amino groups, which are utilized for coordination with EDTA and Eu^{3+} to form a composite probe, named Ti_3C_2 QDs–EDTA–Eu^{3+}. While Ti_3C_2 QDs emit stable blue color as a reference signal, the fluorescence of Eu^{3+} is quenched by

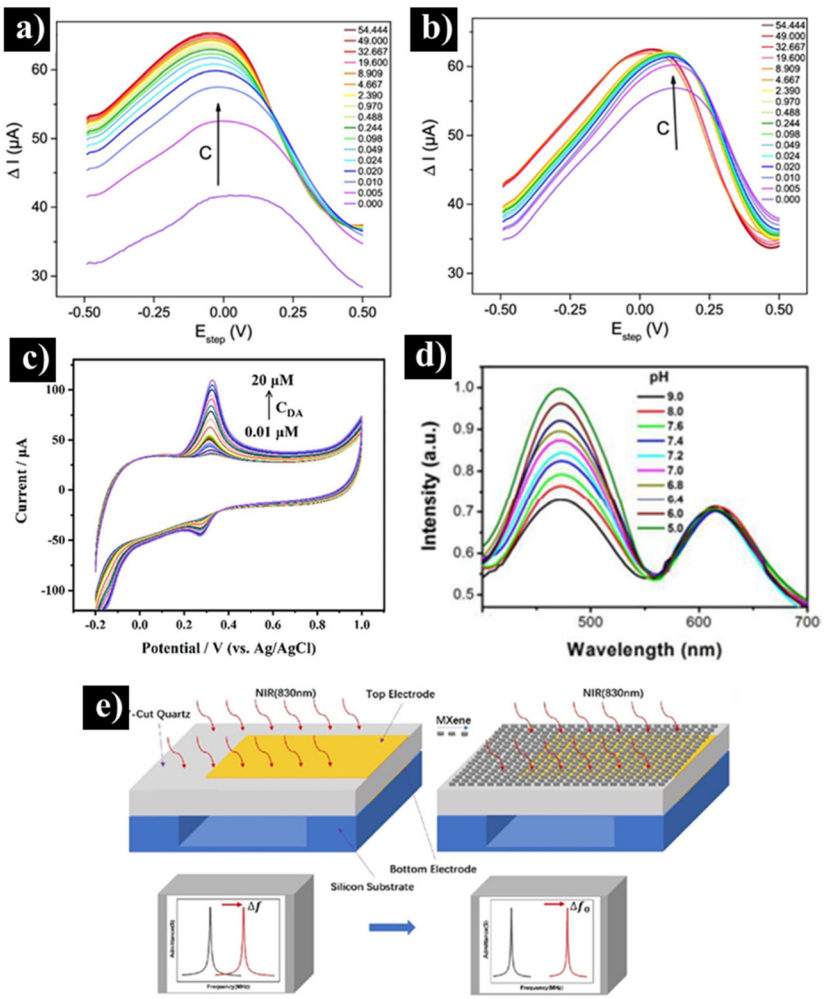

Fig. 10 (a and b) Square wave voltammetry curves of Naf/MQD/GCE and Naf/HMQD/GCE at varying H_2O_2 concentrations (reprinted with permission from the American Chemical Society, copyright © 2021).[97] (c) CV curves of Ti_3C_2-MQDs@3DE in PBS for DA detection (reprinted with permission from Elsevier, copyright © 2023).[113] (d) Normalized PL spectra of $[Ru(dpp)_3]Cl_2$ and Ti_3C_2 MQDs at different pH levels (reprinted with permission from The Royal Society of Chemistry, copyright © 2019).[43] (e) Quartz BAW infrared detector response to NIR irradiation before/after coating (reprinted with permission from Optica Publishing Group, copyright © 2022).[157]

surrounding water molecules. The introduction of DPA replaces the water molecules and enhances the Eu^{3+} fluorescence intensity at 616 nm due to the absorbance energy-transfer effect (AETE) from DPA to Eu^{3+}. A visible fluorescence shift from blue to red with the DPA concentration enables quantitative detection by a smartphone equipped with color recognition software.[124]

In a recent study, Ti_3C_2-MQDs have been utilized to detect CUR, which has antioxidant, anti-inflammatory, antibacterial, and anticancer properties.[62] It is known that excessive amounts of CUR may boost DNA oxidative activity, lower Adenosine triphosphate (ATP) levels, and trigger necrotic processes.[62] Detection of CUR was achieved by leveraging the overlap between the emission peak of Ti_3C_2 MQDs at 430 nm and the absorption spectrum of CUR. When CUR is introduced, the fluorescence emission of Ti_3C_2 MQDs is quenched *via* FRET to CUR, while CUR fluorescence emission increases. Following the addition of ClO^- to this solution, the fluorescence emission of Ti_3C_2 MQDs is recovered, as CUR's phenol and methoxy groups are oxidized to quinones in the presence of ClO^-. The linear detection range of ClO^- has been found to be 25–150 μM and 150–275 μM, with a detection limit of 5 μM. For CUR, the linear detection range is 0.05–10 μM, with a LOD of 20 nM. The MQDs also exhibit a colorimetric response to CUR, which causes a visible color change from colorless to yellow.[99]

In addition to CUR, quercetin, a well-known antioxidant bioflavonoid, was detected by bright bluish-green emissive N-doped Ti_3C_2 MQDs.[126] The introduction of quercetin resulted in a significant fluorescence quenching due to static quenching/radiative-free complex formation and IFE. Consequently, the quantification of quercetin over a linear range of 25–600 nM with a low LOD of 1.35 nM was performed. The sensor demonstrated exceptional specificity for quercetin in real food samples, such as orange, onion, and red wine, with a quenching efficiency exceeding 95% compared to less than 10% for potential interferents. This finding demonstrates the significant potential of MQDs in various applications, including food safety, pharmacological assays, and the detection of various biological markers.[126]

Ti_3C_2 MQDs was also utilized to detect dopamine (DA), a catecholamine released by the adrenal medulla.[113] A Ti_3C_2 QDs@3D-printed electrode sensor enabled DA monitoring with a LOD of 3 nM over a linear range of 0.01 to 20 μM. CV determined an oxidative potential of 0.29 V for DA with an increasing trend in the current density with its concentration (Fig. 10c).[113]

Recently, a nanosurface molecularly imprinted polymer (Ti_3C_2 MQD@MIP) resonance Rayleigh scattering (RRS) spectral probe has been developed for the sensitive and selective detection of thiocyanate (SCN^-).[158] In this platform, Ti_3C_2 MQDs serve as the matrix, while SCN^- act as the template during the imprinting process. The functional monomer, (3-aminopropyl) triethoxysilane, and the cross-linker (tetraethoxysilane) facilitate the formation of the polymer network, with ammonia serving as the polymerization initiator. The detection mechanism is based on changes in RRS intensity, where the interaction between SCN^- and the Ti_3C_2 MQD@MIP probe results in a concentration-dependent reduction in scattering intensity. This allows for accurate quantification of SCN^- with a linear detection range of 0.87–5.22 μg L^{-1} and a LOD of 0.37 μg L^{-1}.[158] In another study, NO_2^- (nitrite), a crucial additive in food preservation, was successfully detected by the dual colorimetric/fluorometric method using N, P-Ti_3C_2 MQDs and the Phen-Fe^{2+} complex.[84] The fluorescence emission of N, P-Ti_3C_2 QDs was quenched by the Phen-Fe^{2+} complex *via* the IFE, accompanied by the intensified orange color. Upon the addition of NO_2^-, the redox reaction between NO_2^- and Fe^{2+} generated Fe^{3+}, reducing IFE by fluorescence recovery as well as a gradual change from orange to colorless. Using a smartphone-assisted colorimetric filter paper based on the N, P-Ti_3C_2 QDs/Phen-Fe^{2+} system, a linear relationship between the red, green, blue (RGB) ratio and NO_2^- concentration (up to 80 μM) was attained. More recently, N, B-doped Ti_3C_2 MQDs incorporated onto a functionalized paper were developed for the efficient adsorption and detection of dichromate ions ($Cr_2O_7^{2-}$).[159] The adsorption mechanism was attributed to a combination of electrostatic interactions and chemical bonding. The sensing mechanism involved fluorescence quenching *via* IFE with an efficiency of 99.9%, a response time of 10 s, and a LOD of 1.2 μM. The incorporation of green and renewable wood pulp fibers as raw materials further emphasized the potential of this innovative material for large-scale production and industrial application in water pollution management.[159]

5.1.7. pH sensors. N-$Ti_3C_2T_x$ MQDs have been introduced as one of the promising and efficient candidates for pH sensors. The pH dependent-fluorescence properties of the MQDs are attributed to surface functionalization, surface defects, protonation/deprotonation processes, and change in absorption and emission characteristics.[108] Measuring the fluorescence intensity of $Ti_3C_2T_x$ MQDs at various pH values under 365 nm excitation revealed a linear relationship between the ratio of 514 nm to 464 nm. The pH-responsive fluorescence was visually confirmed with blue emission at pH = 12.1 and green emission at pH = 2.0.[108]

The pH sensing potential of Ti_3C_2 MQDs, as effective ratiometric pH sensors, was also demonstrated when combined with the pH-insensitive $[Ru(dpp)_3]Cl_2$ dye.[43] This setup enabled precise intracellular pH monitoring *via* fluorescence intensity ratios. The ratiometric fluorescence change due to pH variations was characterized by a decrease in the intensity of the Ti_3C_2 MQD emission at 460 nm, while the emission of reference dye remained stable. A linear decrease in the fluorescence intensity ratio (I_{460}/I_{615}) with the pH in the range of 5 to 9 was noticed (Fig. 10d). This linear calibration curve for the fluorescence ratio (I_{460}/I_{615}) enabled accurate pH differentiation in the physiological range of 6.0 to 8.0. The sensors also demonstrated profound imaging and bio-labeling capabilities for reliable, long-term pH monitoring in biological environments.[43]

5.1.8. Physical parameters. Rehabilitation training plays a crucial role in aiding patients-such as those recovering from

strokes or car accidents-to regain motor functions after an injury. Personalized guidance from professionals is often necessary, demanding a significant allocation of human resources. Hence, there's an urgent need for a sensor that can precisely monitor patients' movement in real-time. Flexible pressure sensors demonstrate the ability to monitor and interpret diverse human motion signals like walking, pulse/heart rate, sound, hand, and knee movements.[38] These devices turn this physiological information into visualized, real-time impulse signals. Recently, Sun *et al.*[38] have evaluated, the sensitivity of MQDs within natural 3D watermelon peel matrix aerogels using a dynamic positioning system, collecting pressure-sensitive data *via* an electrochemical workstation. The resulting current–voltage curve demonstrates an increase in the current with the applied forces ranging from 0.02 to 20 kPa. The sensor's sensitivity also reveals distinct regions, including 323 kPa^{-1} for 0–0.4 kPa and 51.38 kPa^{-1} for 0.4–20 kPa. Thus, this sensor accurately detects various pressures, generating a recordable and analyzable current signal. In the design implementation, speech recognition controls sensors attached to the throat to differentiate phrases and vocal behaviors like "Hello" *versus* "Hi" and detect laryngeal swallowing patterns. The sensors can be fixed on different joints, such as the knee, elbow, and finger joints, to carry out corresponding tests. The signal waveforms are recorded as the sensors are fixed on the sole during fast walking, slow walking, running, and jumping. The sensor can accurately and quickly record the signals of different movements, which provides the possibility of the new-generation real-time remote monitor for sports rehabilitation. Measurement of the resonant frequency of a Y-cut quartz bulk acoustic wave (BAW) sensitive unit, fabricated by microelectromechanical systems, is employed for infrared sensing. Coating the surface of the quartz BAW resonator with the MQD film *via* spin coating technology significantly enhances the infrared absorption efficiency of the infrared detector, demonstrating promising potential for achieving high-performance infrared detection through the amalgamation of these two components. Test outcomes reveal a nearly 41% increase in the sensor's responsivity at an 830 nm wavelength following film coating, rising from 10.88 MHz W^{-1} to 15.28 MHz W^{-1}. This observation underscores substantial enhancement in the sensor's efficiency in absorbing infrared radiation (Fig. 10e).[157]

5.2. Optoelectronics

5.2.1. White light emitting diodes (WLEDs) and lasers. Multicolor and white light diodes hold significant potential for diverse applications, including bioimaging, full-color displays, optoelectronic devices, and PTT.[160] A common approach to producing white light is the combination of a blue LED with a yellow phosphor because most of the fluorescent materials are incapable of directly emitting pure white light.[160] However, this method lacks sufficient red (or other colors) spectral components, resulting in a lower color rendering index (CRI). Recently, the fabrication of novel LEDs has focused on leveraging strong quantum confinement in QDs to achieve tunable band gaps, enabling the emission of light at different wavelengths.[161,162]

One of the earliest MQDs-based WLED with Commission Internationale de l'Éclairage (CIE) coordinates of (0.31, 0.35) was fabricated by Xu Quan *et al.*[9] in 2019. To fabricate this device, which was stable at a voltage of 3 V after a month (Fig. 11a), $Ti_3C_2T_x$-MQDs were hydrothermally co-processed with sodium thiosulfate (S-doped), an ammonia solution (N-doped), and a combination of these two (SN-doped) to emit blue (440 nm), yellow (540 nm), and orange (580 nm), respectively, followed by mixing with polyvinylpyrrolidone (PVP) and casting on a blue chip. Similar to lead-free double perovskites and SiC QDs, Ti_3C_2 MQDs also manifested great potential to be used for single-component white LEDs (Fig. 11b).[127,163] In this case, a hybrid nanocomposite was prepared by polymerizing Ti_3C_2 MQDs, having strong two-photon white fluorescence with the full width at half maximum (FWHM) and PLQY of 220 nm and 9.36%, respectively, in a polydimethylsiloxane solution. This working LED could emit white light with the color coordinates of (0.30, 0.34). Moreover, the fluorescence of the Ti_3C_2 MQDs under high pressure (2.53 GPa) enabled tuning the white emission temperature from cool to warm, (Fig. 11c) which is a fascinating phenomenon for the next generation of single-component warm WLEDs.[127]

White lasers are increasingly important in fields such as laser display technology, communication technology, biomedicine, and environmental detection.[164–167] To fabricate white lasers, a wide range of materials, including dye mixtures[168] semiconductors,[169] laser or nonlinear optical crystals,[166] and QDs[128] have been used.[170–172] However, constrained by compactness, difficulty in growth or wavelength control, and environmentally unfriendly chemicals, white lasers are still underdeveloped, and the available materials and approaches are still being extensively sought. One of the most promising white lasers was fabricated by Huang *et al.*[128] using V_2C MQDs. By employing passivation treatments, the PL intensity of V_2C MQDs, spanning the entire visible spectrum, was significantly enhanced. Fig. 11d illustrates the light emission images of passivated V_2C QDs under various excitation wavelengths. The localized nonlinear random scattering of the passivated V_2C MQDs has been achieved through the generation of excitation-power-dependent solvent bubbles. This phenomenon plays a critical role in producing a white laser with multiple color outputs. With optimized excitation conditions, the amplification and simultaneous lasing of blue (490 nm), green (545 nm), yellow (587 nm), and red (613 nm) light has been demonstrated.

5.2.2. Solar cells. With a high-power conversion efficiency (PCE) of 25.7%,[173] perovskite solar cells (PSCs) have become a strong candidate for the next generation of energy harvesters.[174,175] However, preparing a perovskite thin film with high crystallinity and long-term stability against severe humidity is an important issue for commercialization.[176–178] Among various strategies, the modification of perovskite thin films by appropriate materials has become an effective approach to meet both requirements.[179] To this end, MXenes

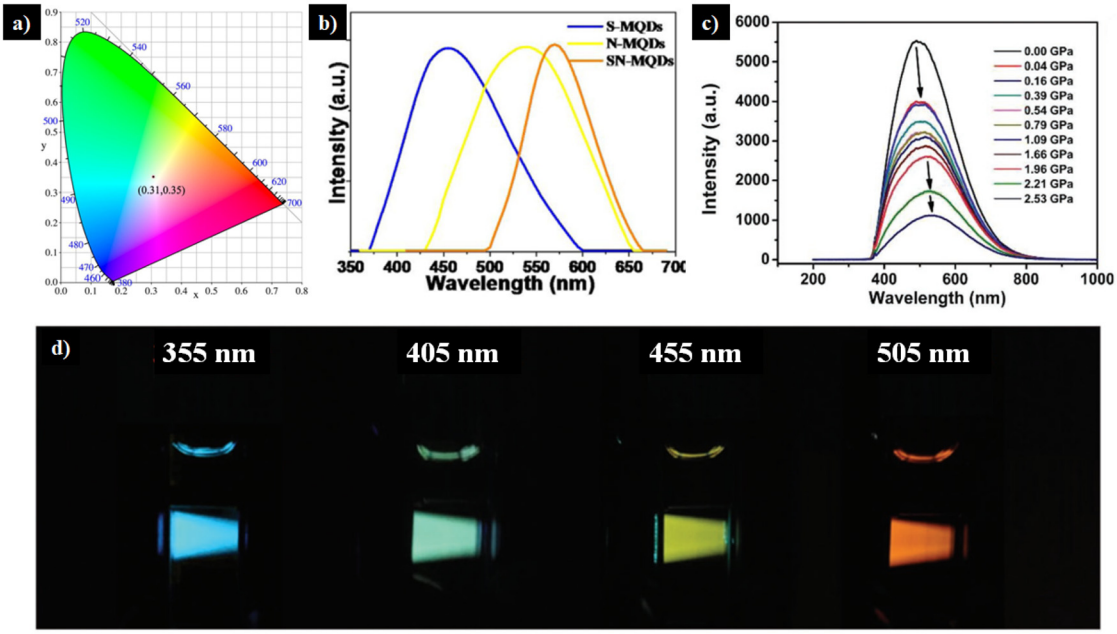

Fig. 11 (a) CIE coordinates of WLED based on MQDs/PVP under 360 nm excitation. The inset showing fluorescence images of the W-MQDs/PVP composite under 365 nm emission (reprinted with permission from Elsevier, copyright © 2019).[9] (b) PL spectra of the visible-light-emitting MQDs under 360 nm emission (reprinted with permission from Elsevier, copyright © 2019).[9] (c) PL spectra of Ti_3C_2 QDs depending on the applied pressure (reprinted with permission from Wiley, copyright © 2019).[127] (d) Images showing different excitation wavelengths for V_2C MQDs (xenon lamp) (reprinted with permission from Wiley, copyright © 2019).[128]

could be a promising material due to their metallic conductivity, high carrier mobility, profound optical transparency, tunable work function, and superior mechanical properties.[180] Their diverse transition elements and surface-terminating groups also allow for tuning band energy alignment between absorber and charge transport layers, improving charge carrier extraction.[181] It has been demonstrated that incorporating MXenes in PSCs reduces interfacial recombination resistance and facilitates smooth charge transfer paths, enhancing the conductivity and stability of PSCs.[182] However, MXene fails to address the challenge of the small crystal size in the perovskite layer, which can negatively impact the PCE.[183] This limitation has led researchers to explore the use of MQDs, offering quantum confinement effect and fruitful surface terminations, high surface area, and improved charge transport, making them a promising alternative for enhancing the performance of PSCs.[184,185]

For instance, incorporation of Cl-terminated Ti_3C_2 MQDs into the $FA_xMA_{1-x}PbI_3$ perovskite could increase the PCE from 19.53% to 21.31%. Not only short-circuit current density (J_{sc}) and open-circuit voltage (V_{oc}) of the cells increased, but also the difference between the forward and reverse scan curves, called normal hysteresis, decreased (Fig. 12a and b). This performance improvement can be attributed to two key factors. First, the strong interactions between the Cl terminations of $Ti_3C_2Cl_x$ and Pb^{2+} ions promote a preferred grain orientation with reduced residual tensile strain by slowing the crystallization rate, thereby improving the crystallinity of the perovskite film. Second, the natural formation of a top-down gradient distribution leads to a higher concentration of $Ti_3C_2Cl_x$ MQD additives near the bottom substrate. These additives serve as nucleation sites for the growth of high-quality perovskite crystals to facilitate efficient charge extraction between the SnO_2 electron transport layer (ETL) and the perovskite layer. Besides, Cl-terminated $Ti_3C_2T_x$ MQDs avoid possible deprotonation of protonated organic amine in perovskite. Consequently, the solar cell exhibits outstanding long-term stability by maintaining over 84% of its initial PCE after being aged for 1000 h under 40% relative humidity.[129] In another study, the $MAPbI_3$ perovskite and TiO_2 layers were modified by Ti_3C_2 MQDs and MXene nanosheets, respectively. Apart from the positive effect of nanosheets on electron mobility improvement of the ETL, 0.8 mg MQDs reduced defects concentration *via* successful perovskite film passivation and increased perovskite crystallinity. These claims could be supported by an enhancement in the PL emission intensity and carrier lifetime, as shown in Fig. 12c–e. As a result of this modification, the PCE improved from 12.0% to 17.1%, along with the reduced hysteresis effect.[34]

Similar to MXene nanosheets, the ETL modification by MQDs manifested great potential to boost both PCE and stability. For instance, it was demonstrated that the introduction of Nb_2C MQDs into SnO_2 (as the ETL) was effective in enlarging the grains, modifying the roughness and surface energy, and reducing defect sites.[130] Subsequent deposition of $Cs_{0.05}(FA_{0.83}MA_{0.17})_{0.95}Pb(I_{0.83}Br_{0.17})_3$ perovskite films on the

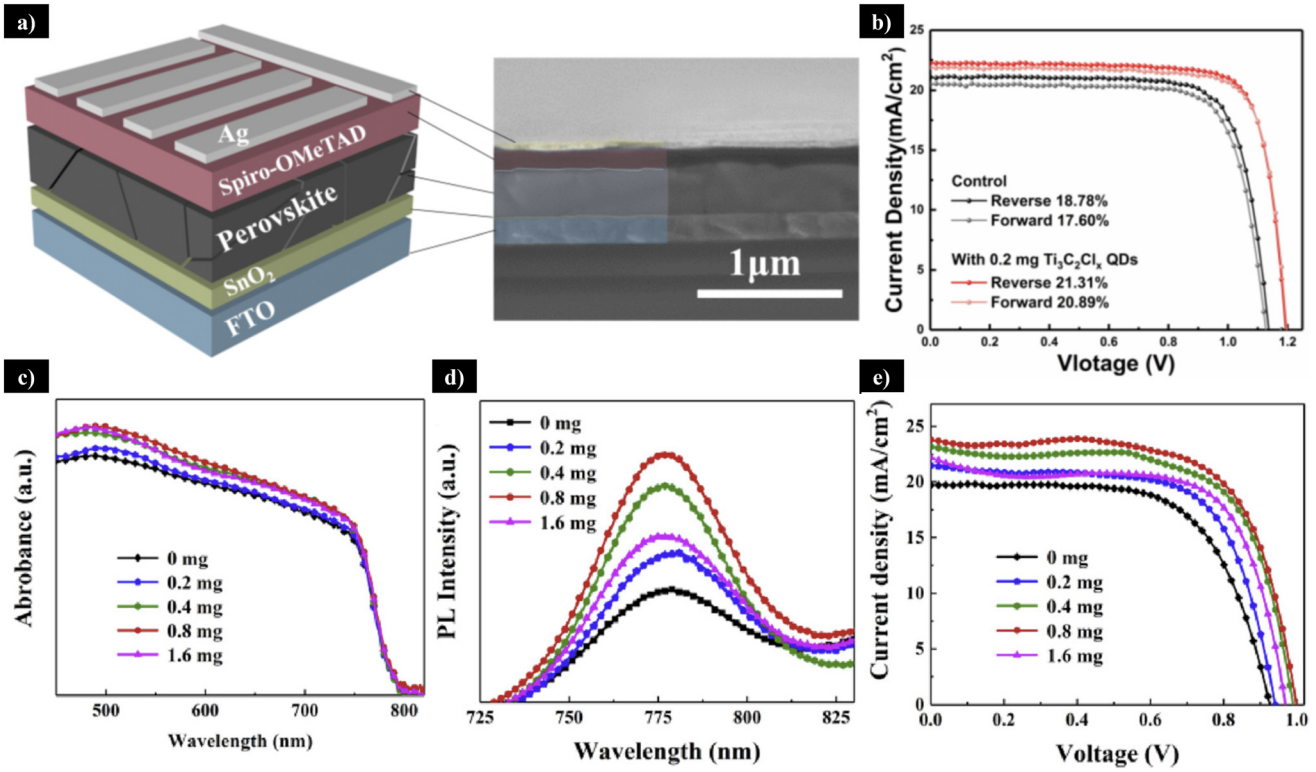

Fig. 12 (a) Schematic illustration of the $Ti_3C_2Cl_x$ MQDs-treated $FA_xMA_{1-x}PbI_3$ PSCs with colored cross-sectional scanning electron microscopy (reprinted with permission from Elsevier, copyright © 2022).[129] (b) Reverse and forward scans for the pristine and 0.2 mg mL^{-1} $Ti_3C_2Cl_x$ MQDs-treated solar cells (reprinted with permission from Elsevier, copyright © 2022).[129] (c) UV-Vis absorption spectra, (d) PL spectra, and (e) *J*–*V* curve of perovskite films with different content of Ti_3C_2 MQDs (reprinted with permission from Elsevier, copyright © 2020).[34]

SnO_2–Nb_2C ETL enhanced perovskite crystallinity and effective carrier transport, leading to a PCE of 22.86%. The device maintained 98% of its as-prepared efficiency after 40 days holding at 25 °C under 40–60% humidity (Fig. 13a and b).[130] In another survey, an *in situ* synchrotron-based two-dimensional grazing-incidence X-ray diffraction (GIXRD) technique was used to explore the effect of $Ti_3C_2T_x$ MQDs-modified SnO_2 (MQDs-SnO_2) on the perovskite crystallization kinetics.[131] It was shown that the modified structure facilitated perovskite nucleation from the precursor solution, forming an intermediate perovskite phase upon anti-solvent treatment. As a result, a substantial improvement in the crystal quality and phase stability of the perovskite film was achieved. As shown in Fig. 13c–e, the more uniform and larger grain sizes, the more light absorption capacity, the shorter lifetime in TRPL, and the much brighter scattered rings in GIXRD patterns underscore the better crystallinity and charge extraction in the target layer compared to the reference cells. The steady-state PCE of up to 23.3% as well as outstanding stability against humidity and light soaking was achieved for the corresponding PSCs due to the superior charge extraction properties of the MQDs-SnO_2 layer.[131] Xu Chen *et al.*[186] prepared high-performance $Cs_{0.05}(FA_{0.83}MA_{0.17})_{0.95}Pb(I_{0.83}Br_{0.17})_3$ PSCs with simultaneously improved performance and stability *via* incorporating $Ti_3C_2T_x$ MQDs into the ETL and active layer. The incorporation of MQDs in the mesoporous TiO_2 reduced the interfacial defects and improved the electron extraction and injection from the perovskite absorber into the mesoporous TiO_2. On the other hand, introducing MQDs into the perovskite active layer increased the crystallization size and conductivity of the perovskite, while reducing the grain boundaries and the intrinsic defect density, by passivating the charge recombination centers. The MQD-modified PSCs exhibited a hysteresis-free response with a PCE of 21.64%, which was remarkably higher than that of the reference device (18.31%).[186]

MQDs have also been used for structural modification of dye-sensitized solar cells (DSSCs) towards higher efficiencies.[132] The PCE of DSSCs still requires further improvement despite their apparent benefits such as low-cost preparation, multicolor transparency, and a wide range of practical applications.[132] Recently, substantial increase in the photocurrent and efficiency of DSSCs has been achieved by successfully altering the energy level alignment of TiO_2 photoanode through the introduction of niobium oxide (Nb_2O_5) and Ti_3C_2 MQDs. The modified photoanode exhibits a distinct mesoporous structure, offering high dye adsorption and with a broader absorption range in the visible region. An improved charge transfer suppressed electron–hole recombination at the photoanode interface, and enhanced PCE (7.24%) relative to the reference group (4.60%) has been demonstrated.[132]

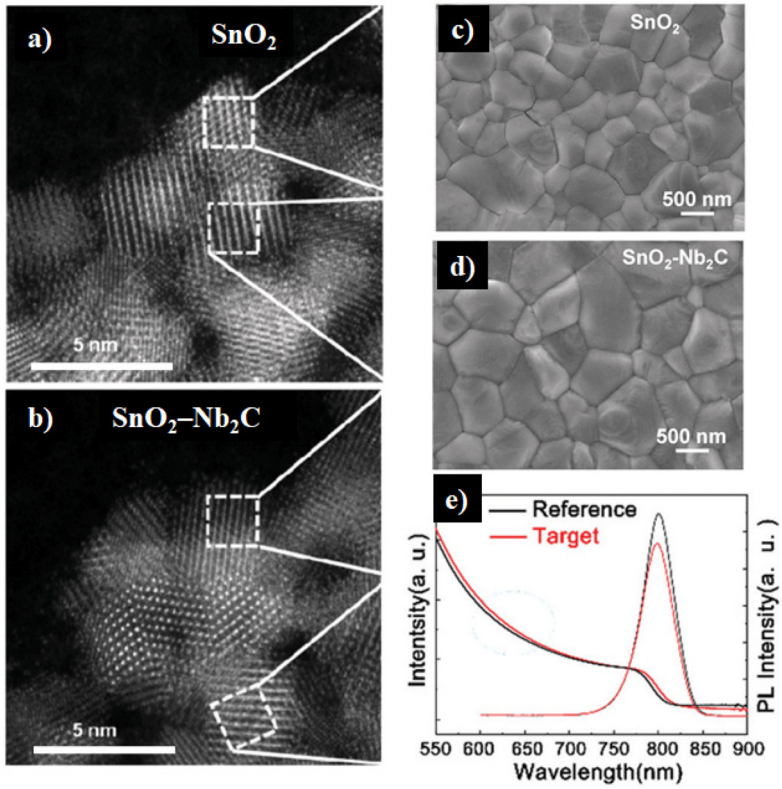

Fig. 13 High-Angle Annular Dark-Field Scanning Transmission Electron Microscopy (HAADF-STEM) images of (a) SnO_2 and (b) SnO_2–Nb_2C MQDs (reprinted with permission from Elsevier, copyright © 2021).[130] The SEM images of the perovskite films deposited on (c) SnO_2 and (d) SnO_2–Nb_2C MQDs ETL basement.[130] (e) UV-vis absorption and PL spectra of the reference and target perovskite films (reprinted with permission from Royal Society of Chemistry, copyright © 2021).[131]

5.2.3. UV detectors. Excessive exposure to ultraviolet (UV) radiation can have harmful effects on the skin, causing premature aging, sunburn, and an increased risk of skin cancer.[187] Both UVA (315–400 nm) and UVB (280–315 nm) rays can cause damage. Although the latter is the main cause of sunburns and is thought to contribute to most skin cancers, the former is associated with skin aging. Given the potential health risks associated with UV exposure, there is a need for efficient UV detectors to help individuals monitor their exposure levels and take necessary precautions to protect their skin.[188,189] Several categories of QDs have been widely explored for UV photodetection, including II–VI semiconductor QDs (*e.g.*, CdSe), metal oxide QDs (*e.g.*, ZnO), carbon-based QDs (such as nitrogen-doped carbon QDs), perovskite QDs (*e.g.*, $CsPbCl_3$, $CsPbBr_3$), and graphitic carbon nitride (g-C_3N_4) QDs. These materials exhibit strong UV absorption, tunable bandgaps, and favorable photoelectric conversion efficiency, making them suitable for diverse photodetector architectures. In comparison, MQDs provide several unique advantages for UV detection. Owing to their intrinsically high dielectric constants and extinction coefficients, MQDs enable superior light absorption and facilitate efficient separation of photogenerated charge carriers, resulting in enhanced responsivity and quantum efficiency. Their rich surface chemistry allows versatile functionalization and heteroatom doping, offering additional control over sensitivity and electronic coupling at device interfaces. Furthermore, MQDs display remarkable chemical stability and biocompatibility, with significantly reduced cytotoxicity relative to conventional QDs such as CdSe and even their 2D MXene parent structures. Benefiting from pronounced quantum confinement and edge effects, MQDs also exhibit excellent photostability and strong light–matter interactions, enabling efficient conversion of optical energy into electrical or thermal signals. These collective attributes render MQDs a promising class of materials for next-generation, flexible, and bio-integrated UV photodetectors.[190–192]

Similar to MQD-modification of ETL in solar cells, MQDs have been used to enhance UV detector performance. For instance, Yiqiang Zheng *et al.*[8] used $Ti_3C_2T_x$ MQDs to enhance charge carriers and light absorption of 2D perovskite $Ca_2Nb_3O_{10}$. The results showed a 1100% increase in spectral responsivity (264 A W^{-1} at 310 nm) compared to the reference photodetector without MQDs. The flexible MQDs/perovskite photodetector was then integrated with a data collector to simulate a wearable visible-blind UV monitoring system for skin and plant protection. The ambient UV radiation information in various weather conditions could be trained and recognized by an artificial neural network to alert users.[8]

Similar to MQD-modification of ETL in solar cells, MQDs have been used to enhance UV detector performance. For instance, Yiqiang Zheng *et al.*[8] used $Ti_3C_2T_x$ MQDs to enhance charge carriers and light absorption of 2D perovskite $Ca_2Nb_3O_{10}$. The results showed a 1100% increase in spectral responsivity (264 A W^{-1} at 310 nm) compared to the reference photodetector without MQDs. The flexible MQDs/perovskite photodetector was then integrated with a data collector to simulate a wearable visible-blind UV monitoring system for skin and plant protection. The ambient UV radiation information in various weather conditions could be trained and recognized by an artificial neural network to alert users.[8]

5.2.4. Ultrafast photonics. Ultrafast lasers, which show short pulse duration from picosecond to femtosecond regions and high pulse energy, has garnered tremendous attention. Materials with nonlinear optical properties are commonly used as a saturable absorber, which is one of the most important parts of an ultrafast laser system.[193] Other types of QDs such as CdSe, graphene, MoS_2, $NbSe_2$ and phosphorene are extensively used in ultrafast photonics and ultrafast laser systems as saturable absorbers due to their strong nonlinear optical properties and ability to generate ultrashort laser pulses. These QDs enable the generation of femtosecond to picosecond laser pulses and are exploited for high-speed optical communications, medical imaging, and advanced sensing technologies. MQDs offer several advantages over traditional QDs in ultrafast photonics. MQDs show a much larger nonlinear absorption coefficient and ultrafast carrier dynamics, with transient absorption signals. When used as saturable absorbers, MQDs enable the generation of femtosecond laser pulses with high signal-to-noise ratios and ultranarrow linewidths, surpassing many conventional QD materials. Their tunable surface terminations and high modulation depth allow for low-threshold mode-locking and efficient ultrafast pulse generation, making them ideal for fiber laser applications. MQDs also exhibit exceptional stability and photodurability, further supporting their advantage for robust ultrafast photonic devices.[194–196] Among 2D materials, MXenes have attracted huge attention due to their outstanding photoelectric characteristics and adjustable performance caused by flexible compositional or surface functional group regulation. For instance, Fumei Yang *et al.*[77] used $Ti_3C_2T_x$-MQDs with various functional groups to fabricate a tapered fiber saturable absorber device for an Er^{3+}-doped fiber laser. The single-mode fiber was stretched into a tapered fiber using a fiber TEC machine. The photo deposition method was then employed to stably transfer $Ti_3C_2T_x$ QDs to the tapered area to fabricate the saturable absorber. The process involved dispersing the material in a solution, immersing the substrate, and exposing it to light to initiate the deposition. The size and abundance of the deposited nanosheets could be controlled by regulating the immersion time. Compared to other QDs such as PbS QDs, the saturable absorber device exhibited a low saturation intensity (1.983 GW cm^{-2}) and high modulation depth (11.6%), enabling easier mode-locked pulse generation. The device produced ultrashort pulses of 466 fs at a wavelength of 1566.57 nm with a fundamental frequency of 22.78 MHz in the communication band.[46]

5.2.5. Nonvolatile memory devices. Nonvolatile memory refers to computer memory that can retain stored information even when power is removed and this is in contrast to volatile memory, which requires constant power to maintain data. Some key characteristics of nonvolatile memory devices include the ability to retain data without power, re-writability, and faster access times than traditional storage.[197] New nonvolatile memory technologies aim to provide even faster speeds, higher densities, and improved endurance compared to flash memory.[197,198] Incorporating hydrothermally prepared $Ti_3C_2T_x$-MQD in PVP films enables precise tunning of the electrical conductance of an indium tin oxide (ITO)/MQD-PVP/ structure from insulator behavior to irreversible resistive switching, reversible resistive switching, and conductor behavior.[133] Schematic images and *I–V* diagrams for different concentrations of $Ti_3C_2T_x$-MQD (C_a = 3.42 mg mL^{-1}, C_b = 1.14 mg mL^{-1}, C_c = 380 μg mL^{-1}, C_d = 20 μg mL^{-1}) are shown in Fig. 14a–h. As seen, the currents for voltage sweep in positive

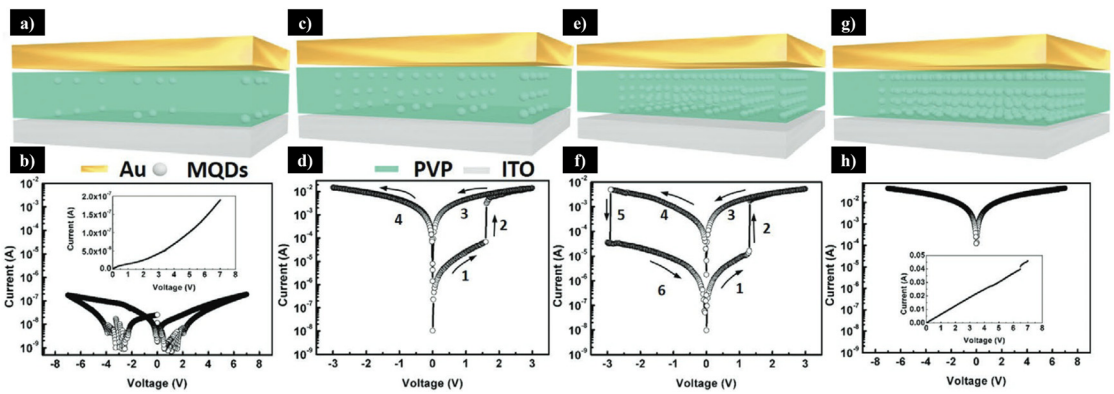

Fig. 14 Memory unit and *I–V* characteristics of MQDs-PVP memory devices containing (a and b) C_d, (c and d) C_c, (e and f) C_b, and (g and h) C_a (reprinted with permission from Wiley, Copyright © 2019).[133]

and negative directions are completely different. The hybrid films with irreversible and reversible resistive switches demonstrate write-once-read-many times and flash memory effects, respectively. These devices also exhibit stable operation during a long retention test (1.2×10^4 s), with a high on/off current ratio of up to 100. The tunable memory and transient features of these hybrid films are likely due to MQD charge trapping, which is a result of their quantum confinement and the dissolvability of memristive components. Overall, MQDs hold promise as resistive switching triggers for emerging nonvolatile memories for data storage, particularly in data storage security applications.[129]

5.3. Energy

Incorporation of MQDs can play a key role in enhancing energy storage efficiency in batteries and supercapacitors by improving electrochemical reaction kinetics and thermodynamics. This results in higher capacitance and energy density, facilitated by improved ion transport, species adsorption, and surface reactions to develop more efficient, high-capacity, and long-lasting energy storage devices. In the following section, we will explore various types of energy storage devices, highlighting the mechanisms behind the performance improvements when MQDs are incorporated.

5.3.1. Energy storage devices. There are several reasons why MQDs are considered promising candidates for enhancing the performance of energy storage devices, such as batteries and supercapacitors; (i) the presence of abundant surface terminations enhances electrochemical performance, and their small lateral size allows molecule and ions accessibility,[199,200] (ii) they benefit from superior electron transport efficiency, (iii) their layered structure could avoid mechanical degradation during charge–discharge cycles, accommodating the crystallographic strain from ion intercalation due to volume expansion, (iv) dopants in QDs can enhance redox reaction kinetics by their localized mid-gap electronic states as highly active catalytic sites, ultimately leading to longer lasting and more efficient batteries.[201–203] Despite these advantages, MQDs face challenges for large-scale commercialization.[204] Recent advancements aim to address the long-lasting issue of aggregation of QDs over time.[205] Strategies for enhancing the surface-active sites through surface functionalization,[206] and introducing them into heterostructure settings[207] are crucial ongoing step forward to overcome limitation of energy storage applications of MQDs.[199,200]

To fully understand the role of MQDs in energy storage and conversion devices, several key parameters must be considered. Specific capacitance (F g^{-1}) measures the ability of the material to store charge per unit mass, which is a crucial parameter for energy storage systems. Cycling stability refers to the number of charge–discharge cycles an electrode material can undergo while maintaining performance. Overpotential (V) is the extra voltage required for electrocatalytic reactions, such as redox reactions, which should be minimized to improve energy efficiency.[208] Power density (W kg^{-1}) and energy density (Wh kg^{-1}) define how much power and energy a material can deliver, particularly for supercapacitors.[208–212] Charge carrier lifetime represents the duration of photogenerated charge carriers remaining separated before recombination, a critical factor in photocatalysis. Lastly, coulombic efficiency (CE) and faradaic efficiency (FE), and apparent quantum yield (AQY) are quantifying indicators of the cycle-to-cycle efficiency and ratio of the actual amount of product formed to the theoretical amount, and performance metric of photocatalysis that measures the fraction of absorbed photons, respectively.[213,214] In the following sections we will delve into each application and explain recent achievements in each area to have a deeper understanding of energy storage applications of MQDs.

- **Lithium–oxygen batteries**

Li–O_2 batteries, leveraging oxygen redox reactions, offer a high theoretical energy density of 3000 Wh kg^{-1}.[215] Electrocatalysts play a crucial role in these systems by accelerating reaction kinetics, minimizing energy losses, and enhancing battery stability, making them key to improving performance and cyclability.[12,216] Among various electrocatalysts for electrochemical applications, the unique properties of MXenes such as good electrical conductivity,[133] edge active catalytic sites,[135] tunable structure,[136] and dispersibility[146] make them highly suitable for oxygen reduction/evolution reactions.[217] However, literature reports on 2D materials, particularly MXenes, still lacks a systematic framework for the rational design of highly active electrocatalysts for such an application.

To address this challenge, various strategies, ranging from defect engineering to doping, have been explored.[218–220] Defect-rich structure of MQDs, owing to higher edge-to-basal plane surface area ratio, can effectively improve electrochemical performance of carbon nanosheets (CNSs), while maintaining the same chemistry as their MXene counterparts.[221] Ti_3C_2 MQD/CNSs catalysts demonstrated a remarkably low voltage gap of 0.62 V, which is substantially lower than 1.29 V for Ti_3C_2 nanosheets/CNSs (Fig. 15a). Besides, Ti_3C_2 QDs/CNSs cathode delivered a high discharge capacity of ~16 000 mAh g^{-1} with a CE of 93.8%, outperforming Ti_3C_2 nanosheets/CNSs (~11 000 mAh g^{-1}, 70.9%). In terms of stability, the former was stable during 240 cycles at 200 mA g^{-1} compared to 65 cycles for the latter. DFT calculations unveiled the relation between electron rearrangement over the grain boundaries and edge sites, helping charge transfer between intermediates and active sites during redox reactions. While for Ti_3C_2 sheets, charge accumulation was restricted to oxygen-containing clusters, confirming the inactivity of basal planes, MQDs showed stronger chemical affinity to LiO_2 intermediates. This finding was attributed to the fact that Li^+ and oxygen atoms could attach to edge rich C-side and functional groups of the edge-rich MQDs as catalytically active sites. Edge defects altered local charge distribution, modulated intermediate adsorption behavior of oxygen species needed for storage of products, and reduced redox energy barriers during Li_2O_2 formation/decomposition.[222]

- **Zinc–air batteries**

Zinc–air battery (ZAB) is a promising energy storage system which benefits from vast utilization of aqueous electrolytes

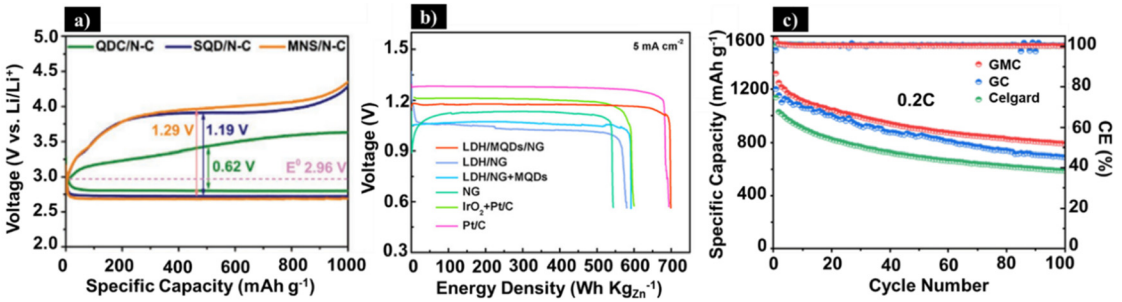

Fig. 15 MQDs as a key component of different type of batteries. (a) Li–O_2 battery: the discharge–charge curves of electrodes at a fixed capacity of 1000 mAh g^{-1} and current density of 200 mA g^{-1}. QDs as cathode material showed lowest charge overpotential compared to nanosheets (0.62 V) (reprinted with permission from Wiley, copyright © 2021).[222] (b) Zn–air battery: the energy density of rechargeable ZABs with LDH/Ti_3C_2-MQDs/NG hybrids, LDH/NG hybrids, LDH/NG + MQDs, bare NG, commercial Pt/C, and IrO_2 + Pt/C air cathodes at a discharge current density of 5 mA cm^{-2} demonstrating a higher energy density for QDs containing sample (~700 Wh kg^{-1}) (reprinted with permission from Wiley, copyright © 2021).[223] (c) Li–S battery: long-term cycling of the battery with various separators (red: GMC, blue: GC, green: Celgard) at 0.2C (reprinted with permission from Royal Society of Chemistry, copyright © 2023).[224]

and high theoretical energy density of 1086 Wh kg^{-1} (five times higher than that of Li-ion).[225] Although traditional noble metal-based electrocatalysts, such as Pt- and Ir/Ru-based materials perform well in electrocatalytic reactions, they still suffer from high costs and poor long-term stability. A major constraint to novel materials in zinc–air batteries is their sensitivity to the CO_2 concentration in air. Among different methods to overcome this issue, such as electrolyte optimization and electrode engineering,[226] developing highly active electrocatalysts for oxygen redox reactions has gained significant attention.[227,228] Considering that layered double hydroxide (LDH) nanosheets have limited conductivity and sluggish catalytic kinetics,[229] the introduction of MQDs to LDH/N-doped graphene (NG) is effective in boosting kinetics of oxygen reduction reaction (ORR) and oxygen evolution reaction (OER) during cycling.[229] Confirmed by Mott–Schottky analysis and DFT calculations, LDH/Ti_3C_2 MQD/NG hybrid exhibits higher carrier density and a deeper Fermi level while pristine LDH suffers from poor charge transport. The LDH/Ti_3C_2-MQD hybrid also shows a lower Tafel slope (57 mV dec^{-1}) than Pt/C (120 mV dec^{-1}), indicating faster reaction kinetics. Furthermore, the MQD-enhanced hybrid offers a high energy density of 700 Wh kg^{-1}, matching commercial Pt/C and far exceeding IrO_2 (580 Wh kg^{-1}) (Fig. 15b), and low potential difference of 0.81 V, significantly outperformed LDH/NG (0.92 V), commercial Pt/C (1.01 V), and IrO_2 + Pt/C (0.91 V). The material's structural integrity during prolonged operation (150 h at 5 mA cm^{-2}) and its mechanical flexibility, even in a bent state, highlights its potential for applications beyond batteries, such as wearable electronics.[223]

- **Lithium–sulfur batteries**

Li–sulfur (Li–S) batteries stand out among many candidates as the next generation of energy storage devices due to their high theoretical capacity (1675 mAh g^{-1}) and the abundance of sulfur.[230] However, industrialization of this type of battery is hindered by the shuttle effect of lithium polysulfides (LiPSs) and irreversible energy loss, leading to poor performance and cyclability.[231] Strategies to mitigate this include engineering the sulfur host, such as using free-standing N-doped carbon/$Ti_3C_2T_x$ MQDs (NC-S/$Ti_3C_2T_x$) films; this design uses polar N-doped carbon to anchor LiPSs while the $Ti_3C_2T_x$ network provides conductivity and a physical barrier, enabling high areal capacities up to 3.41 mAh cm^{-2}.[215,232]

A game-changing solution emerges with the introduction of an ion selective layer in electrolyte to capture LiPS. Through local confinement enabled by the small size of MQDs and their abundant active sites for polysulfide adsorption, the g-C_3N_4@$Ti_3C_2T_x$ MQDs-modified Celgard (GMC) separator forms a highly functional modification layer.[224] This approach leverages the strong interactions of polar materials to gradually trap and accumulate polysulfides, effectively creating a shuttle barrier between the cathode and anode. As a result, a significant improvement in the efficiency of polysulfide conversion is attained. A long-term stability with only 0.024% capacity decay per cycle after 1000 cycles at 2C and the retention rate of nearly 70% at 0.2C after 100 cycles are also obtained. The retention rate is higher than that of the Li–S batteries assembled with unmodified g-C_3N_4 Celgard separator (58%), ensuring significantly extended lifespan compared to traditional designs (Fig. 15c). The modified separator also enhances the stability of Li_2S deposition (final discharge product), as evidenced by longer and more stable plateau regions in discharge curves.[224] By efficiently capturing, confining, and catalyzing polysulfide conversion, MQDs eliminate the shuttle effect bottleneck in Li–S batteries.

- **Supercapacitors**

A flexible power supply is an essential component of portable and wearable electronic devices. Supercapacitors with high power density, long cycle life, and fast charging capabilities have garnered considerable attention in this field. They are lightweight, compact, and operate efficiently across a wide temperature range, making them suitable for portable, energy-efficient devices. The key to providing such engineering products to the market is how to increase their volume energy

densities without sacrificing their volume power densities, life cycles, and other performance parameters.[233] To achieve high volumetric energy density, recent research has focused on new strategies, such as fabrication of hybrid capacitors,[234] utilizing high-voltage ionic liquid electrolytes,[235] preparing high surface area electrodes,[221,236] and all-solid-state systems.[233]

Among other flexible electrodes, integrating 2–4 nm $Ti_3C_2T_x$ MQDs into RGO/$Ti_3C_2T_x$ fiber electrodes (Q3M7) overcame a long-standing challenge in solid-state electrolyte supercapacitors by providing a trade-off between high capacitance and mechanical flexibility.[237] Using MQDs as pillar agents, a highly conductive, structurally stable fiber was obtained. An exceptional volumetric capacitance of 1560 F cm^{-3} at 1 A cm^{-3} in 1 M H_2SO_4 (solution-based electrolyte) was also achieved, which is far surpassing other MXene-based fibers such as $Ti_3C_2T_x$/PEDOT:PSS (poly(3,4-ethylenedioxythiophene)polystyrene sulfonate) (614 F cm^{-3}) and $Ti_3C_2T_x$/RGO (542 F cm^{-3}). The Nyquist plots revealed a lower charge transfer resistance, confirming MQD pillars create expanded interlayer channels, which minimize ion transport tortuosity and facilitate rapid pseudocapacitive intercalation and ion diffusion and electrolyte accessibility by adding MQDs.[215,238] Even a 20× higher current densities (20 A cm^{-3}) gave rise to a capacity retention of 79%, compared to the 61% in $Ti_3C_2T_x$/PEDOT:PSS fibers.[239] When assembled into an all-solid-state supercapacitor, the MQD-enhanced electrode demonstrated a volumetric capacitance of 413 F cm^{-3} at 0.5 A cm^{-3}, an energy density of 36.7 mWh cm^{-3}, and an impressive 97% capacity retention after 10 000 cycles, which hardly changed over time. Additionally, the Q3M7 fibers boast a remarkable mechanical strength of 130 MPa, ensuring their suitability for wearable and flexible electronics. Moreover, no change observed to the capacitive behavior of the fibers after bending, confirming the flexibility of this system under bending test (Fig. 16a).[237] The volumetric energy density exceeded that of commercial supercapacitors (*e.g.*, 2.75 V/44 mF, and 5.5 V/100 mF), but also outperformed previously reported MXene- and RGO-based designs (*e.g.*, MnO_2/$Ti_3C_2T_x$/RGO, $Ti_3C_2T_x$/PET fiber, $Ti_3C_2T_x$/CNT fiber, V_2O_5/single-walled carbon nanotube) (Fig. 16b).[237]

While flexibility is important, in the pursuit of transparent high-performance energy storage devices, researchers have faced a persistent challenge in balancing high transparency with efficient energy storage. The key to this issue lies in utilization of temporally and spatially shaped femtosecond laser to uniformly attach MQDs to laser-reduced graphene oxide (LRGO).[236] The presence of nanosized $Ti_3C_2T_x$-MQDs and higher density of edges compared to basal sites provides a high-power density and areal capacitance of 2.04 × 10^{-3} mWh cm^{-2} and 10.42 mF cm^{-2}, respectively. Well-distributed MQDs prevented restacking of graphene nanosheets (Fig. 16d), while providing more active sites for charge storage and transfer, thereby offering a flexible, ultrahigh transparency supercapacitor (areal capacitances = 10.42 mF cm^{-2} and transmittance = 91%) with high durability, *i.e.*, maintaining 97.6% of its capacitance after 12 000 cycles.[236] In another study,[137] $Ti_3C_2T_x$-MQDs were introduced into the $Ti_3C_2T_x$ nanosheet

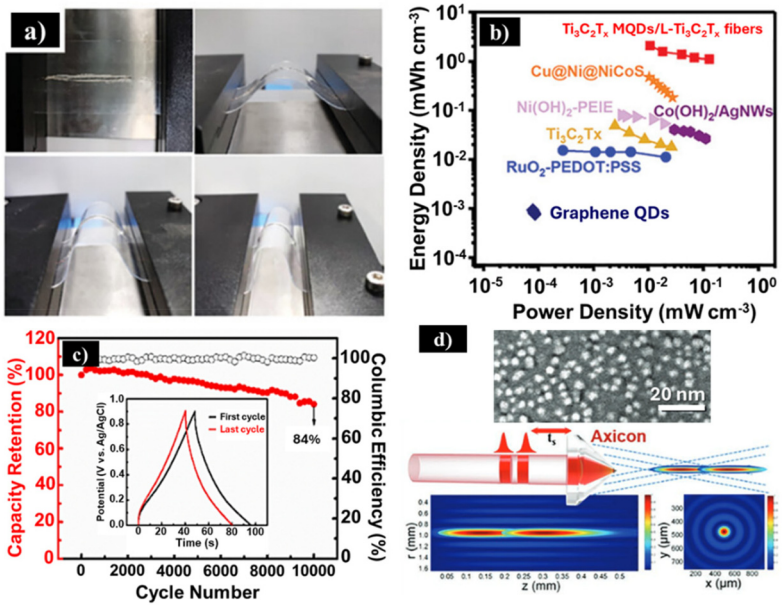

Fig. 16 (a) Mechanical bending test showing the flexibility of solid-state supercapacitor system based on $Ti_3C_2T_x$ MQDs/L-$Ti_3C_2T_x$ fibers made with MQDs confirming flexibility after multiple bending steps (reprinted with permission from Wiley, Copyright © 2023).[237] (b) Ragone plot indicating the potential of the MQD containing fibers at top right corner of energy density *vs.* power density plot (highest compared to other works) (reprinted with permission from Wiley, copyright © 2022).[236] (c) Capacitance retention and CE of the 0D/2D MQD/MXene symmetric solid-state pseudocapacitor after 10 000 cycles showing a high retention of ~84%. The first cycle and the last cycle are shown as an inset confirming minimal changes (reprinted with permission from Wiley, copyright © 2023).[237] (d) $Ti_3C_2T_x$ MQD/LRG laser fabrication process, image of exfoliated materials, SEM (scale bar, 20 nm) confirming size distribution below 5 nm (reprinted with permission from Wiley, copyright © 2022).[236]

matrix to create a heterodimensional hybrid structure (0D/2D) through a microwave hydrothermal method that altered charge storage behavior. Electrochemical impedance spectroscopy (EIS) indicated that the ohmic resistance (1.439 Ω) and charge transfer resistance (0.04078 Ω) of MQD/MXene nanosheet electrodes are smaller than those of $Ti_3C_2T_x$ nanosheets electrodes (R_s = 1.637 Ω, R_{ct} = 0.10032 Ω). An areal capacitance of 2202 mF cm^{-2} at 3 mA cm^{-2} was attained, which significantly outperformed conventional MXene-based electrodes. The material retained 84% of its capacity after 10 000 cycles and delivered an aerial energy density of 90.33 μWh cm^{-2} at a power density of 450 mW cm^{-2}. No efficiency loss due to mechanical deformations was also noticed, highlighting their high flexibility and robust mechanical stability (Fig. 16c).[137,236]

Beyond flexibility and mechanical properties, supercapacitors have long struggled with the trade-off between capacitance and stability.[240] Despite the high theoretical capacitance of various classes of active materials, most of the structures suffer from low utilization of active sites due to limited electron mobility.[241] Recently, J. Wang *et al.*[205] have demonstrated that by incorporating $Ti_3C_2T_x$-MQDs through a microwave-assisted DMF exfoliation process, the $Ni(OH)_2$ structure undergoes a remarkable transformation. As a result, a higher electroactive surface area, higher ion diffusion rate, and significantly improved charge transport efficiency are attained. The MQD-NH electrode on nickel foam offers a record-high specific capacitance of 1660 F g^{-1} at 1 A g^{-1} in 2 M KOH, far surpassing conventional $Ni(OH)_2$ composites such as $Ni(OH)_2$/rGO (802 F g^{-1}) and $Ni(OH)_2$ (1087.1 F g^{-1}).[205]

5.3.2. Energy conversion devices. Owing to exceptional electronics and surface properties of MQDs, their utility has been demonstrated across a diverse range of applications, such as energy conversion systems. In this section, we will go over research highlights on improving efficiency of MQDs as electrocatalysts.

- **CO_2 reduction reaction**

Electrochemical conversion can serve future energy demands by storing renewable energy and reducing anthropogenic emissions such as CO_2. For this aim, photocatalysis has long been regarded as a promising technology for tackling environmental pollution and converting CO_2 into valuable fuels.[242] Among many photocatalytic materials, g-C_3N_4 stands out for its stability, non-toxicity, and visible-light activity. Yet, despite its potential, a persistent challenge is its tendency to lose charge carriers too quickly before they can drive meaningful chemical reactions. Among different methods to improve the efficiency of CO_2 reduction electrodes, strategies such as reducing the activation energy of CO_2 redox reactions,[243] introducing novel electrocatalysts to enhance selectivity for CO_2 reduction,[244] and minimizing parasitic reactions like HER[245] have been reported in literature.[242] One recent approach is the formation of heterojunctions with bismuth oxyiodide (BiOI), a p-type semiconductor known for its strong light absorption and complementary band structure.[246] While this combination does improve charge separation to some extent, it still lacks the efficiency needed for high-performance photocatalysis. The real challenge is not just preventing recombination but actively driving charge migration to ensure efficient and prolonged reaction activity. To improve charge separation, a heterojunction of g-C_3N_4 with BiOI has recently been investigated.[247] Although this combination enhances charge transfer to some extent, it remains insufficient for achieving optimal performance. The missing piece in this system is a mechanism to accelerate charge migration and suppress recombination more efficiently.[247]

Another strategy to accelerate CO_2 conversion is decreasing the activation energy of reaction. As an example, $Ti_3C_2T_x$-MQD heterostructure with g-C_3N_4/BiOI enhances the CO_2 photoreduction properties of the device.[247] While the absorption band edge of g-C_3N_4 shows a strong UV absorption and BiOI displays a broad UV to visible light absorption, modifying with the MQDs will tune the bandgap, and extend the photo-response to NIR range (Fig. 17a). The CN/MQDs/BOI offers an observable photocurrent response of 2.3 μA and a CO production rate of 57.8 μmol g^{-1} h^{-1}, which is more than 30 times higher than C_3N_4/TiO_2. The g-C_3N_4/MQDs/BOI exhibits a Nyquist semicircle, confirming enhanced charge transfer efficiency.

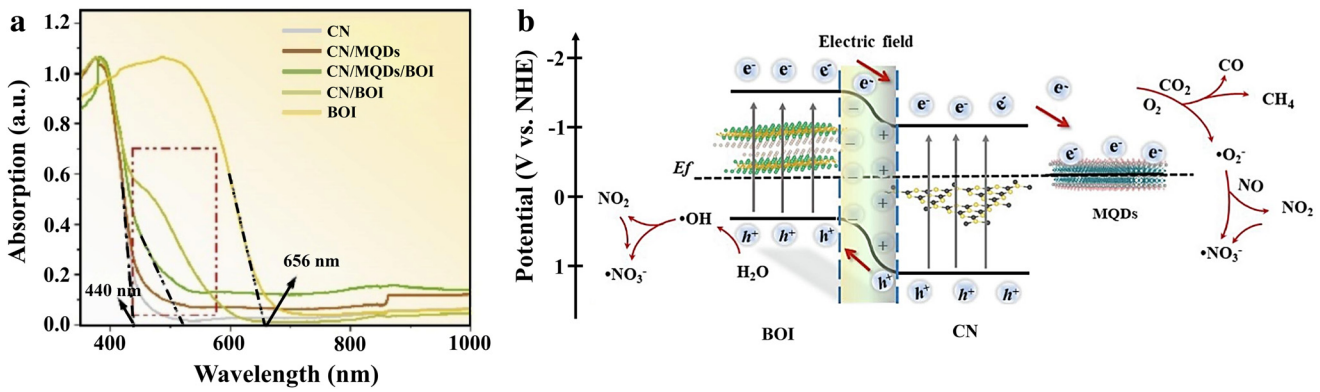

Fig. 17 (a) UV–vis diffuse reflectance absorption spectra of CN/MQDs/BOI confirming the effectiveness of hybrid structure to tune adsorption edge at 440 nm for CN/MQDs and ~520 nm for CN/MQDs/BOI (reprinted with permission from Elsevier, copyright © 2025).[247] (b) Schematic of the reactions based on potential *vs.* NHE (reprinted with permission from Elsevier, copyright © 2025).[247]

However, it is noteworthy that NO_x reduction is susceptible to occur during the reduction reaction process, which affects CO_2 reduction yield and the corresponding production of CO and CH_4 (Fig. 17b).[247]

While metal chalcogenides, such as Bi_2S_3, have shown potential for CO_2 reduction due to their narrow bandgap and strong visible-light absorption, their efficiency is compromised by rapid recombination of carriers and insufficient adsorption sites for CO_2.[248] To address these issues, 3D porous Ti_3C_2-MQDs-OH/Bi_2S_3 structure that leverages the synergy between protonated Bi_2S_3, and alkalized MQDs (MQDs-OH) were investigated for CO_2 reduction.[249] The strong electron-withdrawing properties and abundant hydroxyl functional groups of MQDs-OH led to efficient charge carriers' separation and retarded recombination, as evidenced by EIS. PL and photocurrent response measurements determined a high photocurrent density of 22 μA with 15-fold enhancement in the CO_2 adsorption capacity, *i.e.*, from 1.6 mg CO_2 per g for pristine Bi_2S_3 to 23.0 mg CO_2 per g for MQDs-OH/Bi_2S_3. This massive improvement resulted in a record-high methanol yield of 694.7 μmol g^{-1}, more than double the output of unmodified Bi_2S_3-based catalysts (321.8 μmol g^{-1}). The electron spin resonance (ESR) measurements showed a significant increase in ROS ($O_2^{\bullet-}$) generation, affirming that the presence of MQDs enhanced the activation of CO_2 molecules for more efficient reduction reactions.[249]

- **Hydrogen evolution reaction**

The generation of hydrogen from H_2O through semiconductor photocatalysis has garnered significant attention in recent years.[250] Among various photocatalysts, conventional TiO_2/g-C_3N_4 composites without MQDs have found of great interest for photocatalytic hydrogen evolution.[251] It is noteworthy that the catalytic activity of TiO_2/g-C_3N_4 heterostructures is constrained by rapid charge carrier recombination and limited active sites. While the S-scheme heterostructure of TiO_2/g-C_3N_4 provides a foundation for improved charge separation, it is still not enough to sustain high reaction rates.[145] The modification of S-scheme TiO_2/g-C_3N_4 heterojunction with Ti_3C_2 MQDs is considered as an effective strategy for extending optical absorption into the visible range. Diffuse reflectance spectroscopy (DRS) measurements determine the bandgap energy of TiO_2 (T), g-C_3N_4 (CN), TiO_2/g-C_3N_4 (T-CN), and TiO_2/g-C_3N_4/Ti_3C_2 QDs (T-CN-TCQD) as 3.22 eV, 2.86 eV, 2.57 eV, and 2.45 eV, respectively (Fig. 18a). By serving as electron acceptors and facilitating charge separation, the MQDs address the critical challenge of rapid recombination of photoinduced carriers in g-C_3N_4, resulting in a hydrogen production rate of 5111.8 μmol g^{-1} h^{-1}, which is nearly 26 times higher than pristine g-C_3N_4 nanosheets (196.8 μmol g^{-1} h^{-1}), 3 times higher than Pt/g-C_3N_4 (1896.4 μmol g^{-1} h^{-1}), and 10 times higher than Ti_3C_2 MXene sheet/g-C_3N_4 (524.3 μmol g^{-1} h^{-1}). This drastic improvement is attributed to the superior

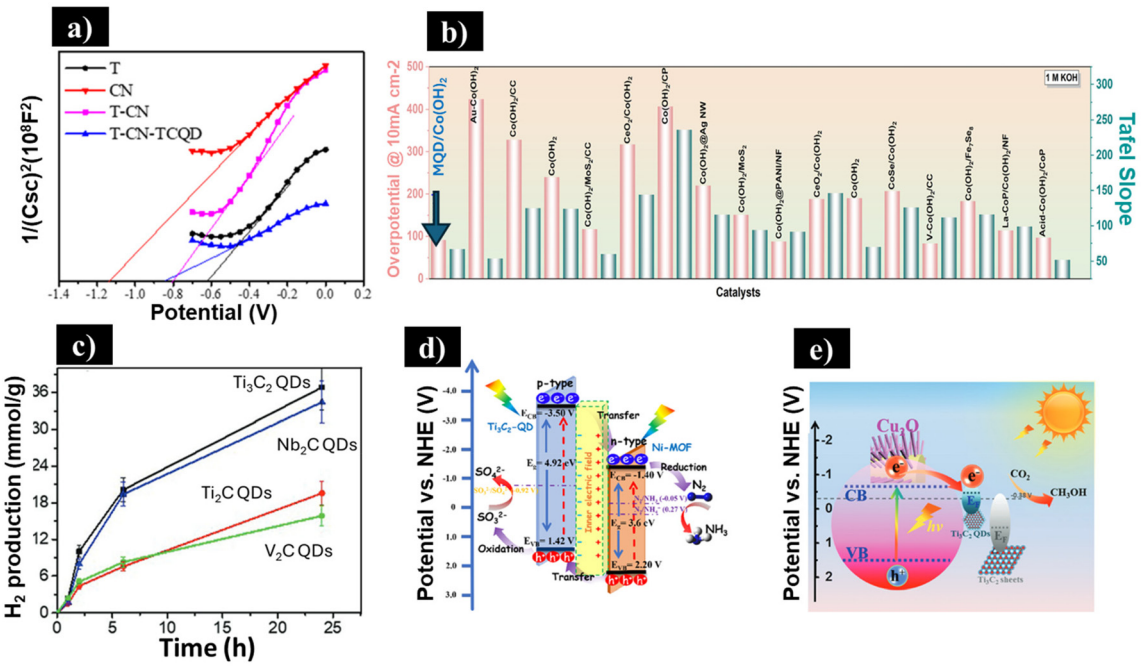

Fig. 18 (a) Flat-band potential (E_{fb}) estimated by Mott–Schottky curve obtained from DRS test showing the extended bandgap energy of g-C_3N_4@Ti_3C_2 MQDs have been expanded to visible region compared to other candidates without MQDs (reprinted with permission from American Chemical Society, copyright © 2019).[142] (b) The Tafel slope and overpotential of $Co(OH)_2$-based catalysts at 10 mA cm^{-2} for HER in an alkaline 1 M KOH solution (reprinted with permission from Elsevier, copyright © 2025).[141] (c) H_2 evolution reaction as a function of time for (■) Ti_3C_2 QDs; (▼) Nb_2C QDs; (●) Ti_2C QDs; and (◊) V_2C MQDs (reprinted with permission from Wiley, copyright © 2023).[252] (d) Energy band positions of Ti_3C_2-MQD/Ni-MOF (reprinted with permission from American Chemical Society, copyright © 2020).[4] (e) Energy level diagram of Ti_3C_2 MQDs/Cu_2O NWs/Cu and Ti_3C_2 sheets/Cu_2O NWs/Cu heterostructure (reprinted with permission from Wiley, copyright © 2018).[145]

electronic conductivity of Ti_3C_2 MQDs, which not only facilitated efficient carrier transfer but also increased the specific surface area of g-C_3N_4 from 27.575 $m^2\ g^{-1}$ to 40.149 $m^2\ g^{-1}$. Time-resolved photoluminescence measurements indicate a longer lifetime, *i.e.*, 10.1242 μs for g-C_3N_4@Ti_3C_2 QDs compared to 9.6841 μs for g-C_3N_4. The enhanced photocurrent response of g-C_3N_4@Ti_3C_2 QDs, along with a reduced EIS arc radius compared to pristine g-C_3N_4, further demonstrate the superior charge transport and separation efficiency introduced by MQDs.[145]

Hydrogen evolution reaction (HER) efficiency also depends on the H^+ reduction barriers. M. Y. Solangi *et al.*[253] demonstrated that an assembly of $Co(OH)_2$ and Ti_2C MQDs, accelerated the adsorption of H_2O and decreased the reduction barrier for H^+. The presence of $Co(OH)_2$ provided active sites for hydroxyl (OH) adsorption, while Co sites with electron-deficiency protected the $Co(OH)_2$ from deteriorating under alkaline environment. The MQD introduction reduced the overall energy from −251.29 to −672.51 eV, while enhancing the structural stability of $Co(OH)_2$. The Gibbs free energy of water dissociation was also substantially decreased from 1.52 to 0.14 eV by the incorporation of MQDs. Additionally, a low overpotential of 91 mV at the current density of 10 mA cm^{-2}, which surpasses the performance of the CF (344 mV), Pt/C (111 mV), and the $Co_2(OH)_3Cl$/CF-R (268 mV) catalysts, was noticed (Fig. 18b).[253]

By utilizing HF-free laser ablation in an aqueous medium, not only can the need for HF be eliminated but also control over quantum confinement effects, surface functionalization, and bandgap modulation can be adopted. For instance, significantly enhanced photocatalytic performance of Ti_3C_2-MQDs for HER has been reported by this technique.[252] Here, a hydrogen production rate of 2.02 mmol $g^{-1}\ h^{-1}$, which is comparable to noble-metal-based catalysts like Pt/g-C_3N_4 (2.5 mmol $g^{-1}\ h^{-1}$), has been reported (Fig. 18c). It has been shown that not only fine-tuning of the valence band (VB) and conduction band (CB) positions can achieved by laser ablation,[254] but also the oxygenated surface terminations (OH, and O) can improve stability and catalytic activity of MQDs.[252]

- **NO_x reduction**

NO_x reduction is critical for environmental protection because it aims to convert hazardous materials to value added products, while reducing nitrogen oxide emissions from industrial processes. However, the large bond energy (940.95 kJ mol^{-1}) of the nitrogen–nitrogen bond makes the nitrogen reduction reaction (NRR) difficult.[255] Thus far different approaches, such as electrolyte engineering,[256] crystallographic phase transformation engineering,[257] transition metal dual-atom catalysts,[258] transition metal oxides,[259] covalent/metal organic frameworks, perovskite oxides, doping with transition metals to hybridizing with carbon-based materials like graphene,[260] and incorporation of MQDs as a co-catalyst to tune NRR activity have been investigated.[261] Among various methods to develop efficient and selective electrocatalysts, utilization of MQDs with different surface terminations have found of interest in nitrogen reduction to produce ammonia at room temperature.[262,263] MQDs provide high density of edge sites, which are more catalytically active than basal planes, thus enhancing the adsorption and activation of nitrogenous molecules. Additionally, the surface chemistry of MQDs can be tailored with functional groups such as hydroxyl, or fluorine, optimizing their electronic structure and adsorption characteristics to lower energy barriers for nitrogen reduction.[143] For instance, J. Qin *et al.*[4] demonstrated that incorporating surface-functionalized Ti_3C_2 MQDs to Ni-MOF led to photocatalytic NH_3 production rate of 88.79 μmol $g^{-1}\ h^{-1}$, which was more than four times higher than pristine Ni-MOF (21.39 μmol $g^{-1}\ h^{-1}$).[139,264] EIS indicated a low charge transfer resistance for the coupled structure, while transient PL decay determined an extended carrier lifetime of 5.636 ns, compared to 2.685 ns for the pristine Ni-MOF. DFT calculations also affirmed that the MQD incorporation decreased the free-energy barrier for N_2 activation, making the reaction more energetically favorable. Specifically, the initial N_2 adsorption step becomes exothermic, releasing 0.74 eV, while the N≡N bond elongated from 1.098 Å to 1.118 Å, facilitating subsequent reduction steps. Details of the heterostructure and reaction mechanism, shown in Fig. 18d, proposed that the synergistic MQD–MOF system altered the reaction pathway, making nitrogen fixation significantly more efficient.[4]

Another product of nitrogen containing compounds reduction is ammonia which is mostly obtained from NORR using copper-based electrocatalysts.[143] Ti_3C_2 MQDs have been proven to effectively boost the co-catalytic performance of NORR ammonia production performance of copper nanowires (Cu NWs).[143] An NH_3 yield of 5346.3 μg $h^{-1}\ mg^{-1}$ and FE of 95.5%, which are much higher than those of unmodified Cu NWs (NH_3 yield of 3313.1 μg $h^{-1}\ mg^{-1}$ and FE of 89.5%) have been reported (Fig. 19a). The onset potential of reaction (−0.4 V *vs.* reversible hydrogen electrode (RHE)) is also significantly less than that of Cu foam (−0.9 V *vs.* RHE). A record-high NH_3 yield, outperforming many well-performing catalysts previously reported in the literature like MoS_2,[139] MoC,[265] Bi/C,[266] and Ni_2P nanosheet array on carbon paper (Ni_2P/CP),[267,268] have been demonstrated. An assembled Zn–NO battery with Ti_3C_2 MQDs/Cu NWs offers a power density of 3.03 mW cm^{-2} and a high NH_3 yield of 925.2 μg $h^{-1}\ mg^{-1}$.[143]

- **Photocatalyst**

Copper oxide nanowires with p-type semiconductor properties and favorable band structure have been considered promising photocatalyst. Traditional approaches, such as integrating carbon nanomaterials,[270] noble metals,[271] and other semiconductors,[272,273] have yielded only limited improvements on charge recombination without making the fabrication processes complex with reduced costs.[145] Recent studies have demonstrated that MQDs can serve as electron shuttles to accelerate charge transport, while suppress recombination losses.[145] For instance, by integrating Ti_3C_2 MQDs onto Cu_2O nanowires (NWs), photocatalytic CO_2 conversion results in a high rate of methanol production (153.38 ppm cm^{-2}), which is 8.25 times higher than pristine Cu_2O NWs (18.58 ppm cm^{-2}) and 2.15 times higher than Ti_3C_2 nanosheets/Cu_2O NWs

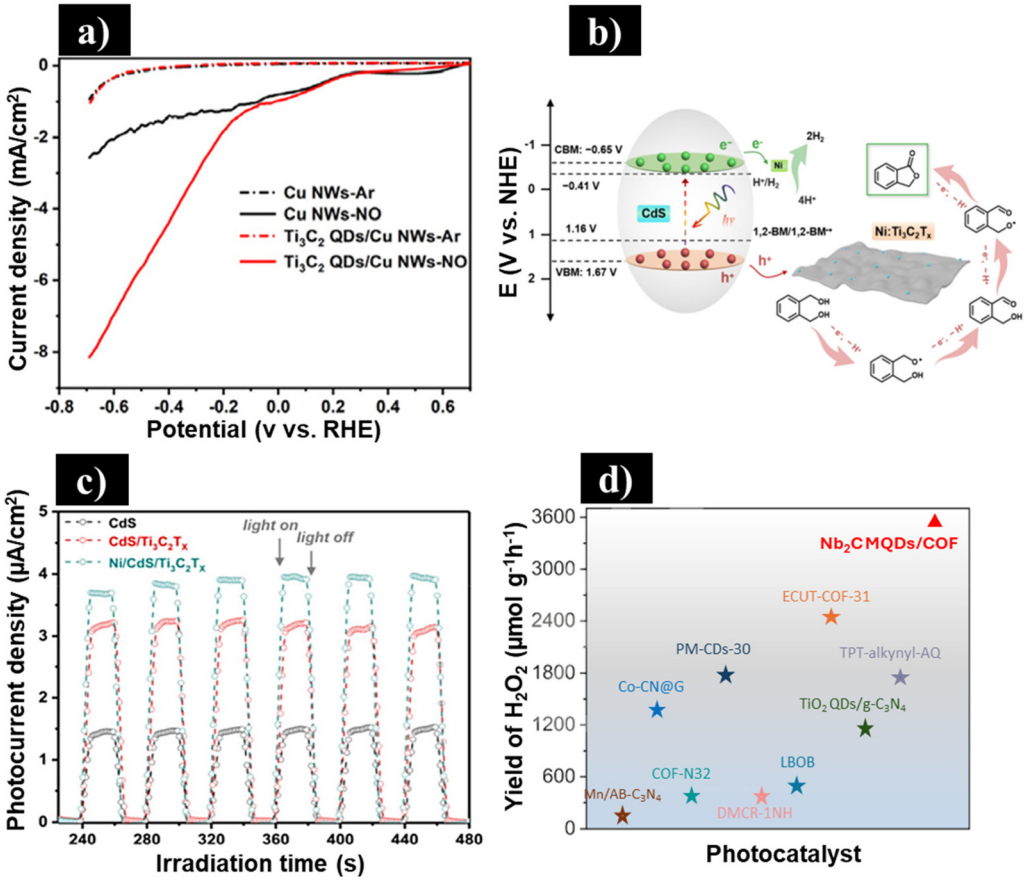

Fig. 19 (a) Linear Sweep Voltammetry (LSV) of Cu NWs and Ti_3C_2 MQDs/Cu NWs in Ar-saturated and NO-saturated 0.1 M K_2SO_4 exhibiting a high activity of MQDs modified Cu nanowires toward NO reduction (reprinted with the permission of Royal Society of Chemistry, copyright © 2023).[143] (b) The proposed reaction mechanism for photocatalytic phthalide synthesis and H_2 evolution by MQDs incorporation and electronic structure modification as a successful strategy to boost reactivity (reprinted with the permission of American Chemical Society, copyright © 2024).[269] (c) Photocurrent *vs.* irradiation time for CdS, CdS/$Ti_3C_2T_x$, and Ni/CdS/$Ti_3C_2T_x$ photocatalysts (reprinted with the permission of American Chemical Society, copyright © 2024).[269] (d) H_2O_2 yield for Nb_2C MQDs/COF as compared to other photocatalysts, demonstrating the promising potential of MQDs to modulate the H_2O_2 production (reprinted with the permission of Elsevier, copyright © 2025).[147]

(71.39 ppm cm^{-2}).[145] Mott–Schottky analysis reveals that carrier density (N_D) increases dramatically from 1.09×10^{19} cm^{-3} in Cu_2O NWs to 2.75×10^{19} cm^{-3} in MQD-modified Cu_2O NWs, with prolonging photocarrier lifetimes. Additionally, DRS demonstrates significantly enhanced light absorption efficiency and shifts the bandgap from 2.2 eV (Cu_2O) to 2.02 eV (Ti_3C_2 MQDs/Cu_2O NWs) (Fig. 18e). This bandgap engineering facilitates a broader spectrum of light absorption and reduces the charge transfer resistance, as evidenced by EIS. Photostability studies of Ti_3C_2 MQDs/Cu_2O NWs/Cu over a wide range of potential also affirm the potential of the MQDs to prevent Cu_2O NWs from oxidation.[145]

- **Radical scavengers**

Radical scavenging plays a pivotal role in mitigating oxidative stress and preserving functional electrode stability and preventing electrode degradation,[274] stabilizing intermediates in reactions like ORR/CO_2RR.[275,276] Benefiting from a large surface-to-volume ratio, Cl, N-doped Ti_3C_2 MQDs (D = ~3.4 nm) synthesized *via* electrochemical etching demonstrated outstanding hydroxyl ($^{\bullet}OH$) radical scavenging activity (93.3%) at a concentration of 12.5 μg mL^{-1}, surpassing the performance of previously reported graphene-based nanoparticles.[277] The scavenging mechanism is attributed to the electron transfer ability of the Ti_3C_2 structure and the electron donation of the double dopants.[75] In another study, nitrogen-doped Ti_3C_2 MQDs synthesized by a hydrothermal method exhibited exceptional scavenging capability against multiple ROS, including $^{\bullet}OH$, $^1O_2$ (singlet oxygen), and $O_2^{\bullet-}$ (superoxide anion) multi-ROS scavenging capabilities, achieving a hydroxyl radical scavenging efficiency of 93.2% at a concentration of 12.5 μg mL^{-1}, significantly outperforming graphene oxide (37.3%), and graphene QDs (53.3%) under comparable conditions. Detailed DFT simulations and voltammetry measurements revealed that nitrogen doping not only enhanced the electron density and created additional active sites but also dramatically strengthened the adsorption and charge-transfer processes with OH radical species, thereby underpinning the superior antioxidative activity of the N-Ti_3C_2 MQDs.[118]

• **Oxidation of alcohols**

Semiconductor photocatalysts often face the challenge of photoinduced decomposition, which hampers their efficiency and stability in selective oxidation of alcohols.[278] To address this issue, recent studies have developed a robust photocatalyst by integrating nickel-decorated cadmium sulfide quantum dots (Ni/CdS QDs) with $Ti_3C_2T_x$ MXene.[269] This composite leverages the high conductivity and unique surface chemistry of $Ti_3C_2T_x$ MXene to enhance charge separation and transfer, while the Ni decoration provides active sites that facilitate the oxidation process. This strategic combination not only mitigates the phot-corrosion of CdS but also significantly improves the efficiency and selectivity of alcohol oxidation reactions under visible light irradiation.[269] Lactonization of 1,2-benzenedimethanol (1,2-BM) to phthalide is also integrated with concomitant H_2 production, as Ni clusters in CdS accelerates H_2 evolution (Fig. 19b). The anchored Ni as a single atom on $Ti_3C_2T_x$ can also influence efficient adsorption and cyclization of diols. This composite material exhibits remarkably enhanced activity for lactone synthesis, which is 80.4 times higher than that of blank CdS, along with excellent selectivity of 91.6% for composite structure (Ni/CdS QDs) although blank CdS QDs had a much lower selectivity of only 48.4% under the same reaction conditions. While the blank CdS shows a significant decrease (43.6%) in the phthalide production after four repeated trials, no obvious deactivation phenomenon of phthalide and H_2 production could be observed over Ni/CdS/Ti_3C_2T MQDs. The transient photocurrent response of the samples increases in the following order: Ni/CdS/$Ti_3C_2T_x$ > CdS/$Ti_3C_2T_x$ > CdS, suggesting the higher charge separation efficiency in Ni/CdS/$Ti_3C_2T_x$ composite (Fig. 19c).[269]

• **H_2O_2 production reaction**

Pyrene-based covalent organic frameworks (COFs) hold significant promise in photocatalytic applications; however, their practical use in hydrogen peroxide (H_2O_2) production is hindered by low charge-generation and charge-transfer efficiencies, as well as rapid charge recombination rate.[208,279] To address these challenges, recent research has focused on integrating MQDs as active sites within pyrene-based COFs through a self-assembly method.[147] This strategic combination enhances photocatalytic performance by improving charge separation and transfer, thereby facilitating efficient H_2O_2 photosynthesis from abundant seawater resources.[147] For instance, a H_2O_2 production rate of 3560 μmol g^{-1} h^{-1} was reported by integration of Nb_2C MQDs into high-crystalline COF structure.[147] An AQY of 12.8% at 400 nm together with SCC (Solar-to-Chemical Conversion) efficiency of 0.27% was also reported (Fig. 19d). From the mechanistic point of view, femtosecond transient absorption spectroscopy (fs-TAS) determined electronic coupling between Nb_2C MQDs and COF. Further supported by DFT simulations of the planar-averaged charge density difference along with Z direction it was proposed that the electrons mainly transferred from COF to Nb_2C MQDs through intermediates governed by a strong electron–phonon coupling at the interface, which promotes directional charge migration over thermal relaxation. This process is further amplified by the significant spin–orbit coupling of the heavy Nb atoms, which modifies the electronic band structure to favor rapid carrier extraction at the MQD active sites and corresponding free energy changes.[147,280]

5.4. Biomedical applications

5.4.1. Immunomodulation. • *In vitro* assays

Transplantation immunology is critically important as it addresses the complex interplay between the immune system and transplanted tissues, biomaterials, and cells determining the success and safety of organ transplantation.[281] Graft rejection occurs when the recipient's immune system recognizes the transplanted organ as foreign and begins the expansion of effector immune cells and inflammation.[281] Inflammation, vital for the body's response to injury and infection to maintain the physiological balance, hinders the clinical use of tissue therapies in regenerative medicine by causing the rejection of transplanted biomaterials and stem cells.[282,283] Since a number of studies have indicated that transplanted tissue constructs frequently trigger pronounced proinflammatory responses leading to rejection, it is needed to control this response to realize the advantages of allografts.[284]

MQDs with anti-inflammatory properties can be applied for immunomodulation. As an example, Ti_3C_2 MQDs with intrinsic immunomodulatory properties were shown to decrease human $CD4^+$ IFN-γ^+ T-lymphocytes activation by about 20%.[284] The QDs also encouraged a 3% increase in the proliferation of immunosuppressive $CD4^+$ $CD25^+$ $FoxP_3^+$ regulatory T-cells within a stimulated lymphocyte population. Human naïve $CD4^+$ T-lymphocytes were activated and turned into proinflammatory Th1 cells over 7 days with and without Ti_3C_2 MQDs. Flow cytometry indicated decreased expression of lymphocyte proliferation and upregulation of the regulatory T-cells. The mechanism behind the immunomodulatory effects of these MQDs is still not well-understood.[51] On the other hand, Szuplewska *et al.*[53] have proposed that the ROS produced by $Ti_3C_2T_x$ MXenes induces the release of proinflammatory cytokines from resident tissue macrophages and interferes with anti-inflammatory and immunomodulatory properties of implanted biomaterials in the body.[21]

Rafieerad *et al.*[24] have studied the immunomodulatory mechanism of $Ta_4C_3T_x$ MQDs by activated HUVECs, human peripheral blood mononuclear cells, and Th1 cells. Activated HUVECs, PBMCs, and Th1 cells were selected as they represent key mediators of immune responses. Endothelial cells function as antigen-presenting cells during transplant rejection, PBMCs comprise essential immune effectors, and Th1 cells play a central role in proinflammatory responses and allograft rejection.[285,286] A 3.3-fold increase in the PD-L1 expression and a simultaneous 1.3-fold decrease in the CD86 expression in activated HUVECs treated with $Ta_4C_3T_x$.[287] MQDs can elucidate the immunomodulatory mechanism of these MQDs. Both PD-L1 and CD86 play important roles in T-cell activation *via* antigen-presenting cells. PD-L1 inhibits T-cell activation, while CD86 activates it.[288] $Ta_4C_3T_x$ MQDs hold the potential to diminish host inflammation against allogeneic organs and

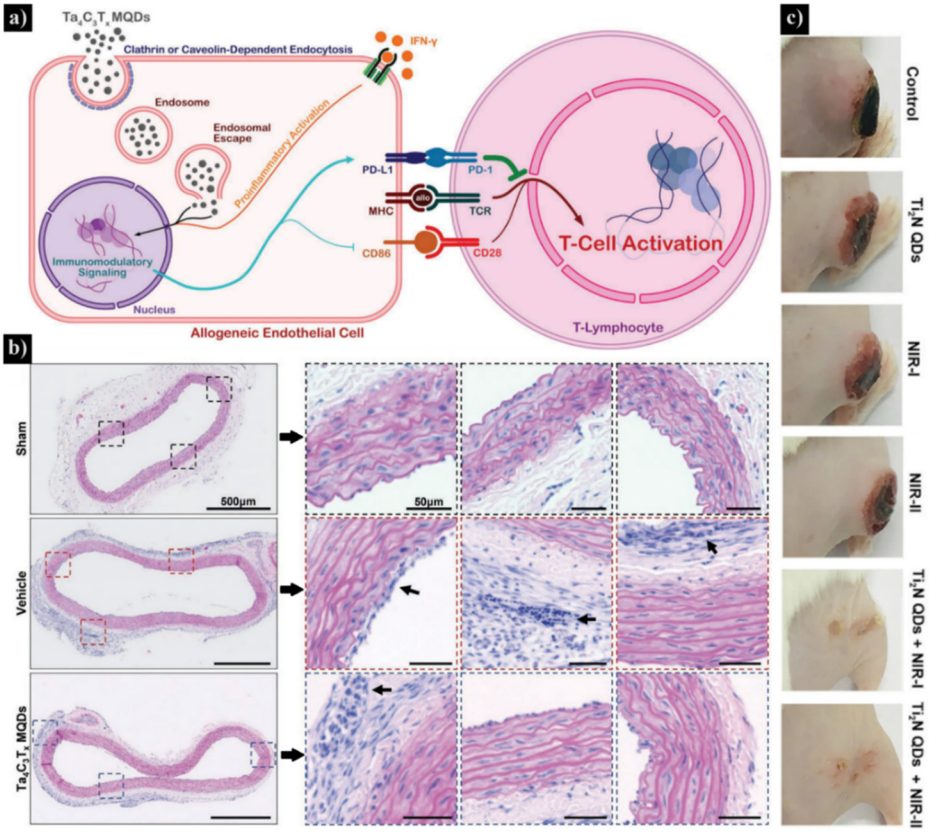

Fig. 20 (a) Schematic representation of the immunomodulatory mechanisms of $Ta_4C_3T_x$ MQDs. (b) H&E-staining of explanted abdominal aortic segments (reprinted with permission from Wiley, copyright © 2021).[24] (c) Typical photographs of 4T1 tumor-bearing mice and tumors after different treatments for 16 days (reprinted with permission from Elsevier, copyright © 2020).[23]

tissues by modifying the PD-L1 and CD86 equilibrium within antigen-presenting endothelial cells (Fig. 20a).[24]

- ***In vivo* immunomodulation**

To investigate the immunomodulatory potential of $Ta_4C_3T_x$ MQDs within a living organism, Rafieerad *et al.*[287] utilized a rat model of allograft vasculopathy, which is a significant factor in the rejection of transplanted organs.[289] Following transplantation, $Ta_4C_3T_x$ MQDs were promptly administered at a specific dose. No adverse effects were observed either over the course of a week or after that in blood and tissue samples. However, histologic examination of the abdominal aorta in transplanted animals revealed apparent inflammatory changes compared to sham animals (Fig. 20b). Nevertheless, animals treated with $Ta_4C_3T_x$ MQDs showed reduced endothelial injury and immune cell infiltration when compared to those injected with saline, while both were different from control animals. Immunohistochemistry, flow cytometric analysis also revealed a decrease in alpha-smooth muscle actin to assess vascular injury. This protein is an early contributor to rejection.[290] This reduction was ameliorated in animals treated with $Ta_4C_3T_x$ MQDs. Tregs, which play a crucial role in immunologic tolerance after transplantation,[291] were reduced in transplanted animals but restored by $Ta_4C_3T_x$ MQD treatment. The results of the *in vivo* examinations revealed the potential of $Ta_4C_3T_x$ MQDs in reducing allograft vasculopathy and improving transplantation outcomes.[287]

5.4.2. Bioimaging. Overcoming the challenge of nanoparticle uptake from the bloodstream to the target site is a significant hurdle in the systemic delivery of subcellular nanomedicine. Vascular ECs, which act as a barrier between the blood and organs, facilitate the uptake of engineered nanoparticles.[288] Recently, fluorescent Ti_3C_2 MQDs with tailored surface modifications were used for clinical subcellular nanomedicine.[10] It was shown that a low concentration of the Ti-based MQDs (2–20 μg ml^{-1}) were efficiently taken up by live HUVECs in a dose-dependent manner. No significant alterations in cellular morphology or behavior over the course of the study was noticed.[10]

Recent studies have expanded the range of MQDs applied in bioimaging beyond conventional Ti_3C_2 composition. For example, niobium carbide (Nb_2C) MQDs have attracted particular attention owing to their bright fluorescence and excellent biocompatibility. Notably, at concentrations as high as 100 μg mL^{-1}, levels that are cytotoxic to Ti_3C_2 QDs, Nb_2C MQDs exhibited no detectable toxicity toward HUVEC cells and even induced protective autophagy, highlighting their superior biological tolerance.[292] Likewise, albumin-stabilized Ti_3C_2 MQDs have been engineered for targeted imaging of

MDA-MB-231 breast cancer cells, producing strong and stable intracellular fluorescence signals *in vitro*.[293]

The structural versatility of MXene-based hybrid nanostructures further highlights their potential for advanced imaging applications. For example, Co–Mn Prussian-blue nanoparticles functionalized with Ti_3C_2 MQDs enabled *in situ* fluorescence sensing and spatial mapping of specific microRNAs within living cancer cells.[294] Collectively, these studies underscore that rationally engineered MQDs, particularly those derived from non-Ti compositions, can serve as bright, stable, and biocompatible nanofluorophores suitable for live-cell imaging with minimal cytotoxicity. Overall, MQDs represent a newly emerging and promising material class of bioimaging materials. However, further research is required to achieve a deeper understanding of their behavior and potential in bioimaging.

5.4.3. Cancer therapy. Although research on 2D nanomaterial has led to the development of new PTT agents, potential long-term toxicity risks have emerged biodegradable QDs with satisfactory photothermal properties.[10] Titanium-based MQDs, such as Ti_2N, have demonstrated great potential in this field by offering an effective platform for photoacoustic (PA) imaging – PTT within the NIR-I/II biowindows for cancer treatment.[21] Ti_2N MQDs exhibit strong and broad NIR-I, and NIR-II absorption, achieving temperatures of around 60 °C with low concentrations (20 ppm) under 808 or 1064 nm laser irradiation. Their photothermal conversion efficiency (η) reaches as high as 48.62% and 45.51% for 808 and 1064 nm, surpassing conventional inorganic PTT agents, such as Au nanorods (21%), graphene oxide (25%), MoS_2 nanoflakes (27.6%), black phosphorus QDs (28.4%), and Bi_2Se_3 nanosheets (26.4%).[291,295] Ti_2N QDs maintain their photothermal properties over five lasers on/off cycles, and their morphology and structure remain unchanged indicating excellent photothermal stability. However, Ti_2N MQDs exhibit notable degradability in aqueous solution through oxidation and hydration processes, forming titanium oxide and hydrogen titanium oxide byproducts. Shao *et al.*[23] used Ti_2N MQDs in an *in vivo* setting, as PTT agents within the NIR-I/II windows. In an animal model, NIR laser irradiation resulted in a significant increase in temperature, effectively ablating the tumor tissues (Fig. 20c). Continuous monitoring of the animals revealed no significant weight loss or adverse effects, highlighting the negligible side effects of the treatments without signs of recurrence. Besides Ti_2N MQDs, titanium carbide MQDs have been used for cancer therapy *via* incorporating Ti_3C_2 into a doxorubicin (DOX)-based prodrug system.[56] This system demonstrated targeted drug release, photodynamic effects, and bioimaging capabilities *in vitro*.[56] Overall, this remains an essentially untouched research area, and MXene quantum dots hold remarkable potential for future applications in cancer therapy.

5.4.4. Other applications. Apart from the above biomedical applications, magnetic luminescent QDs are being explored as potential nanotherapeutics against viral infections, as they offer heightened immune response in infectious diseases like COVID-19.[296] For instance, Ti_3C_2 MQDs enriched with bioactive functional groups have recently been used for testing SARS-CoV-2.[296] It has been found that the MQDs can effectively mitigate virus multiplication, even at very low doses (for example, 0.15 μg mL^{-1}) in VeroE6 cells.[296] In another study, Ta_4C_3 MQDs are suggested as nanocarrier to deliver sanguinarine (SAN) for enhanced antibacterial and wound healing. The SAN@AHEP@Ta_4C_3 formulation shows >85% antibacterial activity against *S. aureus* and *E. coli in vitro* and *in vivo* and, combined with NIR irradiation, demonstrated potential as a safe and effective antibacterial material.[297]

Some cations demonstrate effective reactivity with H_2O_2 within the specific acidic microenvironment of tumors.[298] An efficient generation of highly toxic $^{\bullet}OH$ leads to the destruction of tumor blood vessel integrity and causing cancer cell death. This process can be facilitated in the presence of MQDs. For example, it has been reported that Ti^{3+} in $Ti_3C_2T_x$ MQDs, or Mn^{2+} in a complex $Ti_3C_2T_x$-based system, effectively suppress HeLa tumor xenografts.[298] Due to the biocompatibility of $Ti_3C_2T_x$ MQDs, no side effects on normal tissues and organs have been observed, offering a safe and efficient strategy for tumor therapy.[298]

6. Conclusions and outlook

In this review, the emergence of MQDs as a promising class of nanomaterials for various applications is comprehensively discussed. To unlock their potential in advancing nanoscience and technology, recent progress in their synthesis, including strategies for quantum state engineering and surface passivation, has been reviewed. Through surface functionalization, doping, co-doping, and molecular conjugation, MQDs with high PLQY, exceeding ~28%, can successfully be synthesized. Taking advantage of intrinsic biocompatibility and exceptional optical properties, MQDs have been integrated into a wide range of applications, from sensing (various ions and molecules) and biomedicine (cancer therapy and cell imaging) to optoelectronics (LEDs, lasers, solar cells, and photonics). Their high surface area, layered structure, and abundant active sites male MQDs highly promising for applications in energy storage (batteries and supercapacitors) and energy conversion (hydrogen evolution and CO_2 reduction) systems.

Despite significant advancements in the properties of MQDs and their widespread applications, many promising opportunities remain unexplored, necessitating further comprehensive research. Some key areas for future perspectives are outlined below.

• Current fabrication methods suffer from low yields, temporal inefficiency, inconsistent quality, and high costs.[20] Scaling up production while maintaining uniformity in size, structure, and functionality remains a major challenge. One of the most recent techniques capable of synthesizing narrow-sized QDs from organic and inorganic semiconductors in a very short time scale (in less than hour) is pulsed laser ablation. This can be considered either top-down or bottom-up

based on the pulse time, forming ultrasmall QDs. Using various additives, doped or surface functionalized MQDs can be synthesized. Further, the possibility of the hot injection method, according to which organometallic reagents rapidly inject into a hot solvent and produce homogeneous nuclei,[299] that had been applied for other QDs, can be investigated for synthesizing MQDs.

• Regarding their optical properties, the precise contributions of quantum confinement (size-dependent behavior) and surface functional groups to enhanced radiative recombination by passivation of non-radiative trap states in MQDs are not yet clearly distinguished through in-depth investigation. To elucidate this, it is strongly recommended to combine DFT with PL, PLE, UV-Vis, and ultraviolet photoelectron spectroscopy to not only deepen interpretation about the electronic band structure but also find the excitation dependent or independent PL behavior of modified MQDs.[300]

• Heterojunctions have been capable of enhancing the sensing process. However, a few heterostructures based on MQDs and 2D structures have been fabricated. Transition metal dichalcogenides (TMDs) are chemically stable semiconductors showing ambipolar behavior.[301] Therefore, they can be a great career for transportation of the transferred electrons or holes between MQDs and analytes towards contacts, increasing the sensitivity. Moreover, decorated MQDs combined with tungsten disulfide (WS_2) or molybdenum disulfide (MoS_2) on a flexible polymer substrate (PTE) offer a potentially advantageous architecture for the development of future flexible wearable sensors.

• While the fabrication of single-component WLEDs and lasers based on MQDs has been demonstrated, their performances currently lag behind those achieved with lead-free perovskite QDs exhibiting PLQYs of 70%. Although surface-modified MQDs have reached PLQYs of about 30%, further enhancements *via* systematic investigations into the effects of size, dopant incorporation, and surface functionalization are necessary to compete with other materials.

• Given the recent significant advancements in PLQY enhancement through surface modification of MQDs, the absence, to our knowledge, of fabricated electroluminescent LED devices based on MQDs represents a notable research opportunity.

• MQDs have modified perovskite and ETL in solar cells, but their effects on hole transport layers like Spiro remain unexplored. Engineering the band structure of MQDs can be helpful to use it as a dopant or sensitizer for the conductivity improvement of Spiro-OMeTAD.

• MQDs show great promise in batteries, supercapacitors, and CO_2/N_2 reduction applications due to their high surface area, quantum confinement, and abundant edge sites.[302] A major challenge lies in controlling surface terminations, which strongly influence conductivity, ion intercalation, and long-term cycling stability. Current synthesis methods often yield a mixture of –O, –F, and –OH groups, limiting reproducibility and the ability to engineer their work function and surface catalytic energetics. Future strategies may include post-synthetic plasma treatments, thermal annealing in controlled environments, or selective chemical etching to achieve atomically precise surface control.

• While MQDs have shown promise in electrocatalytic systems such as Li–O_2 batteries, their application in intercalation-based batteries (*e.g.*, Li-ion, Na-ion) remains limited. The quantum-confined size of MQDs facilitates ion diffusion and access to active sites but falls short in practical performance. Current MQD-based electrodes reach only ~200 mA g^{-1} and fewer than 300 cycles, compared to >5000 mA g^{-1} and over 700 cycles in leading Li–air systems.[22] To bridge this gap, efforts should focus on embedding MQDs into conductive, porous frameworks to improve electron transport and accommodate discharge products. Stabilizing surface terminations, controlling aggregation, and designing efficient catalytic interfaces will be critical. Incorporating redox mediators or solid electrolytes may also lower the overpotentials and enhance the kinetics of reversibility and cycling life.[303,304]

• For photocatalytic and optical applications, most recent studies have focused on nanocomposites of MQDs with well-known catalysts such as TiO_2, Cu nanowires, and g-C_3N_4 to leverage interfacial charge-transfer mechanisms.[305] Future research should explore less conventional co-catalysts, such as conductive or semiconducting MOFs and COFs, to expand the functional landscape of MQD-based systems. In parallel, the intrinsic quantum confinement effects of MQDs, which can independently tune bandgap and electronic transitions, remain underexplored and should be systematically studied. A deeper understanding of how surface terminations modulate exciton dynamics and charge separation efficiency is also needed. Moreover, integrating plasmonic materials or defect-engineered semiconductors could induce plasmonic resonance energy transfer (PRET) or broaden the light-absorption cross-section.

• In energy conversion systems, stabilizing MQDs against aggregation and surface oxidation is critical for long-term electrode stability. This can be achieved through encapsulation in conductive matrices or by anchoring MQDs onto chemically compatible, high-surface-area supports such as carbonaceous materials or transition metal oxides. These strategies not only prevent degradation but also form ohmic contacts and reduce interfacial Schottky in charge transfer mechanistic. Additionally, operando spectroscopy and electrochemical impedance analysis should be used to monitor catalyst evolution and reveal degradation mechanisms. Long-term studies under realistic conditions, such as continuous electrolysis, variable gas concentrations, and pH, are still lacking.[69,306] Future research must address these gaps to better evaluate and increase the activation energy of degradation of MQD stability in real-world environments.

• Selectivity in electrocatalytic reactions involving MQDs has received less attention than in other nanomaterials. Altering the adsorption energetics of competing reaction intermediates and selectivity is essential to reduce energy consumption and lower the free energy barrier for the desired efficiency in processes like CO_2 and N_2 reduction. Approaches

such as heteroatom doping (*e.g.*, N, S, B), anchoring single-metal atoms, or constructing well-defined active sites could offer greater control over catalytic pathways. Tailoring surface terminations can also steer intermediate adsorption energetics. Modulating the structural and electronic properties of MQDs, through strain engineering or controlled synthesis, could further enhance charge carrier mobility and reaction specificity.[215] These directions require combined experimental and computational studies to uncover structure–property relationships.

Fig. 21 Schematics overview of challenges, solutions, and future directions for MQDs.

• Drug delivery is a key area of interest, particularly targeted smart drug delivery systems where drug-loaded QDs enter cell nuclei and release drugs for treatment.

• The intrinsic properties of MQDs, demonstrated *in vitro* and *in vivo*, require deeper investigation to understand underlying mechanisms.

• Research is needed to explore how functional groups influence reactive oxygen species generation to optimize medical applications. This could lead to innovative solutions in regenerative medicine and immune-related challenges, including transplantation.

• Fig. 21 gives a clear and comprehensive overview of the current progress and future directions of MQDs. It is organized into three main categories of synthesis, properties, and applications. Each part contains three sections of challenges, solutions, and outlook. This structure helps to show how different experimental methods and material designs influence MQD performance and practical applications. For example, it illustrates how controlling surface terminations can tune the photoluminescence behavior, or how adjusting synthesis routes can improve device stability and energy efficiency.

• In the synthesis section, the Fig. 21 compares several key approaches, including top-down etching, laser ablation, bottom-up solvothermal synthesis, and surface engineering. It summarizes their main issues including oxidation, size distribution, and low yield and lists the corresponding solutions and improvements like HF-free synthesis, heteroatom doping, and ligand passivation. The properties section highlights how these strategies affect MQD optical response, charge transport, surface stability, and energy-related performance. Finally, the applications section outlines how MQDs are being developed for optoelectronics, energy storage, biomedical imaging, and environmental sensing.

• Overall, the scheme serves not only as a summary but also as a roadmap that guides readers to the next stage of MQD research. The outlook column points out key opportunities for progress, including precise surface functionalization, hybrid material design, environmentally friendly scalable production, and cross-disciplinary integration into energy, environmental, and biomedical technologies. Through this structured format, the figure helps readers understand the current state of the field while also identifying the challenges and emerging directions that will shape future MQD development.

Conflicts of interest

The authors declare no competing financial interest.

Abbreviations

AA	Ascorbic acid
AFM	Atomic force microscopy
APTES	3-Aminopropyltriethoxysilane
AQY	Apparent quantum yield
ARS	Alizarin red S
ATP	Adenosine triphosphate
BAW	Bulk acoustic wave
BiOI	Bismuth oxyiodide
BSA	Bovine serum albumin
CE	Coulombic efficiency
CIE	Commission Internationale de l'Éclairage
COF	Covalent organic framework
CRI	Color rendering index
Cu NWs	Copper nanowires
CUR	Curcumin
CV	Cyclic voltammetry
DA	Dopamine
DFT	Density functional theory
DMSO	Dimethyl sulfoxide
DMF	Dimethylformamide
DOX	Doxorubicin
DPA	2,6-Dipicolinic acid
DRS	Diffuse reflectance spectroscopy
DSSCs	Dye-sensitized solar cells
ECL	Electrochemiluminescence
EDD	Electron density difference
EDTA	Ethylenediaminetetraacetic acid
EIS	Electrochemical impedance spectroscopy
ESR	Electron spin resonance
ETL	Electron transport layer
FE	Faradaic efficiency
FRET	Förster resonance energy transfer
FWHM	Full width at half maximum
GCE	Glassy carbon electrode
GIXRD	Grazing-incidence X-ray diffraction
GSH	Glutathione
HAADF-STEM	High-angle annular dark-field scanning transmission electron microscopy
HER	Hydrogen evolution reaction
HOMO	Highest occupied molecular orbital
HRP	Horseradish peroxidase
IFE	Inner filter effect
iPSCs	Induced pluripotent stem cells
ITO	Indium tin oxide
KOH	Potassium hydroxide
LiPSs	Lithium polysulfides
LOD	Limit of detection
LRGO	Laser-reduced graphene oxide
LUMO	Lowest unoccupied molecular orbital
LSV	Linear sweep voltammetry
MQDs	MXene quantum dots
MSCs	Mesenchymal stem cells
MTT	3-(4,5-Dimethyl-2-thiazolyl)-2,5-diphenyl-2*H*-tetrazolium bromide
MUC1	Mucin 1
NaF	Sodium fluoride
NDC	Nitrogen-doped carbon
NG	N-doped graphene
NMP	*N*-Methylpyrrolidone

NRR	Nitrogen reduction reaction
OER	Oxygen evolution reaction
OPD	*O*-Phenylenediamine
ORR	Oxygen reduction reaction
oxOPD	2,3-Diaminophenazine
PEC	Photoelectrochemical
PEDOT:PSS	Poly(3,4-ethylenedioxythiophene):polystyrene sulfonate
PEI	Polyethyleneimine
PET	Photoinduced electron transfer
PL	Photoluminescence
PLQY	Photoluminescence quantum yield
PLL	ε-Poly-L-lysine
PNK	Polynucleotide kinase
POSS-PQDs	Silsesquioxane-perovskite quantum dots
PQDs	Perovskite quantum dots
PSCs	Perovskite solar cells
PTT	Photothermal therapy
PVP	Polyvinylpyrrolidone
RHE	Reversible hydrogen electrode
RES	Reticuloendothelial system
RGB	Red, green, blue
RRS	Resonance Rayleigh scattering
ROS	Reactive oxygen species
SCC	Solar-to-chemical conversion
SCN^-	Thiocyanate
SEM	Scanning electron microscopy
SWV	Square wave voltammetry
TC	Tetracycline
TMAOH	Tetramethylammonium hydroxide
TMCs	Transition metal carbides
TNP	Trinitrophenol
TPAOH	Tetrapropylammonium hydroxide
UA	Uric acid
UV-vis	Ultraviolet-visible spectroscopy
VP	*Vibrio parahaemolyticus*
WLED	White light-emitting diode
XPS	X-ray photoelectron spectroscopy
ZAB	Zinc–air battery

Data availability

No primary research results, software or code have been included and no new data were generated or analysed as part of this review.

Supplementary information (SI) is available. See DOI: https://doi.org/10.1039/d5nr03616j.

References

1 W. Luo, H. Liu, X. Liu, L. Liu and W. Zhao, *Colloids Surf., B*, 2021, **201**, 111631.
2 X. Wang, X. Zhang, H. Cao and Y. Huang, *Microchem. J.*, 2022, **180**, 107629.
3 C. Guan, X. Yue, J. Fan and Q. Xiang, *Chin. J. Catal.*, 2022, **43**, 2484–2499.
4 J. Qin, B. Liu, K.-H. Lam, S. Song, X. Li and X. Hu, *ACS Sustainable Chem. Eng.*, 2020, **8**, 17791–17799.
5 S. Zhang, Z. Qi and Y. Li, *Ceram. Int.*, 2022, **48**, 21118–21124.
6 A. Kalkal, S. Kadian, S. Kumar, G. Manik, P. Sen, S. Kumar and G. Packirisamy, *Biosens. Bioelectron.*, 2022, **195**, 113620.
7 D. V. Tsyupka, Y. A. Podkolodnaya, E. A. Khudina, D. G. Koganova, O. A. Goryacheva, A. M. Abramova and I. Y. Goryacheva, *TrAC, Trends Anal. Chem.*, 2024, **177**, 117774.
8 Y. Zheng, Y. Wang, Z. Li, Z. Yuan, S. Guo, Z. Lou, W. Han, G. Shen and L. Wang, *Matter*, 2023, **6**, 506–520.
9 Q. Xu, W. Yang, Y. Wen, S. Liu, Z. Liu, W.-J. Ong and N. Li, *Appl. Mater. Today*, 2019, **16**, 90–101.
10 A. Rafieerad, W. Yan, A. Amiri and S. Dhingra, *Mater. Des.*, 2020, **196**, 109091.
11 S. Jin, H. Chen, K. Pan, R. Li, X. Ma, R. Yuan, X. Meng and H. He, *Talanta*, 2024, **270**, 125557.
12 S. I. G. P. Mohamed, S. Namvar, T. Zhang, H. Shahbazi, Z. Jiang, A. M. Rappe, A. Salehi-Khojin and S. Nejati, *Adv. Mater.*, 2024, **36**, 2309302.
13 W. Dai, H. Dong and X. Zhang, *Materials*, 2018, **11**, 1776.
14 P. Das, L. Biswal and K. Parida, *Catal. Sci. Technol.*, 2025, **15**, 6976–7003.
15 Q. Xu, Y. Niu, J. Li, Z. Yang, J. Gao, L. Ding, H. Ni, P. Zhu, Y. Liu, Y. Tang, Z.-P. Lv, B. Peng, T. S. Hu, H. Zhou and C. Xu, *Carbon Neutrality*, 2022, **1**, 13.
16 K. Kannan, K. K. Sadasivuni, A. M. Abdullah and B. Kumar, *Catalysts*, 2020, **10**, 495.
17 S. Gokul Eswaran, M. Rashad, A. Santhana Krishna Kumar and A. F. M. El-Mahdy, *Chem. – Asian J.*, 2025, **20**, e202401181.
18 Y. Cheng, B. Jiang, S. Chaemchuen, F. Verpoort and Z. Kou, *Carbon Neutralization*, 2023, **2**, 213–234.
19 C. Zhou, K. B. Tan, W. Han, L. Wang and M. Lu, *Particuology*, 2024, **91**, 50–71.
20 Sariga, A. M. Babu, S. Kumar, R. Rajeev, D. A. Thadathil and A. Varghese, *Adv. Mater. Interfaces*, 2023, **10**, 2202139.
21 B. Shao, Z. Liu, G. Zeng, H. Wang, Q. Liang, Q. He, M. Cheng, C. Zhou, L. Jiang and B. Song, *J. Mater. Chem. A*, 2020, **8**, 7508–7535.
22 J. Lu, Y. Jung Lee, X. Luo, K. Chun Lau, M. Asadi, H.-H. Wang, S. Brombosz, J. Wen, D. Zhai, Z. Chen, D. J. Miller, Y. Sub Jeong, J.-B. Park, Z. Zak Fang, B. Kumar, A. Salehi-Khojin, Y.-K. Sun, L. A. Curtiss and K. Amine, *Nature*, 2016, **529**, 377–382.
23 J. Shao, J. Zhang, C. Jiang, J. Lin and P. Huang, *Chem. Eng. J.*, 2020, **400**, 126009.
24 A. Rafieerad, W. Yan, K. N. Alagarsamy, A. Srivastava, N. Sareen, R. C. Arora and S. Dhingra, *Adv. Funct. Mater.*, 2021, **31**, 2106786.
25 B. Anasori, M. R. Lukatskaya and Y. Gogotsi, *Nat. Rev. Mater.*, 2017, **2**, 16098.

26 D. Lei, N. Liu, T. Su, Q. Zhang, L. Wang, Z. Ren and Y. Gao, *Adv. Mater.*, 2022, **34**, 2110608.
27 P. O. Å. Persson and J. Rosen, *Curr. Opin. Solid State Mater. Sci.*, 2019, **23**, 100774.
28 G. Murali, J. K. Reddy Modigunta, Y. H. Park, J.-H. Lee, J. Rawal, S.-Y. Lee, I. In and S.-J. Park, *ACS Nano*, 2022, **16**, 13370–13429.
29 R. M. Ronchi, J. T. Arantes and S. F. Santos, *Ceram. Int.*, 2019, **45**, 18167–18188.
30 J. Halim, J. Palisaitis, J. Lu, J. Thörnberg, E. J. Moon, M. Precner, P. Eklund, P. O. Å. Persson, M. W. Barsoum and J. Rosen, *ACS Appl. Nano Mater.*, 2018, **1**, 2455–2460.
31 B. Anasori and Y. Gogotsi, *Graphene 2D Mater.*, 2022, **7**, 75–79.
32 K. Khan, A. K. Tareen, M. Iqbal, I. Hussain, A. Mahmood, U. Khan, M. F. Khan, H. Zhang and Z. Xie, *J. Mater. Chem. A*, 2023, **11**, 19764–19811.
33 Y. Li, L. Ding, Y. Guo, Z. Liang, H. Cui and J. Tian, *ACS Appl. Mater. Interfaces*, 2019, **11**, 41440–41447.
34 J. Ge, W. Li, X. He, H. Chen, W. Fang, X. Du, Y. Li and L. Zhao, *Mater. Today Energy*, 2020, **18**, 100562.
35 Z. Yuan, H. Huang, N. Li, D. Chen, Q. Xu, H. Li, J. He and J. Lu, *J. Hazard. Mater.*, 2021, **409**, 125027.
36 Q. Xu, L. Ding, Y. Wen, W. Yang, H. Zhou, X. Chen, J. Street, A. Zhou, W.-J. Ong and N. Li, *J. Mater. Chem. C*, 2018, **6**, 6360–6369.
37 H. Cheng, L. Ding, G. Chen, L. Zhang, J. Xue and H. Wang, *Adv. Mater.*, 2018, **30**, 1803694.
38 J. Sun, H. Du, Z. Chen, L. Wang and G. Shen, *Nano Res.*, 2022, **15**, 3653–3659.
39 M. A. Al-Duais, Z. M. Mohammedsaleh, H. S. Al-Shehri, Y. S. Al-Awthan, S. A. Bani-Atta, A. A. Keshk, S. K. Mustafa, A. D. Althaqafy, J. N. Al-Tweher, H. A. Al-Aoh and C. Panneerselvam, *Luminescence*, 2022, **37**, 633–641.
40 M. Devi, S. Rawat and S. Sharma, *Oxford Open Mater. Sci.*, 2021, **1**, itab014.
41 C. Lai, Z. An, H. Yi, X. Huo, L. Qin, X. Liu, B. Li, M. Zhang, S. Liu, L. Li, Y. Fu, X. Zhou, Z. Wang, N. An and X. Shi, *J. Colloid Interface Sci.*, 2021, **600**, 161–173.
42 Y. Wang, C. Li, X. Han, D. Liu, H. Zhao, Z. Li, P. Xu and Y. Du, *ACS Appl. Nano Mater.*, 2018, **1**, 5366–5376.
43 X. Chen, X. Sun, W. Xu, G. Pan, D. Zhou, J. Zhu, H. Wang, X. Bai, B. Dong and H. Song, *Nanoscale*, 2018, **10**, 1111–1118.
44 R. Liu, B. Zhang, L. Fu, Z. Fu, H. Xie, Y. Tang, H. Wang and D. Sun, *Mater. Today Chem.*, 2024, **35**, 101903.
45 G. Yang, J. Zhao, S. Yi, X. Wan and J. Tang, *Sens. Actuators, B*, 2020, **309**, 127735.
46 J. Liu, S. Chen, J. He, R. Huang, L. Tao, Y. Zhao and Y. Yang, *Nanomaterials*, 2022, **12**, 2043.
47 S. M. Mousavi, M. Y. Kalashgrani, M. Binazadeh, Y. Mazaheri, N. Omidifar, V. Rahmanian, M. Riazi, C. W. Lai, R. H. Althomali, M. M. Rahman, A. Gholami and W.-H. Chiang, *Mater. Today Chem.*, 2024, **38**, 102097.
48 T. S. de Windt, L. A. Vonk, I. C. M. Slaper-Cortenbach, R. Nizak, M. H. P. van Rijen and D. B. F. Saris, *Stem Cells*, 2017, **35**, 1984–1993.
49 A. Trounson and C. McDonald, *Cell Stem Cell*, 2015, **17**, 11–22.
50 Y. Zhang, M. Li, X. Zhang, P. Zhang, Z. Liu, M. Feng, G. Ren and J. Liu, *Colloids Surf., B*, 2023, **221**, 113005.
51 A. Rafieerad, W. Yan, G. L. Sequiera, N. Sareen, E. Abu-El-Rub, M. Moudgil and S. Dhingra, *Adv. Healthcare Mater.*, 2019, **8**, 1900569.
52 D. Xiao, C. Wu, B. Liang, S. Jiang, J. Ma and Y. Li, *J. Mater. Chem. A*, 2024, **12**, 31655–31661.
53 A. M. Jastrzębska, A. Szuplewska, T. Wojciechowski, M. Chudy, W. Ziemkowska, L. Chlubny, A. Rozmysłowska and A. Olszyna, *J. Hazard. Mater.*, 2017, **339**, 1–8.
54 B. C. Bejgum and M. D. Donovan, *Mol. Pharm.*, 2021, **18**, 429–440.
55 L. Rueda-Gensini, J. Cifuentes, M. C. Castellanos, P. R. Puentes, J. A. Serna, C. Muñoz-Camargo and J. C. Cruz, *Nanomaterials*, 2020, **10**, 1816.
56 S. Y. Won, R. Singhmar, S. Sahoo, H. Kim, C. M. Kim, S. M. Choi, A. Sood and S. S. Han, *Colloids Surf., B*, 2025, **245**, 114207.
57 G. Yang and S.-J. Park, *Materials*, 2019, **12**, 1177.
58 B. Hu, J. Chen, Z. Gao, L. Chen, T. Cao, H. Li, Q. Yu, C. Wang and Z. Gan, *ACS Appl. Bio Mater.*, 2024, **7**, 4339–4351.
59 L. Jia, S. Zhou, A. Ahmed, Z. Yang, S. Liu, H. Wang, F. Li, M. Zhang, Y. Zhang and L. Sun, *Chem. Eng. J.*, 2023, **475**, 146361.
60 L. Song, S. Zhu, L. Tong, W. Wang, C. Ouyang, F. Xu and Y. Wang, *Mater. Adv.*, 2021, **2**, 5622–5628.
61 F. Shahzad, A. Iqbal, H. Kim and C. M. Koo, *Adv. Mater.*, 2020, **32**, 2002159.
62 K. Jin and X. Liu, *Surf. Interfaces*, 2024, **44**, 103790.
63 X. Jiang, A. V. Kuklin, A. Baev, Y. Ge, H. Ågren, H. Zhang and P. N. Prasad, *Phys. Rep.*, 2020, **848**, 1–58.
64 M. Wan, J. Zhou, H. Yang, X. Dai, Y. Zheng, Z. Xia and L. Wang, *ACS Appl. Nano Mater.*, 2022, **5**, 11715–11722.
65 C. Fu, F. Ai, J. Huang, Z. Shi, X. Yan and X. Zheng, *Spectrochim. Acta, Part A*, 2022, **272**, 120956.
66 Z. Guo, X. Zhu, S. Wang, C. Lei, Y. Huang, Z. Nie and S. Yao, *Nanoscale*, 2018, **10**, 19579–19585.
67 G. Xu, Y. Niu, X. Yang, Z. Jin, Y. Wang, Y. Xu and H. Niu, *Adv. Opt. Mater.*, 2018, **6**, 1800951.
68 X. Gao, X. Shao, L. Qin, Y. Li, S. Huang and L. Deng, *Nanoscale Res. Lett.*, 2021, **16**, 160.
69 Z. Jin, C. Liu, Z. Liu, J. Han, Y. Fang, Y. Han, Y. Niu, Y. Wu, C. Sun and Y. Xu, *Adv. Energy Mater.*, 2020, **10**, 2000797.
70 Q. Zhang, Y. Sun, M. Liu and Y. Liu, *Nanoscale*, 2020, **12**, 1826–1832.
71 H. Zhang, L. Wang, T. Zhuang, Z. Wei, J. Xia and Z. Wang, *Anal. Bioanal. Chem.*, 2022, **414**, 6753–6760.
72 Y. Nie, Z. Liang, P. Wang, Q. Ma and X. Su, *Anal. Chem.*, 2021, **93**, 17086–17093.
73 Y. Liu, N. Ye, X. Li, X. Li, H. Liu, E. Wang, C. Liang and X. Peng, *J. Solid State Chem.*, 2021, **293**, 121781.
74 Y. Feng, F. Zhou, Q. Deng and C. Peng, *Ceram. Int.*, 2020, **46**, 8320–8327.

75 L. Zhao, Z. Wang, Y. Li, S. Wang, L. Wang, Z. Qi, Q. Ge, X. Liu and J. Z. Zhang, *J. Mater. Sci. Technol.*, 2021, **78**, 30–37.
76 X. Ding, L. Qu, R. Yang, Y. Zhou and J. Li, *Luminescence*, 2015, **30**, 465–471.
77 F. Yang, Y. Ge, T. Yin, J. Guo, F. Zhang, X. Tang, M. Qiu, W. Liang, N. Xu, C. Wang, Y. Song, S. Xu and S. Xiao, *ACS Appl. Nano Mater.*, 2020, **3**, 11850–11860.
78 L. Gnanasekaran, R. Hemamalini and K. Ravichandran, *J. Saudi Chem. Soc.*, 2015, **19**, 589–594.
79 F. He, B. Zhu, B. Cheng, J. Yu, W. Ho and W. Macyk, *Appl. Catal., B*, 2020, **272**, 119006.
80 N. Prudhvi Raju, D. Tripathi, S. Lahiri and R. Thangavel, *Sol. Energy*, 2023, **259**, 107–118.
81 L. Ding, S. Zeng, W. Zhang, C. Guo, X. Chen, B. Peng, Z. Lv, H. Zhou and Q. Xu, *ACS Appl. Energy Mater.*, 2022, **5**, 11540–11552.
82 G. Cai, Z. Yu, P. Tong and D. Tang, *Nanoscale*, 2019, **11**, 15659–15667.
83 H. Wang, R. Zhao, H. Hu, X. Fan, D. Zhang and D. Wang, *ACS Appl. Mater. Interfaces*, 2020, **12**, 40176–40185.
84 Y. Bai, Y. He, M. Wang and G. Song, *Sens. Actuators, B*, 2022, **357**, 131410.
85 Y. Wang, J. Wang, P. Ma, H. Yao, L. Zhang and Z. Li, *New J. Chem.*, 2017, **41**, 14918–14923.
86 Q. Xue, H. Zhang, M. Zhu, Z. Pei, H. Li, Z. Wang, Y. Huang, Y. Huang, Q. Deng, J. Zhou, S. Du, Q. Huang and C. Zhi, *Adv. Mater.*, 2017, **29**, 1604847.
87 K. Gao, L. Hou, X. An, D. Huang and Y. Yang, *Appl. Catal., B*, 2023, **323**, 122150.
88 X. Wang, X. Zhang, H. Cao and Y. Huang, *J. Mater. Chem. B*, 2020, **8**, 10837–10844.
89 G. P. Neupane, B. Wang, M. Tebyetekerwa, H. T. Nguyen, M. Taheri, B. Liu, M. Nauman and R. Basnet, *Small*, 2021, **17**, 2006309.
90 Q. Xu, J. Ma, W. Khan, X. Zeng, N. Li, Y. Cao, X. Zhao and M. Xu, *Chem. Commun.*, 2020, **56**, 6648–6651.
91 L. Zhou, F. Wu, J. Yu, Q. Deng, F. Zhang and G. Wang, *Carbon*, 2017, **118**, 50–57.
92 X. Li, F. Liu, D. Huang, N. Xue, Y. Dang, M. Zhang, L. Zhang, B. Li, D. Liu, L. Wang, H. Liu and X. Tao, *Adv. Funct. Mater.*, 2020, **30**, 2000308.
93 Z. Wang, Y. Zhu, Y. Wu, W. Ding and X. Li, *Nanoscale*, 2022, **14**, 9498–9506.
94 X. Huang and P. Wu, *Adv. Funct. Mater.*, 2020, **30**, 1910048.
95 B. Yan, Z. Cheng, C. Lai, B. Qiao, R. Yuan, C. Zhang, H. Pei, J. Tu and Q. Wu, *Nanomaterials*, 2022, **12**, 3557.
96 W. Han, X. Wen, Y. Ding, Z. Li, M. Lu, H. Zhu, G. Wang, J. Yan and X. Hong, *Appl. Surf. Sci.*, 2022, **595**, 153563.
97 H. Alijani, A. R. Rezk, M. M. Khosravi Farsani, H. Ahmed, J. Halim, P. Reineck, B. J. Murdoch, A. El-Ghazaly, J. Rosen and L. Y. Yeo, *ACS Nano*, 2021, **15**, 12099–12108.
98 B. Yu, A. Huang, D. Chen, K. Srinivas, X. Zhang, X. Wang, B. Wang, F. Ma, C. Liu, W. Zhang, J. He, Z. Wang and Y. Chen, *Small*, 2021, **17**, 2100460.
99 M. Liu, Y. Bai, Y. He, J. Zhou, Y. Ge, J. Zhou and G. Song, *Microchim. Acta*, 2021, **188**, 15.
100 F. Yan, J. Sun, Y. Zang, Z. Sun, H. Zhang, J. Xu and X. Wang, *Dyes Pigm.*, 2021, **195**, 109720.
101 X. Jiang, H. Wang, Y. Shen, N. Hu and W. Shi, *Sens. Actuators, B*, 2022, **350**, 130891.
102 Q. Guan, J. Ma, W. Yang, R. Zhang, X. Zhang, X. Dong, Y. Fan, L. Cai, Y. Cao, Y. Zhang, N. Li and Q. Xu, *Nanoscale*, 2019, **11**, 14123–14133.
103 W. Kong, Y. Niu, M. Liu, K. Zhang, G. Xu, Y. Wang, X. Wang, Y. Xu and J. Li, *Inorg. Chem. Commun.*, 2019, **105**, 151–157.
104 Q. Lu, J. Wang, B. Li, C. Weng, X. Li, W. Yang, X. Yan, J. Hong, W. Zhu and X. Zhou, *Anal. Chem.*, 2020, **92**, 7770–7777.
105 M. Liu, Y. He, J. Zhou, Y. Ge, J. Zhou and G. Song, *Anal. Chim. Acta*, 2020, **1103**, 134–142.
106 S. Li, J. Ma, X. Zhao, P. Zhu, M. Xu, Y. Niu, D. Luo and Q. Xu, *Chin. Chem. Lett.*, 2022, **33**, 1850–1854.
107 D. Huang, Y. Wu, F. Ai, X. Zhou and G. Zhu, *Sens. Actuators, B*, 2021, **342**, 130074.
108 Z. Wang, Y. Zhu, Y. Wu, W. Ding and X. Li, *Nanoscale*, 2022, **14**, 9498–9506.
109 Y. Bai, Y. He, Y. Wang and G. Song, *Microchim. Acta*, 2021, **188**, 401.
110 M. Liu, J. Zhou, Y. He, Z. Cai, Y. Ge, J. Zhou and G. Song, *Microchim. Acta*, 2019, **186**, 770.
111 N. Mohamadbeigi, L. Shooshtari, S. Fardindoost, M. Vafaiee, A. Iraji zad and R. Mohammadpour, *Sci. Rep.*, 2024, **14**, 1562.
112 I. I. Ebralidze, N. O. Laschuk, J. Poisson and O. V. Zenkina, in *Nanomaterials Design for Sensing Applications*, Elsevier, 2019, pp. 1–39.
113 M. Wan, A. Jimu, H. Yang, J. Zhou, X. Dai, Y. Zheng, J. Ou, Y. Yang, J. Liu and L. Wang, *Microchem. J.*, 2023, **184**, 108180.
114 F. Ai, C. Fu, G. Cheng, H. Zhang, Y. Feng, X. Yan and X. Zheng, *ACS Appl. Nano Mater*, 2021, **4**, 8192–8199.
115 X. Chen, J. Li, G. Pan, W. Xu, J. Zhu, D. Zhou, D. Li, C. Chen, G. Lu and H. Song, *Sens. Actuators, B*, 2019, **289**, 131–137.
116 J. Hong, W. Wang, J. Wang, X. Wang, H. Xie, T. Li and N. Gan, *Microchimica Acta*, 2021, **188**, 45.
117 M. Liu, Y. Bai, Y. He, J. Zhou, Y. Ge, J. Zhou and G. Song, *Microchem. J.*, 2024, **207**, 112068.
118 L. Wang, N. Zhang, Y. Li, W. Kong, J. Gou, Y. Zhang, L. N. Wang, G. Yu, P. Zhang, H. Cheng and L. Qu, *ACS Appl. Mater. Interfaces*, 2021, **13**, 42442–42450.
119 Q. Xu, L. Ding, Y. Wen, W. Yang, H. Zhou, X. Chen, J. Street, A. Zhou, W. J. Ong and N. Li, *J. Mater. Chem. C*, 2018, **6**, 6360–6369.
120 M. Wan, J. Zhou, H. Yang, X. Dai, Y. Zheng, Z. Xia and L. Wang, *ACS Appl. Nano Mater.*, 2022, **5**, 11715–11722.
121 M. A. Al-Duais, Z. M. Mohammedsaleh, H. S. Al-Shehri, Y. S. Al-Awthan, S. A. Bani-Atta, A. A. Keshk, S. K. Mustafa, A. D. Althaqafy, J. N. Al-Tweher, H. A. Al-Aoh and C. Panneerselvam, *Luminescence*, 2022, **37**, 633–641.

122 Y. Cheng, P. Shen, X. Li, X. Li, K. Chu and Y. Guo, *Sens. Actuators, B*, 2023, **376**, 132979.
123 P. Jin, P. Wan, C. Zhang, X. Li, Y. Wang, J. Luo and K. Li, *Anal. Chim. Acta*, 2024, **1303**, 342517.
124 C. Lin, C. Qiu, Y. Wang, Y. Liu, M. Rong and L. Niu, *Sens. Diagn.*, 2024, **3**, 431–439.
125 Z. Ding, X. Zhan, Y. Zhang, K. Chu and Y. Guo, *Microchem. J.*, 2024, **207**, 111951.
126 R. Rajamanikandan, K. Sasikumar and H. Ju, *Anal. Chim. Acta*, 2024, **1322**, 343069.
127 M. H. Azar, H. Abdollahi, S. Arabloo, N. Mohamadbeigi, A. F. Sohi, A. Simchi and K. Musselman, *Prog. Mater. Sci.*, 2025, **158**, 101624.
128 D. Huang, Y. Xie, D. Lu, Z. Wang, J. Wang, H. Yu and H. Zhang, *Adv. Mater.*, 2019, **31**, 1901117.
129 X. (Xiao) Liu, Z. Zhang, J. Jiang, C. Tian, X. Wang, L. Wang, Z. Zhang, X. Wu, Y. Zheng, J. Liang and C.-C. Chen, *Chem. Eng. J.*, 2022, **432**, 134382.
130 Y. Niu, C. Tian, J. Gao, F. Fan, Y. Zhang, Y. Mi, X. Ouyang, L. Li, J. Li, S. Chen, Y. Liu, H.-L. Lu, X. Zhao, L. Yang, H. Ju, Y. Yang, C.-F. Ding, M. Xu and Q. Xu, *Nano Energy*, 2021, **89**, 106455.
131 Y. Yang, H. Lu, S. Feng, L. Yang, H. Dong, J. Wang, C. Tian, L. Li, H. Lu, J. Jeong, S. M. Zakeeruddin, Y. Liu, M. Grätzel and A. Hagfeldt, *Energy Environ. Sci.*, 2021, **14**, 3447–3454.
132 H. Yan, M. Chen, W. Liu, P. Wang, M. Liu, Y. Liu, L. Ye and M. Gu, *Opt. Mater.*, 2023, **140**, 113902.
133 H. Mao, C. Gu, S. Yan, Q. Xin, S. Cheng, P. Tan, X. Wang, F. Xiu, X. Liu, J. Liu, W. Huang and L. Sun, *Adv. Electron. Mater.*, 2020, **6**, 1900493.
134 C. Qiao, H. Wu, X. Xu, Z. Guan and W. Ou-Yang, *Adv. Mater. Interfaces*, 2021, **8**, 2100903.
135 Q. Zhu, Y. Cui, Y. Zhang, Z. Cao, Y. Shi, J. Gu, Z. Du, B. Li and S. Yang, *Mater. Today Nano*, 2021, **13**, 100104.
136 S. Xiao, Y. Zheng, X. Wu, M. Zhou, X. Rong, L. Wang, Y. Tang, X. Liu, L. Qiu and C. Cheng, *Small*, 2022, **18**, 2203281.
137 P. Liu, H. Liu, T. Zhang, L. Chen, W. Guo, T. Gu, F. Yu, Y. Liu and G. Wang, *Chem. Eng. J.*, 2023, **477**, 146913.
138 X. Li, C. Wen, M. Yuan, Z. Sun, Y. Wei, L. Ma, H. Li and G. Sun, *J. Alloys Compd.*, 2020, **824**, 153803.
139 L. Zhang, X. Ji, X. Ren, Y. Ma, X. Shi, Z. Tian, A. M. Asiri, L. Chen, B. Tang and X. Sun, *Adv. Mater.*, 2018, **30**, 1800191.
140 M. A. K. Purbayanto, M. Chandel, M. Birowska, A. Rosenkranz and A. M. Jastrzębska, *Adv. Mater.*, 2023, **35**, 2301850.
141 Y. Liu, W. Zhang, X. Zou, Y. Yan, Q. Liang, F. Liu, W. Li, K. Song, X. Zhou, Z. Chen and W. Zheng, *Acta Mater.*, 2025, **283**, 120507.
142 G. Dong, Y. Zhang, Y. Wang, Q. Deng, C. Qin, Y. Hu, Y. Zhou and G. Tian, *ACS Appl. Energy Mater.*, 2021, **4**, 14342–14351.
143 B. Li, D. Shen, Z. Xiao, Q. Li, S. Yao, W. Wang and L. Liu, *Inorg. Chem. Front.*, 2023, **10**, 5927–5936.
144 J. Nie, X. Zhang, M. Wang, Y. Ou, S. Li, P. Zhong, W. Wang, G. Zhu and X. Ma, 2024, preprint, DOI: 10.2139/ssrn.4829261.
145 Z. Zeng, Y. Yan, J. Chen, P. Zan, Q. Tian and P. Chen, *Adv. Funct. Mater.*, 2019, **29**, 1806500.
146 S. Shen, T. Ke, K. Rajavel, K. Yang and D. Lin, *Small*, 2020, **16**, 2002433.
147 Y. Huang, X. Wang, H. Zhang, L. Gao, J. Meng, Y. Liao, Q. Zhou, Y. Wei, B. Zong, H. Li and W.-L. Dai, 2025, preprint, DOI: 10.2139/ssrn.5095895.
148 Y. Cao, T. Wu, K. Zhang, X. Meng, W. Dai, D. Wang, H. Dong and X. Zhang, *ACS Nano*, 2019, **13**, 1499–1510.
149 X. Yu, X. Cai, H. Cui, S.-W. Lee, X.-F. Yu and B. Liu, *Nanoscale*, 2017, **9**, 17859–17864.
150 W. Dai, H. Dong and X. Zhang, *Materials*, 2018, **11**, 1776.
151 Q. Xue, H. Zhang, M. Zhu, Z. Pei, H. Li, Z. Wang and Y. Huang, *J. Mater. Chem. A*, 2017, **5**, 20818–20823.
152 X. Zhou, J. Zhang, D. Huang, Y. Yi, K. Wu and G. Zhu, *Spectrochim. Acta, Part A*, 2023, **293**, 122484.
153 M. K. Schnizler, R. Bogdan, A. Bennert, N. R. Bury, M. Fronius and W. Clauss, *Biochim. Biophys. Acta, Biomembr.*, 2007, **1768**, 317–323.
154 J. Gu, X. Lu, G. Li, B. Shan, J. Liu, Y. Qu, H. Ye, K. Xi and H. Wu, *Chem. Eng. J.*, 2023, **467**, 143445.
155 X. Song, R. D. Airan, D. R. Arifin, A. Bar-Shir, D. K. Kadayakkara, G. Liu, A. A. Gilad, P. C. M. van Zijl, M. T. McMahon and J. W. M. Bulte, *Nat. Commun.*, 2015, **6**, 6719.
156 N. Mohamadbeigi, N. Rafiefard, F. Ejehi, R. Mohammadpour and A. Iraji zad, *Energy Technol.*, 2024, **12**, 2301136.
157 L. Feng, J. Luo, X. Ma, J. Cui, Y. Chen, J. Lu, L. Zhang and Z. Pei, *Opt. Express*, 2022, **30**, 34129.
158 Z. Li, Q. Chen, G. Wen and Z. Jiang, *Langmuir*, 2024, **40**, 17358–17366.
159 Z. Yu, C. Deng, S. Jiang, Y. Liu, C. Liu, F. Seidi, X. Zhang, Y. Huang, W. Wu, J. Han, Q. Yong and H. Xiao, *J. Colloid Interface Sci.*, 2025, **679**, 510–520.
160 P. Pust, V. Weiler, C. Hecht, A. Tücks, A. S. Wochnik, A.-K. Henß, D. Wiechert, C. Scheu, P. J. Schmidt and W. Schnick, *Nat. Mater.*, 2014, **13**, 891–896.
161 H.-Y. Lin, C.-W. Sher, C.-H. Lin, H.-H. Tu, X. Y. Chen, Y.-C. Lai, C.-C. Lin, H.-M. Chen, P. Yu, H.-F. Meng, G.-C. Chi, K. Honjo, T.-M. Chen and H.-C. Kuo, *ACS Appl. Mater. Interfaces*, 2017, **9**, 35279–35286.
162 M. H. Azar, M. Mohammadi, N. T. Rezaei, S. Aynehband and A. Simchi, *J. Alloys Compd.*, 2022, **907**, 164465.
163 M. Hasanzadeh Azar, Z. Ji, J. Jahanzamin and A. Kitai, in *Silicon Carbide - Materials, Devices and Emerging Applications*, IntechOpen, 2024, DOI: 10.5772/intechopen.1007535.
164 M. Hasanzadeh Azar, J. Jahanzamin, Z. Ji, A. Kitai, D. Beke and A. Gali, *Small Sci.*, 2025, **5**, 2500013.
165 S.-W. Chang, W.-C. Liao, Y.-M. Liao, H.-I. Lin, H.-Y. Lin, W.-J. Lin, S.-Y. Lin, P. Perumal, G. Haider, C.-T. Tai, K.-C. Shen, C.-H. Chang, Y.-F. Huang, T.-Y. Lin and Y.-F. Chen, *Sci. Rep.*, 2018, **8**, 2720.

166 G. Haider, H.-I. Lin, K. Yadav, K.-C. Shen, Y.-M. Liao, H.-W. Hu, P. K. Roy, K. P. Bera, K.-H. Lin, H.-M. Lee, Y.-T. Chen, F.-R. Chen and Y.-F. Chen, *ACS Nano*, 2018, **12**, 11847–11859.
167 M. L. Pascu, N. Moise and A. Staicu, *J. Mol. Struct.*, 2001, **598**, 57–64.
168 A. Szukalska, A. Szukalski, M. Adaszynski and J. Mysliwiec, *Adv. Opt. Mater.*, 2023, **11**, 2300266.
169 F. Fan, S. Turkdogan, Z. Liu and C.-Z. Ning, in *2016 IEEE Photonics Conference (IPC)*, IEEE, 2016, pp. 90–90.
170 K. Yamashita, N. Takeuchi, K. Oe and H. Yanagi, *Opt. Lett.*, 2010, **35**, 2451.
171 C. Dang, J. Lee, C. Breen, J. S. Steckel, S. Coe-Sullivan and A. Nurmikko, *Nat. Nanotechnol.*, 2012, **7**, 335–339.
172 X. P. Hu, G. Zhao, Z. Yan, X. Wang, Z. D. Gao, H. Liu, J. L. He and S. N. Zhu, *Opt. Lett.*, 2008, **33**, 408.
173 S. Liu, V. P. Biju, Y. Qi, W. Chen and Z. Liu, *NPG Asia Mater.*, 2023, **15**, 27.
174 M. Hasanzadeh Azar, S. Aynehband, H. Abdollahi, H. Alimohammadi, N. Rajabi, S. Angizi, V. Kamraninejad, R. Teimouri, R. Mohammadpour and A. Simchi, *Photonics*, 2023, **10**, 271.
175 S. Aynehband, M. H. Azar, J.-M. Nunzi and A. Simchi, *Mater. Lett.*, 2025, **397**, 138810.
176 M. Hasanzadeh Azar, M. Mohammadi, N. T. Rezaei, S. Aynehband, L. Shooshtari, R. Mohammadpour and A. Simchi, *ACS Appl. Nano Mater.*, 2021, **4**, 7788–7799.
177 M. Hasanzadeh Azar, H. Abdollahi, S. Arabloo and A. Simchi, *J. Mater. Chem. C*, 2025, **13**, 9061–9071.
178 Q.-Q. Chu, Z. Sun, D. Wang, B. Cheng, H. Wang, C.-P. Wong and B. Fang, *Matter*, 2023, **6**, 3838–3863.
179 S. Shao and M. A. Loi, *Adv. Mater. Interfaces*, 2020, **7**, 1901469.
180 S. Palei, G. Murali, C.-H. Kim, I. In, S.-Y. Lee and S.-J. Park, *Nano-Micro Lett.*, 2023, **15**, 123.
181 M. S. K T and P. Karupppanan, *Chem. Phys. Impact*, 2024, **8**, 100610.
182 S. Qamar, K. Fatima, N. Ullah, Z. Akhter, A. Waseem and M. Sultan, *Nanoscale*, 2022, **14**, 13018–13039.
183 Z. Shi, R. Khaledialidusti, M. Malaki and H. Zhang, *Nanomaterials*, 2021, **11**, 3170.
184 L. Yang, P. Li, J. Ma, X. Zhang, X.-F. Wang and Y. Liu, *J. Energy Chem.*, 2023, **81**, 443–461.
185 M. A. Saeed, A. Shahzad, K. Rasool, F. Mateen, J. Oh and J. W. Shim, *Adv. Sci.*, 2022, **9**, 2104743.
186 X. Chen, W. Xu, N. Ding, Y. Ji, G. Pan, J. Zhu, D. Zhou, Y. Wu, C. Chen and H. Song, *Adv. Funct. Mater.*, 2020, **30**, 2003295.
187 D. L. Narayanan, R. N. Saladi and J. L. Fox, *Int. J. Dermatol.*, 2010, **49**, 978–986.
188 S. Aynehband, M. Mohammadi, R. Poushimin, M. H. Azar, J.-M. Nunzi and A. Simchi, *Mater. Res. Bull.*, 2022, **147**, 111648.
189 Q. Wang, H. Wang, R. Xue, M. Ning, S. Li, P. Chen, M. Sun and Z. Li, *J. Alloys Compd.*, 2023, **965**, 171399.
190 A. Singh, S. Mahapatra, R. Prasad, S. K. Singh and P. Chandra, *Nanoscale*, 2025, **17**, 15554–15591.
191 A. S. Sharbirin, R. E. Kong, W. B. Mato, T. T. Tran, E. Lee, J. W. P. Khor, A. L. Fadli and J. Kim, *Opto-Electron. Adv.*, 2024, **7**, 240029–240029.
192 L. Thyda, K. Naresh, J. K. Joseph, S. Suneetha, C. E. Jeyanthi, P. Amaladass, C. Selvaraju and K. Thangaraju, *Thin Solid Films*, 2024, **790**, 140221.
193 H. Lu, J. He, Z. Hu, X. Hu, P. He, Y. Zhao, M. Hao and L. Tao, *Infrared Phys. Technol.*, 2021, **119**, 103962.
194 J. Du, M. Zhang, Z. Guo, J. Chen, X. Zhu, G. Hu, P. Peng, Z. Zheng and H. Zhang, *Sci. Rep.*, 2017, **7**, 42357.
195 N. Xu, H. Li, Y. Gan, H. Chen, W. Li, F. Zhang, X. Jiang, Y. Shi, J. Liu, Q. Wen and H. Zhang, *Adv. Sci.*, 2020, **7**, 2002209.
196 Y. Shi, H. Long, S. Liu, Y. H. Tsang and Q. Wen, *J. Mater. Chem. C*, 2018, **6**, 12638–12642.
197 J. S. Meena, S. M. Sze, U. Chand and T.-Y. Tseng, *Nanoscale Res. Lett.*, 2014, **9**, 526.
198 S. Tappertzhofen, in *Metal Oxides for Non-volatile Memory*, Elsevier, 2022, pp. 1–32.
199 S. Gokul Eswaran, M. Rashad, A. Santhana Krishna Kumar and A. F. M. El-Mahdy, *Chem. – Asian J.*, 2025, **20**, e202401181.
200 B. Vénosová and F. Karlický, *Nanoscale Adv.*, 2023, **5**, 7067–7076.
201 J. Zhang, R. Jia, K. B. Tan, J. Li, S. Xu, G. Ying, W. Han and M. Lu, *Nano-Micro Lett.*, 2025, **17**, 173.
202 Z. Wang, Y. Wang, Q. Gu, C. Zhao, J. Zhang, S. Xu, M. Lu and B. Zhang, *Particuology*, 2023, **72**, 10–16.
203 Z. Fan, Y. Li, J. Pan, Z. Zhou, W. Li, T. Yang, H. Zhang, C. Shu, W. Hua, Y. Wu and W. Tang, *EES Batteries*, 2025, **1**, 100–118.
204 J. Sun, B. S. Shengping Zhang, M. Alomar, A. S. Alqarni, M. S. Najla Alotaibi, M. S. Badriah Alshahrani, A. A. Alghamdi, Z. Kou, W. Shen, Y. Chen and J. Zhang, *Chem. Rec.*, 2023, **23**, e202200268.
205 J. Wang, Y. Hong, Y. Pan, J. Zhu, X. Xu, W. M. Choi and J. Yang, *Mater. Chem. Phys.*, 2024, **312**, 128634.
206 S. Liu, H. Zhang, J. Chen, X. Peng, Y. Chai, X. Shao, Y. He, X. Wang and B. Ding, *Energies*, 2025, **18**, 1223.
207 C.-M. Fung, B.-J. Ng, Y.-H. Chew, C.-C. Er, J. Low, X. Guo, X. Y. Kong, L.-L. Tan, H. Onishi, A. R. Mohamed and S.-P. Chai, *Cell Rep. Phys. Sci.*, 2024, **5**, 102296.
208 T. Ramachandran, F. Hamed, Y. A. Kumar, R. K. Raji and H. H. Hegazy, *J. Energy Storage*, 2023, **73**, 109299.
209 A. M. Bogale, T. Ramachandran, M. E. Suk, B. B. Badassa, M. M. Solomon, J. He, A. Yusuf, R. K. Raji, B. A. Zenebe, N. K. Amare and F. B. Tesema, *J. Phys. Chem. Solids*, 2026, **208**, 113079.
210 T. Ramachandran, F. Hamed, R. K. Raji, S. M. Majhi, D. Barik, Y. A. Kumar, R. O. M. U. Jauhar, M. P. Pachamuthu, L. Vijayalakshmi and S. Ansar, *J. Phys. Chem. Solids*, 2023, **180**, 111467.
211 C. Choi, D. S. Ashby, D. M. Butts, *et al.*, *Nat Rev Mater.*, 2020, **5**, 5–19.

212 T. Ramachandran, R. K. Raji, S. Palanisamy, N. Renuka and K. Karuppasamy, *J. Ind. Eng. Chem.*, 2025, **145**, 144–168.
213 P. Naskar, D. Kundu, A. Maiti, P. Chakraborty, B. Biswas and A. Banerjee, *ChemElectroChem*, 2021, **8**, 1393–1429.
214 D. G. Gibson, J. I. Glass, C. Lartigue, V. N. Noskov, R.-Y. Chuang, M. A. Algire, G. A. Benders, M. G. Montague, L. Ma, M. M. Moodie, C. Merryman, S. Vashee, R. Krishnakumar, N. Assad-Garcia, C. Andrews-Pfannkoch, E. A. Denisova, L. Young, Z.-Q. Qi, T. H. Segall-Shapiro, C. H. Calvey, P. P. Parmar, C. A. Hutchison, H. O. Smith and J. C. Venter, *Science*, 2010, **329**, 52–56.
215 P. Seraji, H. Shahbazi, M. K. Ncube, N. Shan, F. Lagunas, I. Papailias, P. Navabi, C. Zhang, A. Jaradat, S. Kadkhodaei, K. D. Glusac, R. F. Klie, A. T. Ngo, L. A. Curtiss and A. Salehi-Khojin, *Nano Energy*, 2025, **134**, 110510.
216 A. Jaradat, C. Zhang, S. K. Singh, J. Ahmed, A. Ahmadiparidari, L. Majidi, S. Rastegar, Z. Hemmat, S. Wang, A. T. Ngo, L. A. Curtiss, M. Daly, A. Subramanian and A. Salehi-khojin, *Small*, 2021, **17**, 2102072.
217 X. Zheng, M. Yuan, D. Guo, C. Wen, X. Li, X. Huang, H. Li and G. Sun, *ACS Nano*, 2022, **16**, 4487–4499.
218 J. Gan, F. Li and Q. Tang, *J. Phys. Chem. Lett.*, 2021, **12**, 4805–4813.
219 H. Chen, A. D. Handoko, T. Wang, J. Qu, J. Xiao, X. Liu, D. Legut, Z. Wei Seh and Q. Zhang, *ChemSusChem*, 2020, **13**, 5690–5698.
220 K. Eid, Q. Lu, S. Abdel-Azeim, A. Soliman, A. M. Abdullah, A. M. Abdelgwad, R. P. Forbes, K. I. Ozoemena, R. S. Varma and M. F. Shibl, *J. Mater. Chem. A*, 2022, **10**, 1965–1975.
221 H. Shahbazi, M. Kazemzadeh, A. Malek Khachatourian, P. Seraji, M. Dehghani Mohammad Abadi and M. Golmohammad, *Electrochim. Acta*, 2024, **507**, 145193.
222 P. Wang, D. Zhao, X. Hui, Z. Qian, P. Zhang, Y. Ren, Y. Lin, Z. Zhang and L. Yin, *Adv. Energy Mater.*, 2021, **11**, 2003069.
223 X. Han, N. Li, P. Xiong, M. G. Jung, Y. Kang, Q. Dou, Q. Liu, J. Y. Lee and H. S. Park, *InfoMat*, 2021, **3**, 1134–1144.
224 K. Yang, C. Li, H. Qi, Y. Dai, Y. Cui and Y. He, *J. Mater. Chem. A*, 2023, **11**, 10425–10434.
225 D. Deckenbach and J. J. Schneider, *Adv. Mater. Interfaces*, 2023, **10**, 2202494.
226 W. Sun, F. Wang, B. Zhang, M. Zhang, V. Küpers, X. Ji, C. Theile, P. Bieker, K. Xu, C. Wang and M. Winter, *Science*, 2021, **371**, 46–51.
227 Z. Zeng, G. Fu, H. Bin Yang, Y. Yan, J. Chen, Z. Yu, J. Gao, L. Y. Gan, B. Liu and P. Chen, *ACS Mater. Lett.*, 2019, **1**, 432–439.
228 H. Zhang, M. Zhu, H. Tang, Q. Lu, T. Yang, X. Wang, B. Chen, Z. Qu, X. Wang, M. Yu, D. Karnaushenko, D. D. Karnaushenko, Y. Huang, O. G. Schmidt and K. Zhang, *Energy Storage Mater.*, 2023, **59**, 102791.
229 X. Cai, L. Lai, J. Lin and Z. Shen, *Mater. Horiz.*, 2017, **4**, 945–976.
230 J.-Q. Huang, Q. Zhang, H.-J. Peng, X.-Y. Liu, W.-Z. Qian and F. Wei, *Energy Environ. Sci.*, 2014, **7**, 347–353.
231 D. Zalka, A. Vizintin, A. Maximenko, Z. Pászti, Z. Dankházi, K. Hegedüs, L. S. Shankar, R. Kun, K. Saksl, A. S. Fedorková and P. Jóvári, *Commun. Mater.*, 2025, **6**, 17.
232 R. Hou, H. Bai, X. Zhong, J. Cheng, J. Gao, J. Tang and B. Xu, *RSC Adv.*, 2025, **15**, 15443–15449.
233 D. P. Dubal, N. R. Chodankar, D.-H. Kim and P. Gomez-Romero, *Chem. Soc. Rev.*, 2018, **47**, 2065–2129.
234 L. Pradhan, B. Mohanty, G. Padhy, R. Kumar Trivedi, D. Prasad Das, B. Chakraborty and B. Kumar Jena, *Chem. Eng. J.*, 2024, **497**, 154587.
235 Z. Bo, X. Zhang, Z. Huang, Y. Huang, J. Yan, K. Cen and H. Yang, *RSC Adv.*, 2023, **13**, 15762–15771.
236 Y. Yuan, L. Jiang, X. Li, P. Zuo, X. Zhang, Y. Lian, Y. Ma, M. Liang, Y. Zhao and L. Qu, *Adv. Mater.*, 2022, **34**, 2110013.
237 J. He, F. Ma, W. Xu, X. He, Q. Li, J. Sun, R. Jiang, Z. Lei and Z. Liu, *Adv. Sci.*, 2024, **11**, 2305991.
238 E. Q. Chong, D. B. Lingerfelt, A. Petrone and X. Li, *J. Phys. Chem. C*, 2016, **120**, 19434–19441.
239 X. Zhang, Z. Zhang and Z. Zhou, *J. Energy Chem.*, 2018, **27**, 73–85.
240 Z. Ren, Y. Li and J. Yu, *iScience*, 2018, **9**, 138–148.
241 J. W. Graydon, M. Panjehshahi and D. W. Kirk, *J. Power Sources*, 2014, **245**, 822–829.
242 Z. Li, N. H. Attanayake, J. L. Blackburn and E. M. Miller, *Energy Environ. Sci.*, 2021, **14**, 6242–6286.
243 J. Zhang, C. Guo, S. Fang, X. Zhao, L. Li, H. Jiang, Z. Liu, Z. Fan, W. Xu, J. Xiao and M. Zhong, *Nat. Commun.*, 2023, **14**, 1298.
244 N. H. Solangi, L. P. Lingamdinne, R. R. Karri, N. M. Mubarak, S. A. Mazari and J. R. Koduru, *Carbon*, 2025, **232**, 119758.
245 M. Khalil, G. T. M. Kadja, F. A. A. Nugroho, L. G. Sutanto, P. K. Jiwanti, F. F. Abdi, F. Hussin and M. K. Aroua, *Renewable Sustainable Energy Rev.*, 2024, **206**, 114869.
246 A. A. Abuelwafa, R. M. Matiur, A. A. Putri and T. Soga, *Opt. Mater.*, 2020, **109**, 110413.
247 J. Nie, X. Zhang, M. Wang, Y. Ou, S. Li, P. Zhong, W. Wang, G. Zhu and X. Ma, *Sep. Purif. Technol.*, 2025, **354**, 128961.
248 R. Kim, J. Kim, J. Y. Do, M. W. Seo and M. Kang, *Catalysts*, 2019, **9**, 998.
249 S. Zhang, J. Zhou, Q. Jia, X. Ma, C. Guo, L. Li and L. Gong, 2023, preprint, DOI: 10.2139/ssrn.4625162.
250 B. Abhishek, A. Jayarama, A. S. Rao, S. S. Nagarkar, A. Dutta, S. P. Duttagupta, S. S. Prabhu and R. Pinto, *Int. J. Hydrogen Energy*, 2024, **81**, 1442–1466.
251 H. Yan and H. Yang, *J. Alloys Compd.*, 2011, **509**, L26–L29.
252 R. Ramírez, A. Melillo, S. Osella, A. M. Asiri, H. Garcia and A. Primo, *Small Methods*, 2023, **7**, 2300063.
253 M. Y. Solangi, A. A. Lakhair, F. Z. Dayo, R. A. Qureshi, A. Alhazaa, M. A. Shar, A. J. Laghari, I. A. Soomro,

M. N. Lakhan, A. Hanan and U. Aftab, *RSC Sustainability*, 2024, **2**, 3424–3435.
254 N. G. Semaltianos, *Crit. Rev. Solid State Mater. Sci.*, 2010, **35**, 105–124.
255 B. Chang, H. Zhang, S. Sun and G. Zhang, *Carbon Energy*, 2024, **6**, e491.
256 H. Yun, C. Lim, M. Kwon, D. Lee, Y. Yun, D. Seo and K. Yong, *Adv. Mater.*, 2024, **36**, 2408280.
257 R. Zhang, Y. Zhang, B. Xiao, S. Zhang, Y. Wang, H. Cui, C. Li, Y. Hou, Y. Guo, T. Yang, J. Fan and C. Zhi, *Angew. Chem., Int. Ed.*, 2024, **136**, e202407589.
258 Z. Shu, H. Chen, X. Liu, H. Jia, H. Yan and Y. Cai, *Adv. Funct. Mater.*, 2023, **33**, 2301493.
259 G. Zhang, Q. Ji, K. Zhang, Y. Chen, Z. Li, H. Liu, J. Li and J. Qu, *Nano Energy*, 2019, **59**, 10–16.
260 W. Bi, X. Li, R. You, M. Chen, R. Yuan, W. Huang, X. Wu, W. Chu, C. Wu and Y. Xie, *Adv. Mater.*, 2018, **30**, 1706617.
261 Q. Jiang, Y. Lei, H. Liang, K. Xi, C. Xia and H. N. Alshareef, *Energy Storage Mater.*, 2020, **27**, 78–95.
262 S. Zhang, J. Wu, M. Zheng, X. Jin, Z. Shen, Z. Li, Y. Wang, Q. Wang, X. Wang, H. Wei, J. Zhang, P. Wang, S. Zhang, L. Yu, L. Dong, Q. Zhu, H. Zhang and J. Lu, *Nat. Commun.*, 2023, **14**, 3634.
263 Z. Han, D. Tranca, F. Rodríguez-Hernández, K. Jiang, J. Zhang, M. He, F. Wang, S. Han, P. Wu and X. Zhuang, *Small*, 2023, **19**, 2208102.
264 J. Shah, T. Wu, J. Lucero, M. A. Carreon and M. L. Carreon, *ACS Sustainable Chem. Eng.*, 2019, **7**, 377–383.
265 G. Meng, M. Jin, T. Wei, Q. Liu, S. Zhang, X. Peng, J. Luo and X. Liu, *Nano Res.*, 2022, **15**, 8890–8896.
266 Y. Li, J. Liu, Z. Sun, R. Li, L. Guo, X. Zhang, Y. Wang, Y. Wang, Z. Yu and C. Fan, *Green Chem.*, 2022, **24**, 9253–9262.
267 L. Zhang, Q. Zhou, J. Liang, L. Yue, T. Li, Y. Luo, Q. Liu, N. Li, B. Tang, F. Gong, X. Guo and X. Sun, *Inorg. Chem.*, 2022, **61**, 8096–8102.
268 T. Mou, J. Liang, Z. Ma, L. Zhang, Y. Lin, T. Li, Q. Liu, Y. Luo, Y. Liu, S. Gao, H. Zhao, A. M. Asiri, D. Ma and X. Sun, *J. Mater. Chem. A*, 2021, **9**, 24268–24275.
269 M.-Y. Qi, W.-Y. Xiao, M. Conte, Z.-R. Tang and Y.-J. Xu, *ACS Catal.*, 2025, **15**, 129–138.
270 H. Zhang, X. Lv, Y. Li, Y. Wang and J. Li, *ACS Nano*, 2010, **4**, 380–386.
271 D. Sun, W. Liu, Y. Fu, Z. Fang, F. Sun, X. Fu, Y. Zhang and Z. Li, *Chem. – Eur. J.*, 2014, **20**, 4780–4788.
272 J. Wang, X. Niu, R. Wang, K. Zhang, X. Shi, H. Y. Yang, J. Ye and Y. Wu, *Appl. Catal., B*, 2025, **362**, 124763.
273 H. Ling, H. Sun, L. Lu, J. Zhang, L. Liao, J. Wang, X. Zhang, Y. Lan, R. Li, W. Lu, L. Cai, X. Bai and W. Wang, *Nat. Commun.*, 2024, **15**, 9505.
274 H. Zhang, H. Hu, Y. Li, J. Wang and L. Ma, *Biosens. Bioelectron.*, 2024, **248**, 115997.
275 K. S. Docherty and P. J. Ziemann, *Aerosol Sci. Technol.*, 2003, **37**, 877–891.
276 Y. Ma, K. Chen, J. Ma, G. Xu, S. Dong, B. Chen, J. Li, Z. Chen, X. Zhou and G. Cui, *Energy Environ. Sci.*, 2019, **12**, 273–280.
277 H.-S. Hsieh and R. G. Zepp, *Environ. Sci.: Nano*, 2019, **6**, 3734–3744.
278 B. Weng, M.-Y. Qi, C. Han, Z.-R. Tang and Y.-J. Xu, *ACS Catal.*, 2019, **9**, 4642–4687.
279 M. Gryszel, A. Markov, M. Vagin and E. D. Głowacki, *J. Mater. Chem. A*, 2018, **6**, 24709–24716.
280 F. Kurtz, T. N. Dauwe, S. V. Yalunin, G. Storeck, J. G. Horstmann, H. Böckmann and C. Ropers, *Nat. Mater.*, 2024, **23**, 890–897.
281 Z. Zhang, L. Ding, X. Zuo, H. Feng and Q. Xia, *Med*, 2023, **4**, 404–431.
282 R. Swijnenburg, S. Schrepfer, J. A. Govaert, F. Cao, K. Ransohoff, A. Y. Sheikh, M. Haddad, A. J. Connolly, M. M. Davis, R. C. Robbins and J. C. Wu, *Proc. Natl. Acad. Sci.*, 2008, **105**, 12991–12996.
283 K. S. Jones, *Semin. Immunol.*, 2008, **20**, 130–136.
284 A. Khademhosseini and R. Langer, *Nat. Protoc.*, 2016, **11**, 1775–1781.
285 S. Short, G. Lewik and F. Issa, *Transplantation*, 2023, **107**, 2341–2352.
286 G. Piotti, A. Palmisano, U. Maggiore and C. Buzio, *Front. Immunol.*, 2014, **5**, 505.
287 A. Rafieerad, W. Yan, K. N. Alagarsamy, A. Srivastava, N. Sareen, R. C. Arora and S. Dhingra, *Adv. Healthcare Mater.*, 2021, 1–17.
288 M. Bresinsky and A. Goepferich, *Eur. J. Pharm. Biopharm.*, 2025, **208**, 114634.
289 J. Merola, D. D. Jane-wit, J. S. Pober, N. Haven, N. Haven and N. Haven, *JCI Insight*, 2018, **3**, e97881.
290 T. Fan, L. Yan, S. He, Q. Hong, F. Ai, S. He, T. Ji, X. Hu, E. Ha, B. Zhang, Z. Li, H. Zhang, X. Chen and J. Hu, *Chem. Soc. Rev.*, 2022, **51**, 7732–7751.
291 Q. Xu, S. Zhao, L. Deng, J. Ouyang, M. Wen, K. Zeng, W. Chen, L. Zhang and Y.-N. Liu, *Chem. Commun.*, 2019, **55**, 9471–9474.
292 V. G. Gayathri, B. Richard, J. T. Chacko, J. Bayry and P. A. Rasheed, *J. Mater. Chem. B*, 2025, **13**, 1212–1228.
293 S. Y. Won, R. Singhmar, S. Sahoo, H. Kim, C. M. Kim, S. M. Choi, A. Sood and S. S. Han, *Colloids Surf., B*, 2025, **245**, 114207.
294 Q. You, P. Wang, T. Zhu, Z. Jia, Z. Chang, L. Li and W.-F. Dong, *Mater. Today Bio*, 2025, **32**, 101747.
295 J. Shao, H. Xie, H. Huang, Z. Li, Z. Sun, Y. Xu, Q. Xiao, X.-F. Yu, Y. Zhao, H. Zhang, H. Wang and P. K. Chu, *Nat. Commun.*, 2016, **7**, 12967.
296 A. Yilmazer, K. N. Alagarsamy, C. Gokce, G. Y. Summak, A. Rafieerad, F. Bayrakdar, B. I. Ozturk, S. Aktuna, L. G. Delogu, M. A. Unal and S. Dhingra, *Small Methods*, 2023, **7**, 2300044.
297 F. Zhang, G. Sun, R. Zhao, F. Yang, X. Jiang, S. Song, J. Zhang, H. Shen and J. Shen, *Langmuir*, 2024, **40**, 11381–11389.

298 L. Li, Z. Xing, T. Liao, J. Wang, Z. Xu, Y. Kuang and C. Li, *Mater. Today Chem.*, 2024, **39**, 102171.
299 J. Chang and E. R. Waclawik, *RSC Adv.*, 2014, **4**, 23505–23527.
300 T. Zhang, Z. Xu, H. Chen, J. Liu, D. Luo, N. Liu, Y. Zhang and Z. Chen, *Chem. Eng. J.*, 2024, **488**, 150886.
301 H. Shahbazi, P. Seraji, H. Farraj, T. Yang, A. Kim, S. Fattahpour, I. Papailias, M. Diamond, S. Namvar, A. Ahmadiparidari, S. Wang, Z. Liu, S. Feng, K. Kumar, M. Ahart, J. Cabana, S. Kadkhodaei, J. Wang, Z. Huang, R. J. Hemley and A. Salehi-Khojin, *Science*, 2025, **388**, 950–956.
302 B. Mohanty, L. Giri and B. K. Jena, *Energy Fuels*, 2021, **35**, 14304–14324.
303 K. Wang, Q. Ren, Z. Gu, C. Duan, J. Wang, F. Zhu, Y. Fu, J. Hao, J. Zhu, L. He, C.-W. Wang, Y. Lu, J. Ma and C. Ma, *Nat. Commun.*, 2021, **12**, 4410.
304 H. Wan, Z. Wang, S. Liu, B. Zhang, X. He, W. Zhang and C. Wang, *Nat. Energy*, 2023, **8**, 431–432.
305 Z. Lu, L. Zeng, W. Song, Z. Qin, D. Zeng and C. Xie, *Appl. Catal., B*, 2017, **202**, 489–499.
306 M. Abdinejad, A. Farzi, R. Möller-Gulland, F. Mulder, C. Liu, J. Shao, J. Biemolt, M. Robert, A. Seifitokaldani and T. Burdyny, *Nat. Catal.*, 2024, **7**, 1109–1119.